

**Characterization of Time-Varying Backgrounds in the PROSPECT Experiment**

A Thesis

Submitted to the Faculty

of

Drexel University

by

Olga Kzylova

in partial fulfillment of the

requirements for the degree

of

Doctor of Philosophy

March 2021



© Copyright 2021  
Olga Kzylova.

This work is licensed under the terms of the Creative Commons Attribution-ShareAlike  
license Version 3.0. The license is available at  
<http://creativecommons.org/licenses/by-sa/3.0/>.

## Dedications

This thesis is dedicated to the memory of my grandmother.

## Acknowledgments

The material in this thesis is based upon work supported by the U.S. Department of Energy, Office of Science, Office of High Energy Physics under Award Number DE-SC0017815.

This thesis would not be completed without a support of many people surrounding me during these years at Drexel.

First and most, I cannot thank enough my advisor Prof. Michelle Dolinski for giving me opportunity to join and participate the particle physics world, supporting me throughout the work, and being patient with me and my questions.

I would like to thank my collaborators Dr. Nathaniel Bowden, Dr. Pieter Mumm, Dr. Karsten Heeger, and Dr. Bryce Littlejohn. I highly appreciate mentorship of Pranava – without it, my work in PROSPECT would be far more challenging. I am thankful to Johathan and Pierce, who were willing to answer my questions and discuss the problems I met throughout my work on the dissertation. I also want to thank Danielle N., Tom, Jeremy G. and Jeremy Lu, Xianyi, Ben, Danielle B., Michael, Tim, Adam and Don for those years of working together. I want to thank the particle group at Drexel - Dr. Chuck Lane, Ruey and our undergraduate students for the discussions of my work during out meetings, and suggesting new ideas and solutions.

I highly appreciate guidance, ideas and critique of my committee members: Dr. Jim Napolitano, Dr. Brigita Urbanc, Dr. Russell Neilson, and Dr. Naoko Kurahashi Neilson. Thank you for being patient, understanding and interested in my success.

The path to this thesis would be very different without a support of my peers at Drexel. Without hours spent on classes with my cohort: Joey, Kelley, Ginny, Shuting and Ben. Without support of other students from Drexel community: Angelica, Justin, Sean and Steve, Matt, Joe F., Anton, Eli, Dustin, Rob, Kaho and Jackie.

I want to thank Drexel administration: Laura, Janice, Jackie, as well as Lisa, Maryann and Wolf, Dr. McMillan and Dr. Vogeley for making the whole process of working on thesis possible for us.

Finally, I would like to thank my family and friends for being there for me and supporting me throughout these years.

## Table of Contents

LIST OF TABLES . . . . .	ix
LIST OF FIGURES . . . . .	x
ABSTRACT . . . . .	xvi
1. INTRODUCTION TO NEUTRINOS . . . . .	1
1.1 Neutrinos . . . . .	1
1.2 Neutrino Oscillations . . . . .	3
1.2.1 Solar and Atmospheric Neutrino Anomalies . . . . .	3
1.2.2 Description of Neutrino Oscillations . . . . .	4
1.3 Theory of Neutrino Mass . . . . .	7
1.3.1 Three Flavor Paradigm . . . . .	7
1.3.2 Sterile Neutrinos . . . . .	10
1.4 Reactor Experiments . . . . .	11
1.4.1 Overview of Reactor Experiments . . . . .	11
1.4.2 The Reactor Antineutrino Spectrum and Flux Anomalies . . . . .	15
2. PROSPECT . . . . .	18
2.1 Goal, Idea and Design . . . . .	18
2.1.1 High Flux Isotope Reactor . . . . .	19
2.1.2 Detector Design . . . . .	20
2.1.3 $\bar{\nu}_e$ Detection Strategy . . . . .	21
2.1.4 Oscillation Search Strategy . . . . .	24
2.1.5 Achieved Parameters . . . . .	25
2.2 Detector Assembly and Installation . . . . .	26
2.3 Data Taking and Detector Evolution . . . . .	28
2.4 Event Classification . . . . .	29

2.4.1	Pulse Cruncher . . . . .	29
2.4.2	Low Level Calibration . . . . .	30
2.4.3	Cluster Analysis and Event Reconstruction . . . . .	34
3.	BACKGROUND . . . . .	35
3.1	PROSPECT Background Rejection . . . . .	35
3.1.1	Reactor Related Background . . . . .	35
3.1.2	PROSPECT Shielding Structure . . . . .	36
3.1.3	Shielding from Cosmogenic Background . . . . .	39
3.2	Primary Cosmic Rays . . . . .	41
3.2.1	Solar Modulation of Galactic Cosmic Rays . . . . .	42
3.2.2	Solar Events and Solar Cosmic Rays . . . . .	43
3.2.3	Geomagnetic Field Effect on Cosmic Rays . . . . .	45
3.3	Secondary Cosmic Rays . . . . .	46
3.3.1	Mesonic Component: Pions and Kaons . . . . .	47
3.3.2	Mesonic Component: Muons and Neutrinos . . . . .	48
3.3.3	Electromagnetic Component: Electrons, Positrons and Photons . . . . .	48
3.3.4	Hadronic Component: Protons and Neutrons . . . . .	49
3.3.5	Air Showers . . . . .	49
3.4	Background and Atmospheric Parameters . . . . .	50
3.4.1	Dependence on Atmospheric Pressure . . . . .	50
3.4.2	Dependence on Temperature . . . . .	51
4.	EVENT SELECTION AND VETOES . . . . .	52
4.1	Cuts for Single Background Events . . . . .	53
4.2	Rates of Single Background Events . . . . .	54
4.2.1	Muon-like Single Events . . . . .	54
4.2.2	Recoil-like Single Events . . . . .	55
4.2.3	Neutron Capture Single Events . . . . .	57

4.2.4	All Single Events . . . . .	58
4.3	Veto Application . . . . .	58
4.4	Dead Time . . . . .	59
4.5	Water Pool Level Singles Study . . . . .	61
5.	PROMPT AND DELAYED SINGLES ANALYSIS . . . . .	67
5.1	Prompt-like Events . . . . .	67
5.1.1	Selection of Prompt-like Single Events . . . . .	67
5.1.2	Rates and Energy Spectra of Prompt-like Single Events . . . . .	68
5.1.3	Prompt-like singles peaks stability . . . . .	71
5.2	Delayed-like Events . . . . .	72
5.2.1	Selection of Delayed-like Single Events . . . . .	72
5.2.2	Rates and Energy Spectra of Delayed-like Single Events . . . . .	73
5.2.3	Time Dependence of Delayed-like Rates . . . . .	74
6.	COINCIDENCE ANALYSIS . . . . .	79
6.1	Coincidence Analysis . . . . .	79
6.1.1	Coincidence Events Cuts . . . . .	79
6.1.2	Coincidence Analysis Accidentals Subtraction . . . . .	81
6.2	Background Subtraction . . . . .	83
6.2.1	Background Scaling with Pressure . . . . .	83
6.2.2	Average Pressures for Reactor-On and Reactor-Off Periods . . . . .	85
6.2.3	Barometric Coefficients . . . . .	87
6.3	Results . . . . .	88
6.3.1	Evolution of Rates with Time and Pressure Dependence . . . . .	88
6.3.2	Average Rates, Barometric and Scaling Coefficients . . . . .	90
6.4	PROSPECT Results . . . . .	92
6.4.1	Spectrum Results . . . . .	92
6.4.2	Oscillation Results . . . . .	94

7. SEASONALITY STUDY OF MUONS . . . . .	99
7.1 Introduction . . . . .	99
7.2 Pressure Dependence . . . . .	101
7.3 Temperature Datasets . . . . .	102
7.3.1 Source of temperature data . . . . .	102
7.3.2 Validity of Results in Nashville . . . . .	103
7.3.3 Comparison of Ground and MMP Temperatures . . . . .	104
7.3.4 Modified Effective Temperature Calculation . . . . .	104
7.3.5 Mass Weighted Temperatures Calculation . . . . .	106
7.4 Rate vs Temperature . . . . .	107
7.4.1 Correlation Coefficients . . . . .	107
7.4.2 Linear Scaling with Pressure and Temperature . . . . .	109
7.4.3 Michel Electrons . . . . .	110
8. CONCLUSION . . . . .	114
BIBLIOGRAPHY . . . . .	116
APPENDIX A: SPATIAL DISTRIBUTION STUDY OF RECOIL-LIKE EVENTS . . . . .	122
APPENDIX B: ANALYSIS OF TEMPERATURE DEPENDENCE OF MUON-LIKE EVENTS . . . . .	127
B.1 Temperature Measurements . . . . .	127
B.2 Atmospheric Depth Calculation . . . . .	128
B.3 Cutoff Altitude . . . . .	128
B.4 Uncertainty . . . . .	129

## List of Tables

1.1	The values for 3-neutrino oscillation parameters obtained from the current neutrino oscillation experimental data. Here, $\delta$ is a Dirac phase. The values are obtained for normal hierarchy $m_1 < m_2 < m_3$ , and the values in brackets - for the inverted hierarchy $m_3 < m_1 < m_2$ . The data are presented in <sup>1</sup> , and originally collected in global fit in <sup>2</sup> . . . . .	7
4.1	Cuts for single background events. . . . .	57
5.1	Cuts for prompt-like single events. . . . .	67
5.2	Cuts for delayed-like single events. . . . .	72
6.1	Cuts for prompt and delayed events for IBD-like, recoil + nLi, and nLi + nLi coincidences. The delayed event for these pairs has the same cuts. . . . .	81
6.2	Average pressure comparison between script's and manual results for Period 1, Period 2 and Total from PRL paper dataset <sup>3</sup> . . . . .	86
6.3	Rates, barometric coefficients, and on-off scaling coefficients for different types of single and correlated event categories. . . . .	90
7.1	Correlation coefficients for different temperature datasets and different energy bins of deposited energy of muon-like events in PROSPECT detector. . . . .	108
7.2	Correlation coefficients of different muons datasets with different temperature datasets. . . . .	110
A.1	Correlation coefficients with atmospheric pressure, and $\chi^2/\text{DOF}$ for recoil-like events for different selection of spatial distribution, z-fiducial, and PSD cuts . . . . .	126

## List of Figures

1.1	Left: the detector used in Savannah River experiment. The water tanks with $\text{CdCl}_2$ are labeled with A and B. Tanks with liquid scintillator are marked with I, II, and III. Right: the details of IBD mechanism in the experiment <sup>4</sup> . . . . .	3
1.2	Scheme of fission reactions in the nuclear reactor with $^{235}\text{U}$ fuel. . . . .	11
1.3	Reactor emission and measured spectra. The measured spectrum ( $s_0 \cdot s_d$ , red) is obtained via multiplying of emitted spectrum from the reactor ( $s_0$ , blue) by the detection IBD cross-section ( $s_d$ , green) <sup>5</sup> . . . . .	13
1.4	Flux deficit for different experiment at different distances. The datapoints show measured rate of $\bar{\nu}_e$ normalized to the theoretical expectation (Huber/Mueller model) for 3-flavors neutrino model <sup>6</sup> . . . . .	15
1.5	Oscillation parameter space for sterile neutrinos in 3+1 model suggested for Reactor Neutrino Anomaly <sup>7</sup> . . . . .	16
1.6	(a) Daya Bay comparison for measured reactor spectrum in comparison to theoretical predictions (Huber/Mueller model). (b) Ratio of predicted and measured events that shows bump in the region 4-6 MeV. (c) $\chi^2$ distribution showing abnormality in the same energy range <sup>6</sup> . . . . .	17
2.1	Left: (a, b) Photograph of a HFIR reactor. (c) The drawing of the active fuel. (d) The power distribution of the reactor in 2D projection <sup>8</sup> . Right: replacement of a reactor core during reactor shutdown. . . . .	19
2.2	Left: Cutaway schematic drawing of a detector showing the optical grid and array of segments. Right: A cross-section of the PROSPECT detector showing the locations of inserting calibration sources (red) and optical insert (yellow) <sup>8</sup> . . . . .	21
2.3	Left: Central and end pinwheels - plastic 3D-printed pieces consisting the optical grid; Right: Example of fiber optic assembly that would be inserted into central pinwheel <sup>8</sup> . . . . .	22
2.4	Schematic drawing of detector segments. Left: the individual segment with double-ended PMT-readout. Right: the inner detector that is enclosed by the inner acrylic tank <sup>8</sup> . . . . .	23
2.5	Left: Schematic drawing of PMT in the housing. Right: photo of a single PMT in the housing. . . . .	24
2.6	A schematic picture explaining the detection of $\bar{\nu}_e$ in PROSPECT. . . . .	25
2.7	Left: Template waveforms from the PROSPECT-50 prototype detector showing the different shapes of electronic recoil and nuclear recoil energy depositions in the liquid scintillator. The source that was used is $^{252}\text{Cf}$ . PSD is a metric that is equal to the fraction of charge in the tail of the pulse to the total integral charge. Right: The distribution of PSD parameters as a function of energy for the same detector and energy source <sup>9</sup> . . . . .	26
2.8	Different baselines for the reactor . . . . .	27

2.9	MC-generated oscillated spectra for different baselines for RAA best-fit point ( $\sin^2 2\theta_{14} = 0.165$ , $\Delta m_{41}^2 = 2.39 \text{ eV}^2$ ).	27
2.10	Work on PMTs and optical grid in Yale Wright Laboratory's clean room.	28
2.11	One of the first displayed detected hadron, muon and IBD-candidate. The color and size indicate how much energy was deposited.	29
2.12	An example of electron pulse and how it looks into analysis. The dashed vertical line is the half-height leading edge timing. The presented plot is obtained after being inverted and baseline subtracted <sup>10</sup> .	30
3.1	The 3D design of detector shielding layers. The inner detector, separated in array of 11 x 14 segments is surrounded by acrylic tank, shown in rose color. Acrylic segment supports (light green), optical grid and PMT housings (beige) are indicated in the picture. The essential layers of the shielding include 5% borated polyethylene (purple), secondary aluminum tank (light gray) <sup>11</sup> .	37
3.2	Detector bottom part of the shielding and the support chassis <sup>11</sup> .	38
3.3	(left) 3D layout of detector, Experiment Room, shield wall, reactor and the water pool. (right) 2D disposition of PROSPECT detector. The scheme shows shield wall that covers the holes in the pool wall to provide shielding from this source of high reactor background. The picture also shows the disposition of the detector on concrete monolith under the floor. <sup>11</sup>	39
3.4	A photograph of the lead wall. The red arrows indicate the pipes penetrating to the reactor water pool. A blue arrow indicates EF-4 beam line that is directed toward the reactor vessel. The central part of the wall is 2.1 m tall and 3.0 m wide. <sup>11</sup>	40
3.5	A simulation of the cosmogenic neutrons interactions that pass IBD topology cuts and segment-end fiducialization. <sup>11</sup>	41
3.6	Plots of the monthly sunspot number (blue) and smoothed sunspot number (red) for the solar cycles 19-24 <sup>12</sup> .	43
3.7	Solar modulation of cosmic rays. The upper plots show rates of cosmic rays from Climax neutron monitor (blue), and from Moscow, Russia that is rescaled and plotted in red. The lower plots shows monthly sunspot numbers <sup>13</sup> .	44
3.8	A record of Oulu neutron monitor during GLE in July 14, 2000. As shown in the picture, first CME (1) at the Sun happens on July 11th. It arrives on Earth on July 13 (2), and the Forbush decrease in rates of cosmic rays is observed. On July 14, a second powerful CME happens on the Sun, which accelerates high energy solar particles that reach Earth within minutes. This sudden increase in cosmic rays of solar origin is observed as GLE (3). Finally, second CME arrives on Earth on July 15 (4) and sweep away galactic cosmic rays. Another Forbush decrease is detected by Oulu neutron monitor. Second CME also produces the largest geomagnetic storm on Earth in 10 years. The plot is obtained from Neutron Monitor Database NEST <sup>14</sup> .	45
3.9	Production of cosmic ray showers in the atmosphere <sup>15</sup> .	46

3.10	The estimations of vertical fluxes of cosmic rays with energies above 1 GeV in the atmosphere as a function of altitude. The energy regions used were the regions in which the particles are the most present, except for electrons <sup>16</sup> .	47
4.4	Rates of muon-like singles with time.	57
4.5	Rates of recoil-like singles with time.	58
4.6	Rates of recoil-like singles with time for RxOff only.	59
4.7	Rates of neutron captures with time.	60
4.8	Rates of all single events with time.	61
4.9	Rates of all single events with time for RxOff only.	62
4.10	Scheme of implementation of cosmic shower veto. Delayed neutron-capture candidate is shown in purple, veto triggering events are shown in red, and time window are represented with blue arrows.	63
4.11	Smeared spectra of reconstructed energy of prompt event in IBD candidate. Spectra with different cuts illustrate the effectivity of these cuts. The accidentals are subtracted <sup>10</sup> .	64
4.12	Scheme of calculation of dead time.	64
4.13	Comparison of deadtime for different types of vetoes over time.	65
4.14	Reactor scheme of change of water level <sup>17</sup> .	65
4.15	The rates of single neutron capture events (top) and recoil-like single events (bottom) comparing to the water level drop in the period 07/06 - 07/24 when the longest water level drop happened. Water level is shown in red.	66
5.1	Optional caption for list of figures	68
5.2	Cumulative spectra of prompt-like singles for reactor on and reactor off periods.	69
5.4	Rate of prompt-like singles vs time for different energy bins	71
5.5	Fitted value of the peak of Tl-208 shown for one time bin of 48 hours during reactor off period.	72
5.6	Mean energy of the peak Tl-208 vs time.	73
5.7	Width of the peak Tl-208 vs time.	74
5.8	Fitted value of the peak at 7.7 MeV shown for one time bin of 48 hours during reactor on period	75
5.9	Mean energy of the peak at 7.7 MeV vs time.	75
5.10	Width of the peak at 7.7 MeV vs time.	76
5.11	Optional caption for list of figures	76

5.12 Energy of delayed-like singles for reactor on (blue) and reactor off (green) . . . . . 77

5.14 Time evolution of rates of delayed-like singles. . . . . 78

6.1 Plot of live time fraction of each data point when each time bin is 24 hours. The dashed line shows the cutoff limit: if the amount of the real data in the time bin is less than 2 hours, those data points got cut off. . . . . 84

6.2 Overlapping of pressure time bins with runs . . . . . 86

6.3 Neutron monitor stations locations . . . . . 87

6.4 Rates of recoils + nLi coincidences with time. Each time bin is 8 hours. . . . . 89

6.5 Rates of recoils + nLi events vs atmospheric pressure. Left: RxOn and RxOff periods. Right: RxOff only. . . . . 90

6.6 Rates of nLi + nLi coincidences with time. Each time bin is 24 hours. . . . . 91

6.7 Rates of nLi + nLi events vs atmospheric pressure. Left: RxOn and RxOff periods. Right: RxOff only. . . . . 92

6.8 Rates of IBD-like events and accidentals with time. Each time bin is 24 hours. . . . . 93

6.9 Rates of IBD-like events vs atmospheric pressure. Left: RxOn and RxOff periods. Right: RxOff only. . . . . 94

6.10 The observed prompt visible energy spectrum of IBD-like events (with subtracted accidentals) during reactor-on periods and during reactor-off periods. Reactor-off spectrum is scaled with time exposure and atmospheric pressure conditions to match the same parameters of reactor-on spectrum. The result of the subtraction, which is a final spectrum of IBD signal, is shown in black with only statistical errors<sup>18</sup>. . . . . 95

6.11 Assignment of baseline bins to the fiducial segments<sup>18</sup>. . . . . 96

6.12 Comparison of the relative measured spectra of  $E_{rec} \frac{M_{l,\nu e}}{M_e}$  with predicted  $\frac{P_{l,\nu e}}{P_e}$  for different baseline bins. The predicted spectrum is oscillated for the best-fit point of  $(\sin^2 2\theta_{14}, \Delta m_{41}^2) = (0.11, 1.78 \text{ eV}^2)$  (purple solid lines) and for RAA best-fit point (blue solid lines) from<sup>19</sup>. Without oscillations, the ratio is a flat unity. Statistical uncertainties are shown with error bars<sup>18</sup>. . . . . 97

6.13 Exclusion contours for oscillations of sterile neutrino for Feldman-Cousins (black) and Gaussian CLs (red) methods. Green and yellow belts are the PROSPECT exclusion ranges from the toy MC datasets, grey belt is the RAA and best-fit point from<sup>20</sup> and preferred parameter space<sup>18</sup>. . . . . 98

7.1 Dependence of temperature deviations from the mean value at the locations of Nagoya ground muon detector in Japan, and at the Kuwait City ground muon detector in Kuwait. Top plots show temperature deviations in the regions close to maximum muon production altitude ( $\Delta T[h_{MMP} = 16.5 \text{ km}]$ ) and bottom plots show temperature deviation near the ground ( $\Delta T[h_{GRD} = 0.5 \text{ km}]$ ). The black dashed curves are 3 months-average, and the colored curved are daily data.<sup>21</sup> . . . . . 100

7.2	Dependence of temperature at isobar pressure of 100 hPa line (level of maximum muon production). <sup>21</sup> . . . . .	101
7.3	Rates of muon-like singles vs atmospheric pressure for combined RxOn and RxOff periods.101	
7.4	National Weather Service station in Nashville (left) and a balloon inside before launching (right) <sup>22</sup> . . . . .	102
7.5	Comparison between ground temperatures at the balloon station in Nashville and near HFIR at Oak Ridge . . . . .	103
7.6	Comparison of ground and MMP temperatures at station in Nashville at Pressure = 100 hPa. . . . .	104
7.7	Left: Air mass weight function ( $w[ht]$ ) for mass-weighted method. Middle: weight function ( $\omega[x]$ ) of the effective temperature method vs atmospheric depth. Right: weight function ( $\omega[x]$ ) of the modified effective temperature method vs atmospheric depth. <sup>21</sup> . . . . .	105
7.8	Modified effective ( $T_{EFF-M}$ ) and mass weighted ( $T_{MSS}$ ) temperatures at Nashville for PROSPECT data taking period. . . . .	107
7.9	Rates for muon-like events for all events in the muon-like cut, and for energy ranges 15-200 MeV, 200-250 MeV, and 250-800 MeV, all compared to $T_{MSS}$ . . . . .	108
7.10	Top: Rates for muon-like events vs atmospheric pressure, before scaling with pressure, and after scaling. Bottom: Rates of muon-like events, already scaled with atmospheric pressure, vs $T_{MSS}$ . . . . .	109
7.11	Behavior of muon-like events with high deposited energy (250-8000 MeV) vs atmospheric pressure (left) and vs $T_{MSS}$ (right). . . . .	110
7.12	Rate of Michel electrons vs time, compared to $T_{MSS}$ . . . . .	111
7.13	Rate of Michel electrons, already scaled with pressure vs time, compared to $T_{MSS}$ . . . . .	112
7.14	Dependence of rate of Michel electrons on atmospheric pressure before and after pressure scaling. . . . .	112
7.15	Dependence of scaled with pressure rate of Michel electrons on $T_{MSS}$ . . . . .	113
A.1	The dividing of the detector into 9 parts. Each part has 14 segments. Excluded segments are not colored. . . . .	123
A.2	PSD vs energy distributions for the events into each of 9 parts for one reactor-on run on May 15th, 2018. The plots show the behavior of ingress events that increase at the bottom of the detector, and to the right side above "hot spot". . . . .	124
A.3	Separation of detector segments into left, right, top and bottom parts. Excluded segments are shown in red, and non-fiducial segments are shown in blue. . . . .	125
A.4	Separation of detector segments into left, right, top and bottom parts. Excluded segments are shown in red, and non-fiducial segments are shown in blue. . . . .	125

A.5	Separation of detector segments into left, right, top and bottom parts. Excluded segments are shown in red, and non-fiducial segments are shown in blue. . . . .	126
B.1	Dependence of temperature on altitude for dry and humid seasons. . . . .	127
B.2	Dependence of humidity on altitude for dry and humid seasons. . . . .	127
B.3	Dependence of atmospheric dependence with altitude. . . . .	129
B.4	Maximum altitude of balloon flight. . . . .	130
B.5	Dependence of height cutoff on $T_{EFF-M}$ value. . . . .	131
B.6	Comparison of effective temperature calculations in Peachtree City, Nashville, and Blacksburg . . . . .	131
B.7	Difference between EFF-M temperatures in Peachtree City and Nashville . . . . .	132
B.8	Comparison of MSS temperature calculations in Peachtree City, Nashville, and Blacksburg	132
B.9	Difference between MSS temperatures in Peachtree City and Nashville . . . . .	133

## Abstract

Characterization of Time-Varying Backgrounds in the PROSPECT Experiment

Olga Kzylova

Michelle Dolinski, Ph.D.

Recent reactor neutrino experiments aimed for the study of neutrino oscillations exhibited anomalies in both flux and the antineutrino spectrum. The  $\sim 6\%$  deficiency of observed flux with respect to theoretical predictions, called the Reactor Antineutrino Anomaly, can be explained through flaws in theoretical model of reactor antineutrino spectrum or existence of eV-scale sterile neutrino state leading to meter-scale neutrino oscillations. The anomaly in spectrum in the energies 4-6 MeV raised a question about insufficiency of our reactor nuclear model.

The Precision Reactor Oscillation and Spectrum Experiment (PROSPECT) was developed to study these anomalies by looking at antineutrino oscillations at short ( $< 12$  m) baselines from a highly-enriched ( $\sim 93\%$   $^{235}\text{U}$ ) uranium reactor core. The detector precisely measured and compared the  $^{235}\text{U}$  antineutrino spectrum to the existing nuclear data and performed a reactor-model independent search for eV-scale sterile neutrino oscillations, extending current parameter map of sterile neutrinos.

The major challenge of the PROSPECT experiment is distinguishing the rare neutrino signal from a very high background rate on the surface. One of the strategies that PROSPECT utilizes for this is a background subtraction - a bin-by-bin energy spectrum subtraction when the reactor is shut down from when the reactor is operating. This work discusses the background measurements of PROSPECT detector, attributing the time variation of the background to the environmental parameters, evolution of the detector, and the operation status of the reactor, and presents details of successful handling of the background subtraction.



## Chapter 1: Introduction to Neutrinos

### 1.1 Neutrinos

Neutrino is a class of neutral fundamental particles that interact only via weak subatomic force and gravity. Neutrinos are fermions and have very small mass which is much smaller than mass of other particles. There are 3 flavors of neutrinos that are known and well-studied today: electron neutrinos  $\nu_e$ , muon neutrinos  $\nu_\mu$ , and tau neutrinos  $\nu_\tau$ , and their 3 corresponding anti-particles:  $\bar{\nu}_e$ ,  $\bar{\nu}_\mu$ , and  $\bar{\nu}_\tau$ . Each flavor of neutrino corresponds to 3 leptons ( $e$ ,  $\mu$ ,  $\tau$ ). The division of neutrinos in the three flavors do not correspond to their mass states, and therefore each neutrino flavor will be a superposition of the mass states and vice versa.

Since neutrino do not interact through strong or electromagnetic forces, they rarely interact with the matter and therefore have very long free path in different materials. For example, free path of neutrino with energy of about 3-10 MeV in the water is about  $10^{18}$  m which is about 100 light years. Every second about  $6 \cdot 10^{10}$  neutrinos from the Sun pass through area of  $1 \text{ cm}^2$  on Earth without interaction with the matter. Therefore, it is very hard to detect the neutrinos, and for many years they were only theoretically predicted particle. It is easier to detect neutrinos with higher energies than with lower energies.

The prediction of the existence of neutrino was formulated by Wolfgang Pauli in 1930 as a possible solution of the violation of conservation of energy and spin statistics in the beta-decay. Pauli suggested that the new type of particle, a low-mass electrically neutral particle is emitted from the nucleus in the process of beta-decay and carries part of the energy with itself<sup>23</sup>.

A neutrino was observed experimentally by Clyde Cowan and and Frederick Reines in the nuclear reactor experiment at Savannah River Plant in the USA in 1956<sup>24</sup>. Savannah River experiment utilized 2 tanks with 200 litres of water target in total with 40 kg of  $\text{CdCl}_2$  dissolved in water. The water tanks were sandwiched between 3 tanks of liquid scintillator (Figure 1.1). Liquid scintillator tanks had 110 photomultiplier tubes (PMTs) on both ends of each and detected the signals, while

water tanks acted as a proton target. The detector was located at 12 m underground to reduce cosmogenic background.

The process in which electron antineutrino is born is called beta-decay:

$$n \rightarrow p + e^{-} + \bar{\nu}_e. \quad (1.1)$$

In the experiment at Savannah River Plant, the electron antineutrino that was produced in nuclear reactor was detected through the inverse-beta decay mechanism:

$$\bar{\nu}_e + p^{+} \rightarrow n + e^{+} \quad (1.2)$$

Electron antineutrino interacts with a proton in the water tanks and produces neutron and positron. Positron quickly annihilates with one of the electrons in the scintillator producing two gamma-rays of 511 keV each, and the neutron is captured on a nucleus, producing another gamma-particle, that are detected with photomultiplier tubes. In Savannah River reactor experiment, thermalized neutrons were captured on Cd:

$$n + {}^{108}\text{Cd} \rightarrow \gamma + {}^{109}\text{Cd}. \quad (1.3)$$

Thus, positron annihilation and neutron capture created distinct tags with specific energies and time window, allowing to sufficiently reduce background. The difference between the rates when the reactor was on comparing when it was shutdown for fuel replacement demonstrated that neutrinos were born in the reactor. The subtraction of background during off-periods also efficiently helped extract true signal. The researchers could obtain signal to background ratio of 3:1. The vast majority of reactor experiments discussed in Section 1.4 work using the same principle today.

After the discovery of neutrino, multiple experiments were created and properties of neutrino have been extensively studied. The existence of  $\nu_{\mu}$  and distinction from  $\nu_e$  was first predicted by Bruno Pontecorvo in 1959<sup>25</sup> and discovered with accelerator experiment in Brookhaven National Lab

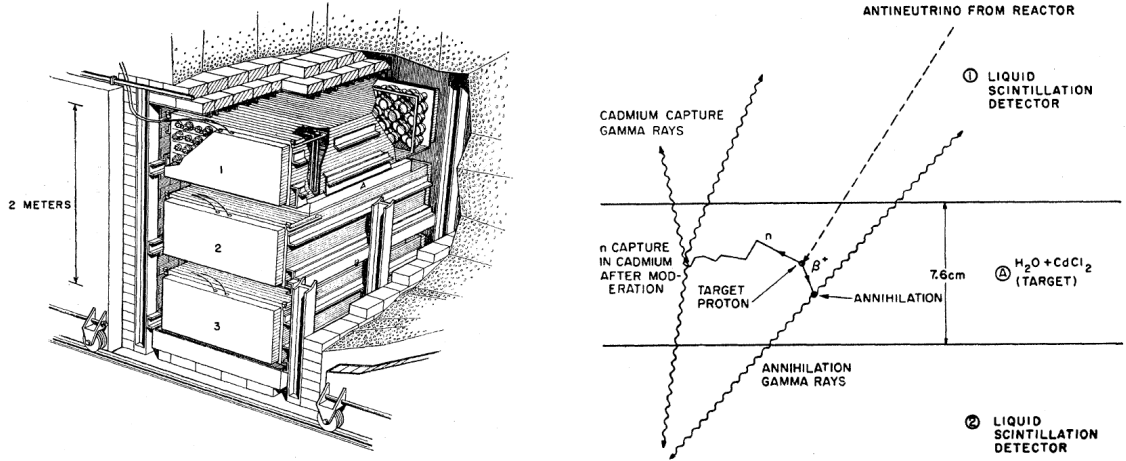


**Figure 1.1:** Left: the detector used in Savannah River experiment. The water tanks with  $\text{CdCl}_2$  are labeled with A and B. Tanks with liquid scintillator are marked with I, II, and III. Right: the details of IBD mechanism in the experiment<sup>4</sup>.

in 1962<sup>26</sup>. Tau neutrino  $\nu_\tau$  was discovered in 2000 at DONUT accelerator experiment at Fermilab<sup>27</sup>.

## 1.2 Neutrino Oscillations

### 1.2.1 Solar and Atmospheric Neutrino Anomalies

One of the types of neutrinos we can measure at Earth are the neutrinos produced inside the Sun's core. The nuclear reactions include proton-proton chain reaction in which neutrinos, alpha particles, positrons and gamma-rays are emitted.

The scientists since the late 1960s measured a deficit in the neutrino flux comparing to the theoretical predictions. Ray Davis and John N. Bahcall's Homestake Experiment at the Homestake Gold Mine in the US was designed to test the Standard Solar Model by measuring the solar neutrino flux. A chlorine-based detector utilized neutrino absorption on  $^{37}\text{Cl}$ , suggested by Pontecorvo<sup>28</sup>



The experiment detected only about a third of predicted neutrinos from the Standard Solar Model<sup>29;30</sup>. This discrepancy was named the "solar neutrino problem".

Subsequent experiments with radiochemical and water Cherenkov detector confirmed these re-

sults. One of the Cherenkov detectors, Kamiokande-II in Japan, quantitatively confirmed the flux discrepancy of about one third comparing to the prediction<sup>31</sup>. The experiment at Sudbury Neutrino Observatory (SNO) also got 34% deficit<sup>32</sup>.

Another anomaly that raised questions about neutrino fluxes that reach the Earth is a "atmospheric neutrino anomaly". Atmospheric neutrinos is a product of cosmic rays from outside the Solar System after their interaction with air molecules high in the Earth atmosphere. This reaction produces  $\pi$  and  $K$  mesons. Pions decay into muon  $\mu^-$  and muon antineutrino  $\bar{\nu}_\mu$  and consequently, muon decays into electron  $e^-$ , electron antineutrino  $\bar{\nu}_e$  and muon neutrino  $\nu_\mu$ :

$$\pi^- \rightarrow \mu^- + \bar{\nu}_\mu, \quad \mu^- \rightarrow e^- + \bar{\nu}_e + \nu_\mu \quad (1.5)$$

As a result, a ratio between muon and electron neutrinos has to be 2 with the small uncertainty regarding decay of kaons:

$$\frac{\nu_\mu}{\nu_e} = \frac{\Phi(\nu_\mu + \bar{\nu}_\mu)}{\Phi(\nu_e + \bar{\nu}_e)} \quad (1.6)$$

Water Cherenkov detector at Kamiokande-II experiment that measures atmospheric neutrinos, reported in 1988 that the amount of electron neutrinos was in agreement with theoretical prediction, while muon neutrinos revealed a deficit of about 40% comparing to the theoretical predictions<sup>33</sup>. Multiple other detectors later confirmed this deficit<sup>34;35</sup>.

## 1.2.2 Description of Neutrino Oscillations

Solar and atmospheric neutrino anomalies and increasing number of empirical evidence in their favour raised a question that physics describing the neutrino behavior could be lacking an important piece. Italian and Soviet physicist Bruno Pontecorvo was the first who predicted quantum mechanic neutrino oscillations from matter to antimatter back in 1957<sup>36</sup>. Few years later, the theory was quantitatively developed to oscillations between neutrino flavors by Ziro Maki, Masami Nakagawa, and Shoichi Sakata in 1962<sup>37</sup>, and Pontecorvo in 1967<sup>38</sup>.

Similarly to quarks, neutrino can oscillate between different neutrino flavors. However, this

phenomena requires neutrinos to have a non-zero mass, and this mass must vary between generations. Since the initial Standard Model theory did not include neutrino mass and oscillations, it had to be modified by including a mass term into general Lagrangian and the mix matrix of neutrino, called the PMNS matrix (Pontecorvo–Maki–Nakagawa–Sakata matrix).

Chiral left-handed neutrinos are observed in the reactions with leptons, conserving lepton charge. The states they are in are called flavors, or weak eigenstates:  $\nu_e$ ,  $\nu_\mu$ , and  $\nu_\tau$ , and the corresponding antineutrinos. The mass eigenstates come from mixing of weak eigenstates through the unitary transformations:

$$|\nu_\alpha\rangle = \sum_i U_{\alpha i}^* |\nu_i\rangle \quad (1.7)$$

$$|\nu_i\rangle = \sum_\alpha U_{\alpha i} |\nu_\alpha\rangle \quad (1.8)$$

where  $|\nu_\alpha\rangle$  is a neutrino in the flavor state ( $\alpha = e, \mu, \text{ or } \tau$ ),  $|\nu_i\rangle$  is a neutrino in the mass state  $m_i$ ,  $i = 1, 2, 3$ , and the asterisk represents the complex conjugate of the unitary matrix.

$U_{\alpha i}$  here is the PMNS matrix ( $U_{\text{PMNS}}$ ) -  $3 \times 3$  matrix, analogue of the CKM matrix that describes analogous mixing of quarks. Then, the equation for 3 neutrino flavors would have a form:

$$\begin{pmatrix} \nu_e \\ \nu_\mu \\ \nu_\tau \end{pmatrix} = \begin{pmatrix} U_{e1} & U_{e2} & U_{e3} \\ U_{\mu1} & U_{\mu2} & U_{\mu3} \\ U_{\tau1} & U_{\tau2} & U_{\tau3} \end{pmatrix} \begin{pmatrix} \nu_1 \\ \nu_2 \\ \nu_3 \end{pmatrix} \quad (1.9)$$

Due to charge, parity, and the time reversal (CPT) symmetry, the  $U_{\text{PMNS}}$  for antineutrino would be same as  $U_{\text{PMNS}}$ .

The PMNS matrix can be parametrized into  $3 \times 3$  - for 3 neutrino flavors, or  $4 \times 4$  - if neutrino is a Majorana particle - forms.

$$\begin{aligned}
U_{\text{PMNS}} &= \begin{pmatrix} 1 & 0 & 0 \\ 0 & c_{23} & s_{23} \\ 0 & -s_{23} & c_{23} \end{pmatrix} \begin{pmatrix} c_{13} & 0 & s_{13}e^{-i\delta_{CP}} \\ 0 & 1 & 0 \\ -s_{13}e^{i\delta_{CP}} & 0 & c_{13} \end{pmatrix} \begin{pmatrix} c_{12} & s_{12} & 0 \\ -s_{12} & c_{12} & 0 \\ 0 & 0 & 1 \end{pmatrix} \begin{pmatrix} e^{i\alpha_1/2} & 0 & 0 \\ 0 & e^{i\alpha_2/2} & 0 \\ 0 & 0 & 1 \end{pmatrix} = \\
&= \begin{pmatrix} c_{12}c_{13} & s_{12}c_{13} & s_{13}e^{-i\delta_{CP}} \\ -s_{12}c_{23} - c_{12}s_{23}s_{13}e^{i\delta_{CP}} & c_{12}c_{23} - s_{12}s_{23}s_{13}e^{i\delta_{CP}} & s_{23}c_{13} \\ s_{12}s_{23} - c_{12}c_{23}s_{13}e^{i\delta_{CP}} & -c_{12}s_{23} - s_{12}c_{23}s_{13}e^{i\delta_{CP}} & c_{23}c_{13} \end{pmatrix} \begin{pmatrix} e^{i\alpha_1/2} & 0 & 0 \\ 0 & e^{i\alpha_2/2} & 0 \\ 0 & 0 & 1 \end{pmatrix}
\end{aligned}$$

Here, the matrix is parametrized through mixing angles  $\theta_{12}$ ,  $\theta_{23}$ , and  $\theta_{13}$ .  $c_{ij}$  represents  $\cos\theta_{ij}$ , and  $s_{ij}$  represents  $\sin\theta_{ij}$ .  $\delta$  is the CP-violating phase and is only non-zero if neutrino violates CP-symmetry - however, it has not been detected in the experiments yet.  $\alpha_1$  and  $\alpha_2$  are Majorana CP phase terms.

The mixing angles  $\theta_{ij}$  are being identified in the experiments and the oscillation parameters are collected in the Table 1.1. We can calculate the probability of oscillations of one neutrino flavor into another using simplification of two-neutrino flavors in vacuum. In such case, the PMNS matrix is  $2 \times 2$  matrix with mixing angle  $\theta$ :

$$U = \begin{pmatrix} \cos\theta & \sin\theta \\ -\sin\theta & \cos\theta \end{pmatrix} \quad (1.10)$$

The probability of a neutrino changing flavor in this case can be calculated as

$$P_{\alpha \rightarrow \beta, \alpha \neq \beta} = \sin^2(2\theta) \sin^2\left(\frac{\Delta m^2 L}{4E}\right) \quad (1.11)$$

where  $\Delta m^2 = m_1^2 - m_2^2$  and  $E = E_1 = E_2$ . This formula is used in the accelerator experiments where the appearance of neutrinos is studied. On the other hand, the probability of disappearance, i.e. the probability that the neutrino oscillates into another flavor at some distance L, is calculated

as:

$$P_{\alpha \rightarrow \alpha} = 1 - P_{\alpha \rightarrow \beta} = 1 - \sin^2(2\theta) \sin^2\left(\frac{\Delta m^2 L}{4E}\right) \quad (1.12)$$

The examples of disappearance experiments are reactor neutrino experiments, where the flux of original electron antineutrino, born in the nuclear reactor, decreases at some distance from the reactor. Those experiments prove that in this case  $\Delta m_{ij}^2$  is not zero, i.e. neutrino has mass.

**Table 1.1:** The values for 3-neutrino oscillation parameters obtained from the current neutrino oscillation experimental data. Here,  $\delta$  is a Dirac phase. The values are obtained for normal hierarchy  $m_1 < m_2 < m_3$ , and the values in brackets - for the inverted hierarchy  $m_3 < m_1 < m_2$ . The data are presented in<sup>1</sup>, and originally collected in global fit in<sup>2</sup>.

Parameter	Best-fit	$3\sigma$
$\Delta m_{21}^2$ [ $10^{-5} eV^2$ ]	7.37	6.93-7.96
$\Delta m_{31(23)}^2$ [ $10^{-3} eV^2$ ]	2.56 (2.54)	2.45-2.69 (2.42-2.66)
$\sin^2\theta_{12}$	0.297	0.250-0.354
$\sin^2\theta_{23}$ , $\Delta m_{31(32)}^2 > 0$	0.425	0.381-0.615
$\sin^2\theta_{23}$ , $\Delta m_{32(31)}^2 < 0$	0.589	0.384-0.636
$\sin^2\theta_{13}$ , $\Delta m_{31(32)}^2 > 0$	0.0215	0.0190-0.0240
$\sin^2\theta_{13}$ , $\Delta m_{32(31)}^2 < 0$	0.0216	0.0190-0.0242
$\delta/\pi$	1.38 (1.31)	$2\sigma : (1.0 - 1.9)$ $(2\sigma : (0.92 - 1.88))$

## 1.3 Theory of Neutrino Mass

### 1.3.1 Three Flavor Paradigm

The mass is included in the Standard Model through Dirac mass term  $m\psi\bar{\psi}$  in the Lagrangian. After decomposing the Dirac spinor into left and right chiral states, the Dirac mass term for the neutrino has a form

$$\mathcal{L}_D = -m_D(\bar{\psi}_L\psi_R + \bar{\psi}_R\psi_L) \quad (1.13)$$

The non-zero Dirac mass requires the particle to have both right-handed and left-handed chiral states, and initially it was assumed that neutrinos are massless because neutrinos are only observed in the chiral left-handed state. However, we now know that neutrinos have mass, and therefore the

two options are possible. The first option is that the neutrino has a right-handed chiral state that appears only in Standard Model and does not participate in weak interaction, and therefore cannot be observed (sterile neutrino). The Lagrangian for such mass for a Dirac neutrino field  $\nu = \nu_R + \nu_L$  has a form<sup>39</sup>:

$$\mathcal{L}_{mass}^D = -m\nu\bar{\nu} = -m(\bar{\nu}_R\nu_L + \bar{\nu}_L\nu_R) = -m\bar{\nu}_R\nu_L + \text{hermitian conjugate.} \quad (1.14)$$

The second option is that neutrino, being a neutral fermion, could acquire mass through the Majorana mass mechanism instead of Yukawa coupling to the Higgs field.

If  $\hat{C}$  is the charge conjugation operator that turns a particle state into an antiparticle state:  $\hat{C}|\psi\rangle = C|\bar{\psi}\rangle$ ,  $\psi$  is a particle wavefunction,  $\psi^c$  is its charge conjugated partner, and  $C$  is a charge conjugation eigenvalue, then the right-handed component  $\nu_L^c$ :

$$\nu_L^c = C\bar{\nu}_L^T \quad (1.15)$$

The Majorana mass then would have the form

$$\mathcal{L}_{mass}^M = -\frac{1}{2}m\bar{\nu}_L^c\nu_L + \text{hermitian conjugate.} \quad (1.16)$$

And the factor of a half is addressing double-counting because of identical property hermitian conjugate.

Assuming, that right-handed neutrino exists and interacts only with the Higgs field,

$$\begin{aligned} 2\mathcal{L}_{mass} &= L_L^D + L_R^D + L_L^M + L_R^M + \text{hermitian conjugate} = \\ &= m_D\bar{\nu}_R\nu_L + m_D\bar{\nu}_L^c\nu_R^c + m_L\bar{\nu}_L^c\nu_L + m_R\bar{\nu}_R^c\nu_R + \text{hermitian conjugate.} \end{aligned}$$

This equation can be written in matrix form, with first vector containing only right-handed chiral

states, and the second vector - only the left-handed fields:

$$\mathcal{L} \sim \begin{pmatrix} \bar{\nu}_L^c & \bar{\nu}_R \end{pmatrix} \begin{pmatrix} m_L & m_D \\ m_D & m_R \end{pmatrix} \begin{pmatrix} \nu_L \\ \nu_R^c \end{pmatrix} + \text{hermitian conjugate.} \quad (1.17)$$

After procedure of diagonalization, and substituting  $m_L = 0$  (Standard Model) and  $m_R \gg m_D$  (close to the mass values of quarks and charged leptons), we get mass eigenstates  $m_1$  and  $m_2$ :

$$m_1 = \frac{m_D^2}{m_R}, \quad m_2 = m_R \left(1 + \frac{m_D^2}{m_R}\right) \approx m_R \quad (1.18)$$

With this approximation, the mass  $m_2$  of neutrino  $\nu_2$  is very large, and the mass  $m_1$  of  $\nu_1$  is very low, and therefore, the  $\nu_1$  is our left-handed Majorana neutrino, and  $\nu_2$  is a right-handed sterile neutrino.

This is called the see-saw mechanism<sup>40</sup> that is one explanation for why the neutrino mass is significantly smaller than masses of the other particles, such as charged leptons. Since charge leptons have Dirac masses or the order of 1 MeV, then, if the Dirac mass of neutrino was in similar range, then the mass of right-handed state would be of about  $10^{15}$  eV. Such a large mass makes it impossible for us to create such a particle - such particle would have been created early in the Universe and would no longer exist in a stable state.

Considering all of the above, we can derive three implications of the neutrino mass:

1. If neutrino is a Dirac particle, then the right-handed chiral neutrino state should exist. However, it does not interact with matter and is not detectable. This is why it is called sterile neutrino.
2. On the other hand, if neutrino is a Majorana particle, i.e. it is particle and its own antiparticle at the same time, the mass term couples left-handed state with right-handed state which would lead to the violation of lepton number.
3. In the case of Majorana particle, a very light mass of neutrino can be justified after introducing a very heavy Majorana neutrino through the see-saw mechanism. It would also mean that the

CP violation during decay of this heavy neutrino, could be responsible for baryon asymmetry in the first seconds of the Universe.

### 1.3.2 Sterile Neutrinos

If right-handed chiral neutrino states exist, as was discussed in Section 1.3.1, they will not interact with matter through the weak force (comparing to the left-handed neutrinos that we can observe through this interaction). Therefore, right-handed neutrinos would be "sterile", or "inert". The existence of right-handed neutrino would allow Standard Model to explain the generation of neutrino mass, to understand the significant difference in masses between neutrinos and charged leptons or quarks, and to understand the matter-antimatter asymmetry of the Universe.

The sterile neutrinos, if they exist, would mix with other flavors, and some experiments suggest that the mass of light sterile neutrinos  $\nu_4(\nu_5)$  would be at the eV-scale  $m_4(m_{4,5}) \sim 1eV^1$ . Experiments like LSND<sup>41</sup>, Karmen (1 and 2)<sup>42</sup>, MiniBooNE<sup>43;44</sup> were developed to search for sterile neutrinos at short baselines. For example, LSND experiment<sup>41</sup> that studies  $\bar{\nu}_\mu \rightarrow \bar{\nu}_e$  appearance, reported a significant excess of events. MiniBooNE experiment, that looked at  $\bar{\nu}_\mu \rightarrow \bar{\nu}_e$  and  $\nu_\mu \rightarrow \nu_e$  reported a  $2.8\sigma$  excess of events in the energy range of  $200 < E_\nu < 1250$  MeV<sup>44</sup> in the antineutrino mode, and  $3.4\sigma$  excess of events in the same energy range in neutrino mode<sup>43</sup>. These excess reports do not comply with 3-flavors mixing oscillation theory. Radioactive neutrino source measurements of the experiments GALLEX<sup>45</sup> and SAGE<sup>46</sup> found of deficit in measured fluxes - so-called "Gallium Anomaly". Finally, multiple reactor neutrino experiments observed "reactor antineutrino anomaly" that is discussed in more details in Section 1.4.

According to what was said in Section 1.2.2 about probability of neutrino survival, and with the approximation for short baselines, the probability of  $\bar{\nu}_e$  to survive in 3+1 model (where  $\bar{\nu}_4$  is a sterile antineutrino) will have the form:

$$P(\bar{\nu}_e \rightarrow \bar{\nu}_e) = 1 - \sin^2(2\theta_{14})\sin^2\left(1.27\Delta m_{41}^2 \frac{L[m]}{E_\nu[MeV]}\right) \quad (1.19)$$

where  $\theta_{14}$  is the mixing angle between states 1 and sterile state 4, and  $\Delta m_{41}^2$  is the mass-splitting

between these two states.

## 1.4 Reactor Experiments and Reactor Neutrino Anomaly

### 1.4.1 Overview of Reactor Experiments

Electron antineutrinos are born in nuclear reactor as a result of nuclear fission processes. Nuclear reactors are not only copious but also isotropic source of neutrinos: about  $6 \bar{\nu}_e$  per fission means that a  $1 \text{ GW}_{th}$  reactor can produce about  $2 \times 10^{20} \bar{\nu}_e/\text{sec}$ . The majority of nuclear reactors use as a fuel  $^{235}\text{U}$ ,  $^{239}\text{Pu}$ ,  $^{241}\text{Pu}$ , and  $^{238}\text{U}$ . The schematic multi-step fission process from  $^{235}\text{U}$  fission is shown in Figure 1.2.

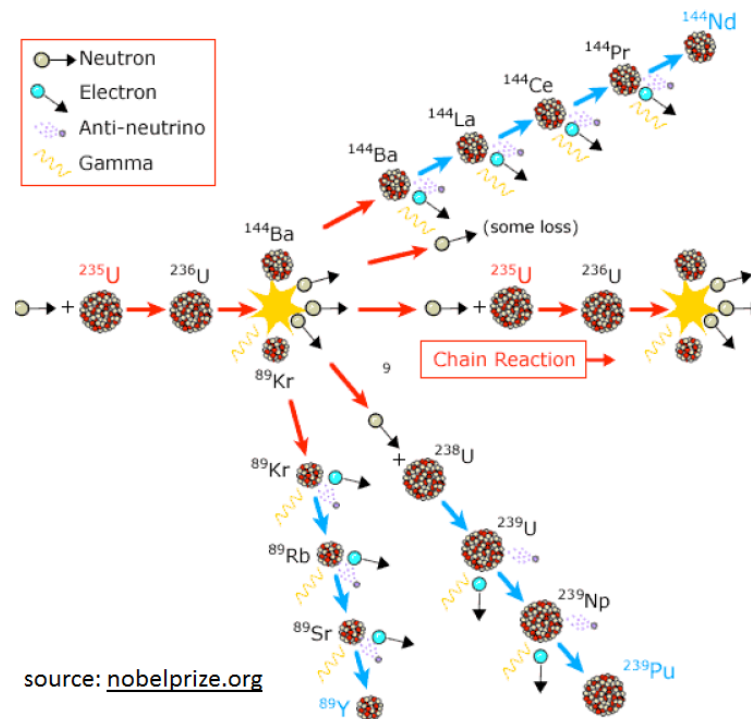


**Figure 1.2:** Scheme of fission reactions in the nuclear reactor with  $^{235}\text{U}$  fuel.

Since reactors produce electron antineutrinos, it is predominantly the inverse beta decay (IBD) mechanism that is used to detect those neutrinos. In this charged current reaction mediated by the weak transmission of  $W^+$  boson, the  $\bar{\nu}_e$  is quasi-elastically scattered on a proton which produces

two signals: so called "prompt" signal (positron) and so-called "delayed" signal (neutron):

$$\bar{\nu}_e + p \rightarrow e^+ + n. \quad (1.20)$$

This interaction has a threshold, where for this interaction to occur, the neutrino energy has to have energy higher than  $E_{\bar{\nu}_e}^{thr}$ :

$$E_{\bar{\nu}_e}^{thr} = E_{e^+} + T_n + (M_n - M_p) \simeq E_{e^+} + 1.293 \text{ MeV} = T_{e^+} + 1.806 \text{ MeV}. \quad (1.21)$$

Therefore, the threshold neutrino energy is  $E_{\bar{\nu}_e}^{thr} = 1.806 \text{ MeV}$ .

Total IBD cross-section was obtained from multiple reactor short-baseline experiments and has the form<sup>47;48</sup>:

$$\sigma_{\text{IBD}} = \left( \frac{2\pi^2}{f\tau_n m_e^5} \right) E_{e^+} p_{e^+} \quad (1.22)$$

where  $f$  is a neutron decay phase space-factor  $f = 1.7152$ , and  $\tau_n$  is the mean neutron lifetime  $\tau_n = 880.3 \text{ s}$ . To obtain the detected IBD spectrum we need to convolve the emitted spectrum with IBD cross-section, as shown in Figure 1.3. The detected spectrum would have the form with a peak around 3.5 MeV. About 75% of reactor antineutrinos have energies below the IBD energy threshold, and therefore cannot be detected with the detector utilizing IBD reaction.

To obtain theoretical prediction for flux and spectrum of reactor neutrino emission, historically there were used 2 methods<sup>49;50</sup>. In the first method the summation is done over the  $\bar{\nu}_e$  spectrum with corresponding weights of each  $\beta$ -decay branch of all fission fragments that are taken from the existing nuclear database. However, the incomplete database will give large uncertainties and variations in the shape and normalization of reactor flux. The second, more empirical method, considers a measured cumulative electron spectrum from the  $\beta$ -decays of all fission constituents of the fuel isotopes. This cumulative electron spectrum was measured in 1980s at the Institute Laue-Langevin (ILL) in France for  $^{235}\text{U}$ ,  $^{239}\text{Pu}$ , and  $^{241}\text{Pu}$  bombarded with thermal neutrons and

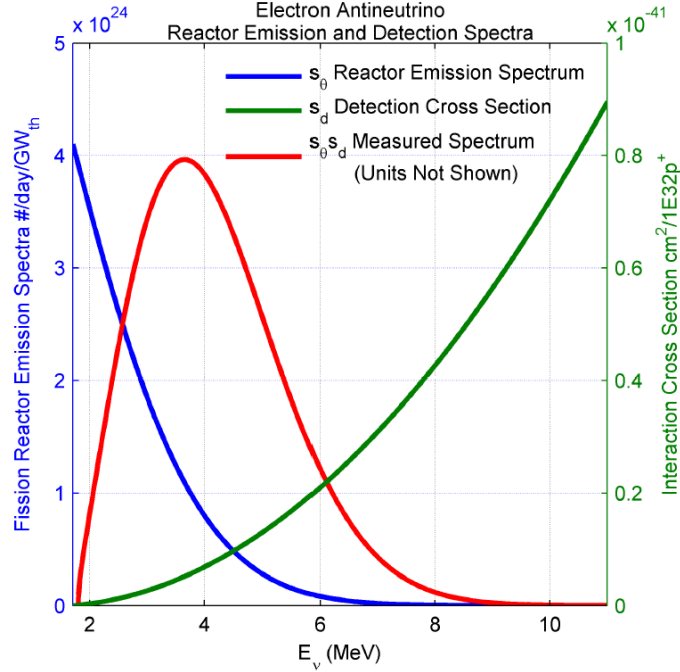


**Figure 1.3:** Reactor emission and measured spectra. The measured spectrum ( $s_0 \cdot s_d$ , red) is obtained via multiplying of emitted spectrum from the reactor ( $s_0$ , blue) by the detection IBD cross-section ( $s_d$ , green)<sup>5</sup>.

converted to  $\bar{\nu}_e$  spectra<sup>51</sup>.  $^{238}\text{U}$  cumulative electron spectrum was measured in 2014 at the scientific neutron source FRM II in Germany<sup>52</sup>.

The antineutrino spectrum in nuclear reactors will be calculated with<sup>53</sup>:

$$S(E_{\bar{\nu}_e}) = \frac{W_{th}}{\sum_i (f_i/F) e_i} \sum_i \frac{f_i}{F} \left( \frac{dN_i}{dE_{\bar{\nu}_e}} \right). \quad (1.23)$$

Here,  $W_{th}$  is the thermal power of the reactor,  $f_i$  is the number of fissions from actinide  $i$ ,  $e_i$  is the effective energy released per fission,  $F$  is the total number of fissions, and  $dN_i/dE_{\bar{\nu}_e}$  is the cumulative antineutrino spectrum of  $i$ -th isotope normalized per fission. Only  $^{235}\text{U}$ ,  $^{239}\text{Pu}$ ,  $^{241}\text{Pu}$ , and  $^{238}\text{U}$  nuclear isotopes are considered. The fission fractions  $f_i/F$  are the most dynamic values as they depend on the fuel evolution in the reactor, and on average those values in low-enriched uranium (LEU) reactors are about 58% of  $^{235}\text{U}$ , 29% of  $^{239}\text{Pu}$ , 5% of  $^{241}\text{Pu}$ , and 8% of  $^{238}\text{U}$ <sup>54</sup>. Currently, the theoretical predictions for  $^{235}\text{U}$ ,  $^{239}\text{Pu}$ , and  $^{241}\text{Pu}$  come from the Huber conversion<sup>55</sup>, and for  $^{238}\text{U}$  for Mueller's *et al.*'s *ab initio* calculation<sup>20</sup>.

The IBD reaction in scintillator has multiple advantages to distinguish the neutrino signal from the background. The prompt positron and delayed neutron produce two signals with different energy tags, separate with specific pre-known time and distance differences - they are called correlated pair of events. In the scintillator, positron ionizes the scintillator and then quickly annihilates with an electron with producing two  $\gamma$ -rays of 511 keV each. Those photons will then undergo Compton scattering on electrons that will produce scintillation light. The signal is called "prompt" because it happens fast - on the order of nanoseconds. Since the neutron recoil is so small (about 40 keV), the positron is the particle that carries the main neutrino kinetic energy, and therefore the energy of neutrino can be reconstructed as

$$E_{\bar{\nu}_e} = E_{\text{rec}} + (E_{\bar{\nu}_e}^{\text{thr}} - E_{\text{rec}}^{\text{thr}}) = E_{\text{rec}} + 0.78 \text{ MeV} \quad (1.24)$$

where the value of 0.78 MeV is obtained after subtracting two annihilation  $\gamma$ -rays from 1.806 MeV.

The delayed signal in IBD-pair is the capture of neutron on the media of the scintillator. These neutrons, born in IBD reaction are thermal, and therefore can react with nuclei in the scintillator with high enough cross-section such as  $^1\text{H}$ ,  $^6\text{Li}$ , or  $\text{Gd}$ , depending on the type of scintillator. The time tag of the neutron capture is typically of the order of  $\mu\text{s}$ , and specific distance tag between prompt and delayed signals is also present.

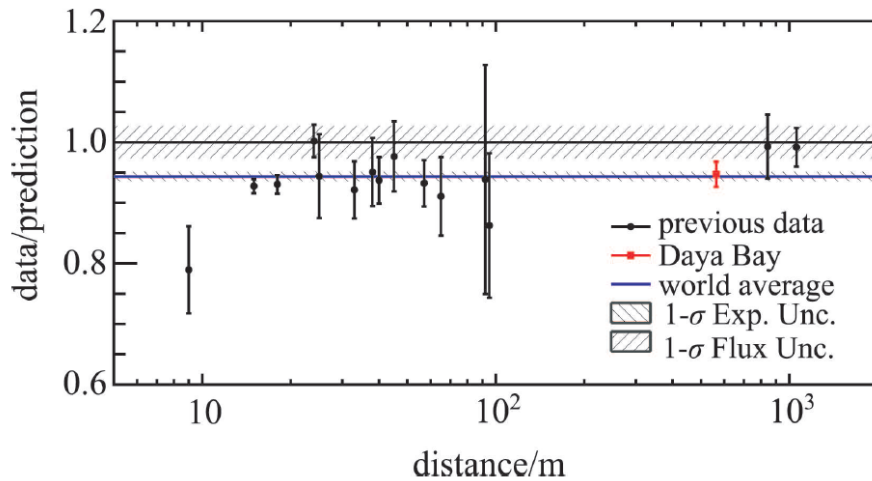
The experiments with reactors can be shortly defined into two categories: short-baseline (O(1 km)) and medium-baseline (O(10~100 km)). The target of short baseline experiments typically is measurement of  $\theta_{13}$ , measurement of  $\Delta m_{31}^2$  and  $\Delta m_{32}^2$ , investigation of reactor flux and spectrum anomalies, and search for sterile neutrinos. The goal of medium-baseline experiments is determination of correct mass-ordering and measurement of  $\theta_{12}$  and  $\Delta m_{21}^2$ .

Numerous short-baseline experiments demonstrated the flux measurements comparing to the theoretical flux predictions. Those experiments demonstrated deficit in the experimental measurements of reactor antineutrino flux, thus proving the existence of neutrino oscillations, and that  $\theta_{13}$  is not zero. Double Chooz reactor experiment in France discovered the deficit at distance  $L \sim 1.1$

km<sup>56</sup>. Daya Bay experiment in China demonstrated the strong evidence for neutrino disappearance at  $L \sim 1.65$  km with statistical significance  $5.2 \sigma$ <sup>57</sup>, and RENO experiment in South Korea reported disappearance at  $L \sim 1.38$  km at  $4.9 \sigma$  significance<sup>58</sup>. Double Chooz reported more evidence at  $2.9 \sigma$  later in<sup>59</sup>, and Daya Bay and RENO experiments updated their reports with better statistics in<sup>60;61</sup>.

### 1.4.2 The Reactor Antineutrino Spectrum and Flux Anomalies

The "reactor neutrino anomaly" (RAA) is a deficit of measured antineutrino rates in comparison to the theoretical prediction at short distances ( $< 100$  m). With the improved recalculated theoretical predictions for reactor antineutrino flux from 2011<sup>20</sup> it was discovered that the mean ratio of the measured rates to predicted rates is  $0.943 \pm 0.023$  which results in a deviation from one at 98.6% C.L.<sup>19</sup>. This deficit is shown in Figure 1.4 for multiple experiments, including Daya Bay, RENO and Double Chooz. An updated measurement of reactor antineutrino flux vs fuel composition with Daya Bay suggested that the primary source for RAA can be <sup>235</sup>U part of the fuel<sup>62;63</sup>.



neutrino is the reason for the RAA anomaly, it has to mix with Standard Model neutrinos and have high frequency oscillations which can be seen in Figure 1.5.

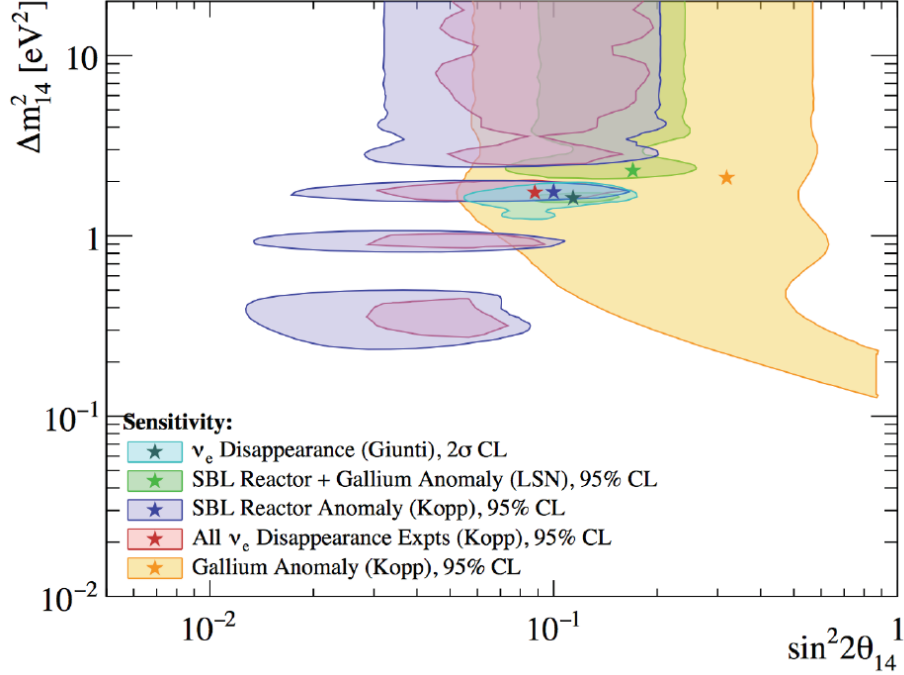


**Figure 1.5:** Oscillation parameter space for sterile neutrinos in 3+1 model suggested for Reactor Neutrino Anomaly<sup>7</sup>.

Another anomaly, observed in reactor experiments is the anomaly in the spectrum shape in the energy around 5 MeV shown in Figure 1.6. Although the agreement with the predicted spectrum was obtained for other energy regions, the local significance of the excess of events for window 4-6 MeV had p-value of  $9.7 \times 10^{-6}$  ( $4.4 \sigma$ )<sup>6</sup>. Experiments in Daya Bay<sup>62</sup>, RENO<sup>67</sup>, and Double Chooz<sup>68</sup> observed an excess of  $\bar{\nu}_e$  in this energy region with respect to theoretical model. It was found that this excess rate depends on the power of the reactor and is stable in time, which makes a hypothesis of some unknown background unlikely. Sterile neutrinos cannot explain this anomaly.

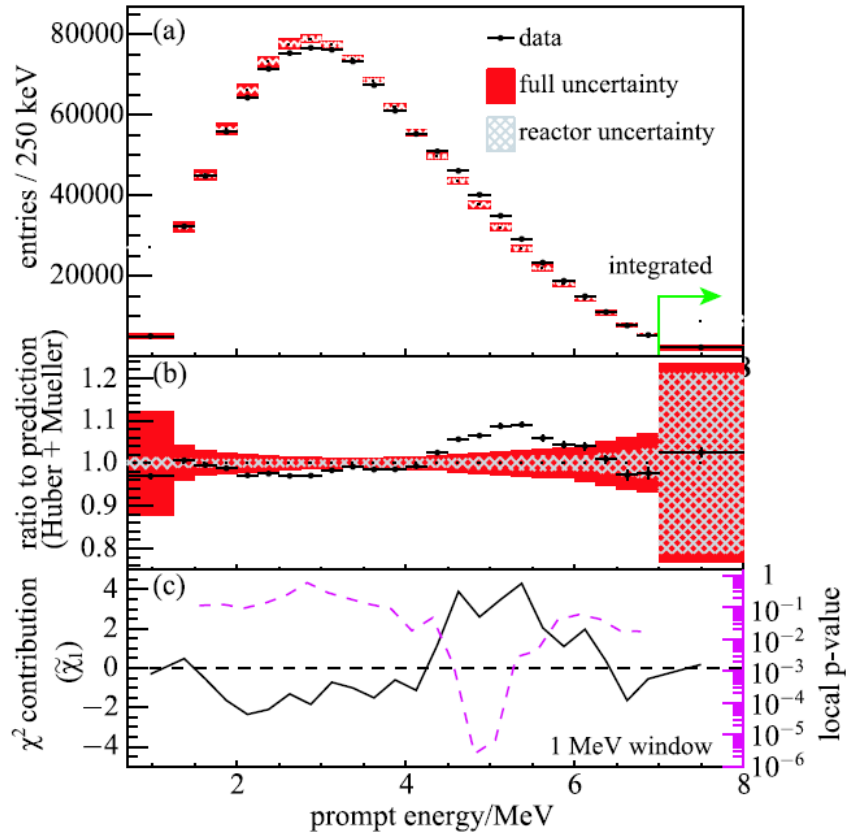


**Figure 1.6:** (a) Daya Bay comparison for measured reactor spectrum in comparison to theoretical predictions (Huber/Mueller model). (b) Ratio of predicted and measured events that shows bump in the region 4-6 MeV. (c)  $\chi^2$  distribution showing abnormality in the same energy range<sup>6</sup>.

## Chapter 2: The PROSPECT Experiment

### 2.1 Goal, Idea and Design

The Precision Reactor Oscillation and Spectrum Experiment (PROSPECT) has the goal to address both reactor antineutrino anomaly of flux deficit and spectrum anomaly in the energy range of 4-6 MeV. To implement the first goal, PROSPECT performs a search for oscillations of eV-scaled sterile neutrinos independently of reactor model. To address the second goal, PROSPECT conducts precise measurements of a reactor  $^{235}\text{U}$  spectrum.

The PROSPECT-I detector was constructed at Yale University and transported and mounted in close proximity (7-12 m) to the High Flux Isotope Reactor (HFIR) at Oak Ridge National Laboratory. A special segmented design of the detector allows to make search of sterile neutrino oscillations within the detector itself independent of the shape of reactor neutrino model. A  $^6\text{Li}$ -loaded liquid scintillator allows to utilize pulse shape discrimination (PSD) mechanism for better detection of a signal from the background. The experiment intentionally works with  $^{235}\text{U}$ -reactor to isolate reactor spectral shape of this isotope to investigate its role in spectrum anomaly in the energy range 4-6 MeV. In addition, the high-resolution measurement of spectral shape can provide an important dataset for nuclear databases and future experiments.

To successfully decouple signal from background, PROSPECT utilized sophisticated system of protective shielding as well as principles of detection. One of these principles is to measure spectrum both when reactor is working and when reactor is shut down for subtraction of the background from the mix of signal + background. PROSPECT also utilizes in its analysis IBD mechanism which allows to get clear signal due to signature of prompt and delayed events. Finally, PROSPECT uses a special procedure of vetoing of events that can be connected to cosmogenic background.

PROSPECT-I successfully and efficiently detected thousands of electron antineutrinos from nuclear reactor and performed oscillation and spectrum analysis based on multiple months dataset.

### 2.1.1 High Flux Isotope Reactor

HFIR reactor is a research compact reactor with a nominal thermal power of  $85 \text{ MW}_{th}$ . It is located in the concrete building in Oak Ridge National Laboratory in Tennessee at altitude of about 250 m. HFIR consists of two concentric cylindrical rings with plates of  $^{235}\text{U}$  fuel in between them (Figure 2.1). The enrichment of  $^{235}\text{U}$  reaches 93%, and 99% of electron antineutrino are born from this isotope<sup>8</sup>. The outer diameter of cylinder 0.435 m, and the height is 0.508 m.

HFIR operates in cycles with each reactor cycle of about 24 days. During this cycle the fuel is burnt out and the new fuel is being replaced while the reactor is turned off. The reactor is located in the water pool of a height of 8 m. When the fuel is replaced, sometimes the water level in the pool is lowered down to 5 m for facility workers to get access to some areas in the reactor. The water lowering does not happen regularly and at maximum can take only a few days, usually - shorter. The spent fuel elements are stored in another water pool just next to reactor core water pool. The periods when the reactor is shut down were used by PROSPECT to measure the background for later subtraction.

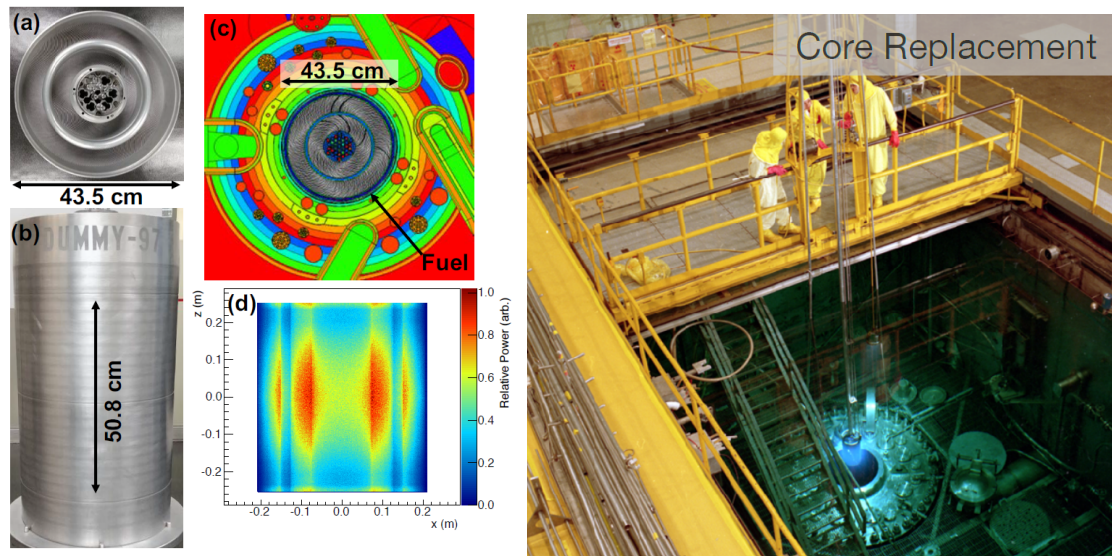


**Figure 2.1:** Left: (a, b) Photograph of a HFIR reactor. (c) The drawing of the active fuel. (d) The power distribution of the reactor in 2D projection<sup>8</sup>. Right: replacement of a reactor core during reactor shutdown.

### 2.1.2 Detector Design

The PROSPECT detector consists of the inner part with liquid scintillator and layered system of shielding. The structure of shielding is discussed in details in Chapter 4, and here we will discuss the structure of inner part of the detector.

For performing a successful reactor model independent search for sterile oscillations, the design of PROSPECT detector consists of an array of elongated optical segments with PMTs on each end. The cutaway of the detector is shown in Figure 2.2. Active volume is filled with 3760 l of  ${}^6\text{Li}$ -loaded organic scintillator. The inner volume is confined with the inner acrylic containment tank. The inner volume is divided into an optical array of  $14 \times 11$  segments with independent double PMT readouts. Overall, the optical grid was designed and manufactured from light materials supported with plastic 3D-printed hollow support rods. The choice of light materials was intended to improve the energy response of the detector. By keeping the amount of dead materials low, the lesser loss of energy was achieved. Another goal of the design was also its ability to perform *in situ* radioactive and optical calibration measurements by inserting the strings with calibration sources inside the rods and being able to move them along the detector (Figure 2.2). Figure 2.3 shows the pinwheels: structural low-mass plastic 3D-printed pieces from which the optical grid was made. It also shows the fiber optic assembly that goes inside the hollow pinwheels.

Figure 2.4 shows one individual PROSPECT segment with optical grid on the corners supporting optical separators and giving shape for the structure. Each segment has a double-ended PMT readout. There were two kinds of PMTs used in PROSPECT design: Hamamatsu R6594 SEL(Hamamatsu) and ADIT Electron Tubes 9372KB(ET). Each PMT was inserted into acrylic box, called housings, and housings were filled with mineral oil in order to be compatible with the liquid scintillator from outside of the housings and reduce background noise (Figure 2.5). The space between the outer surface of the PMT and inner surface of the housing was filled with conical reflector that allowed for better collection of light between square cross-section of housing, and circular cross-section of PMT.

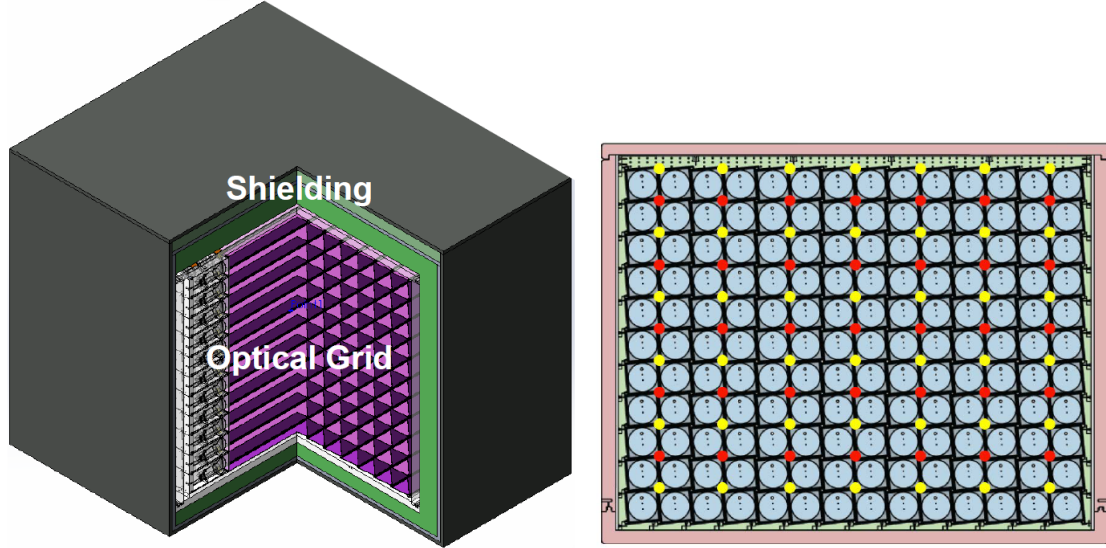


**Figure 2.2:** Left: Cutaway schematic drawing of a detector showing the optical grid and array of segments. Right: A cross-section of the PROSPECT detector showing the locations of inserting calibration sources (red) and optical insert (yellow)<sup>8</sup>

The inner detector structure was inserted into inner acrylic tank with lid on the top and a slab at the bottom. Both the tank and the bottom slab have grooves for sealing with two Viton O-rings. The tank is filled with liquid scintillator and sealed. A system of check the pressure differential between inside and the outside containment vessel allows to check for leaks in the detector.

### 2.1.3 $\bar{\nu}_e$ Detection Strategy

The PROSPECT experiment utilizes IBD reaction in  ${}^6\text{Li}$ -loaded liquid organic scintillator to detect electron antineutrinos. The liquid scintillator was developed by PROSPECT collaboration and is based on the commercial EJ-309 organic solvent, meeting HFIR requirements of being non-flammable and of low toxicity. It achieved a high light yield and a high PSD capability. Due to these characteristics, the experiment obtained a good energy resolution ( $4.5\%/\sqrt{E(\text{MeV})}$ ) and excellent ability to distinct electronic and nuclear recoil bands.

In the IBD reaction, electron antineutrino interacts with a proton inside the detector and produced a correlated pair of prompt and delayed signals.

$$\bar{\nu}_e + p \rightarrow e^+ + n. \quad (2.1)$$

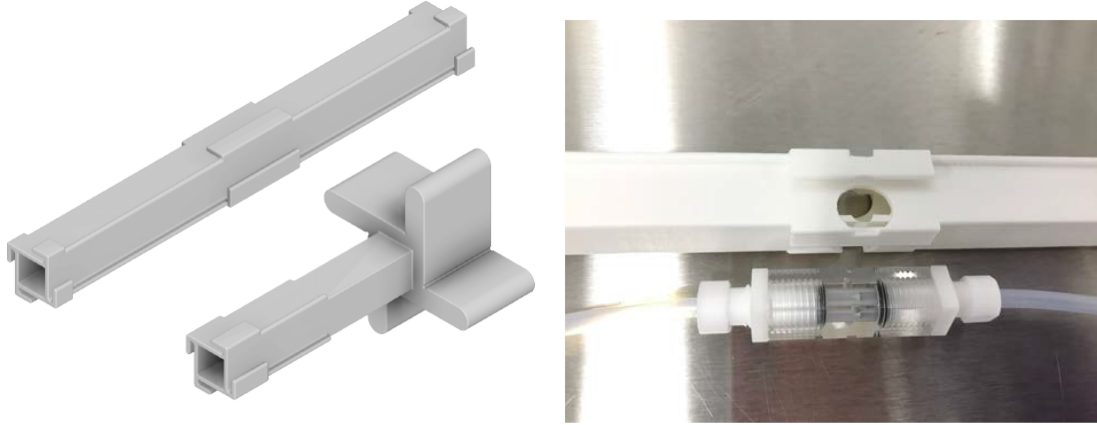


**Figure 2.3:** Left: Central and end pinwheels - plastic 3D-printed pieces consisting the optical grid; Right: Example of fiber optic assembly that would be inserted into central pinwheel<sup>8</sup>

The prompt signal is a positron from the right side of equation that after being born quickly deposits its kinetic energy in form of ionization of the scintillator and annihilates with electron producing two  $\gamma$ -quants of the energy of 511 keV each. The signal detected by PMTs is of low ionization density and is extended in topology (tens of centimeter)<sup>10</sup>.



For the neutron, on the other hand, it takes longer time while it thermalizes via scattering of the protons and finally gets captured on a  ${}^6\text{Li}$  (or hydrogen) atom of liquid scintillator. The atom decays into a triton ( ${}^3\text{H}$ ) and alpha particle ( ${}^4\text{H}$ ) of kinetic energies of 2.05 MeV and 2.75 MeV. Tritium and alpha-particle quickly deposit their energies in the scintillator creating another registered signal. This signal is compact (of  $\mu\text{m}$  range) and of very high ionization density. It is called delayed signal due to its delayed nature comparing the first, prompt signal.



The prompt and delayed signals have specific energy tags and time difference of  $t < 100 \mu\text{s}$ . Together with PSD properties of the liquid scintillator and dimensional analysis it provides efficient

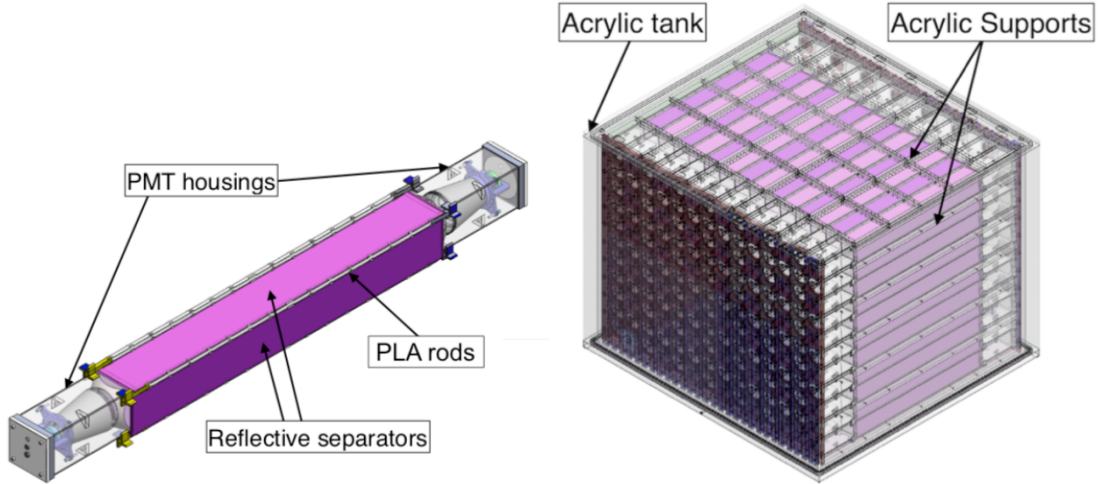


**Figure 2.4:** Schematic drawing of detector segments. Left: the individual segment with double-ended PMT-readout. Right: the inner detector that is enclosed by the inner acrylic tank<sup>8</sup>.

background rejection. The schematic representation of the reaction is shown in Figure 2.6.

The pulse shape discrimination or PSD is a scintillator property that allows it to discriminate between different particles. The property is calculated through the formula:

$$PSD = \frac{Q_{tail}}{Q_{full}} \quad (2.4)$$

where  $Q_{tail}$  is the amount of charge in the PMT pulse tail and  $Q_{full}$  is the amount of total integral charge as shown in Figure 2.7. Through introducing this PSD metrics we can identify electric recoils as low  $dE/dx$ , and nuclear recoils as high  $dE/dx$ . The PSD property of a liquid scintillator and corresponding analysis allows to reach significantly better background rejection. It is especially important technique for ground experiment located in the very high proximity to the nuclear reactor with no appreciable overburden.

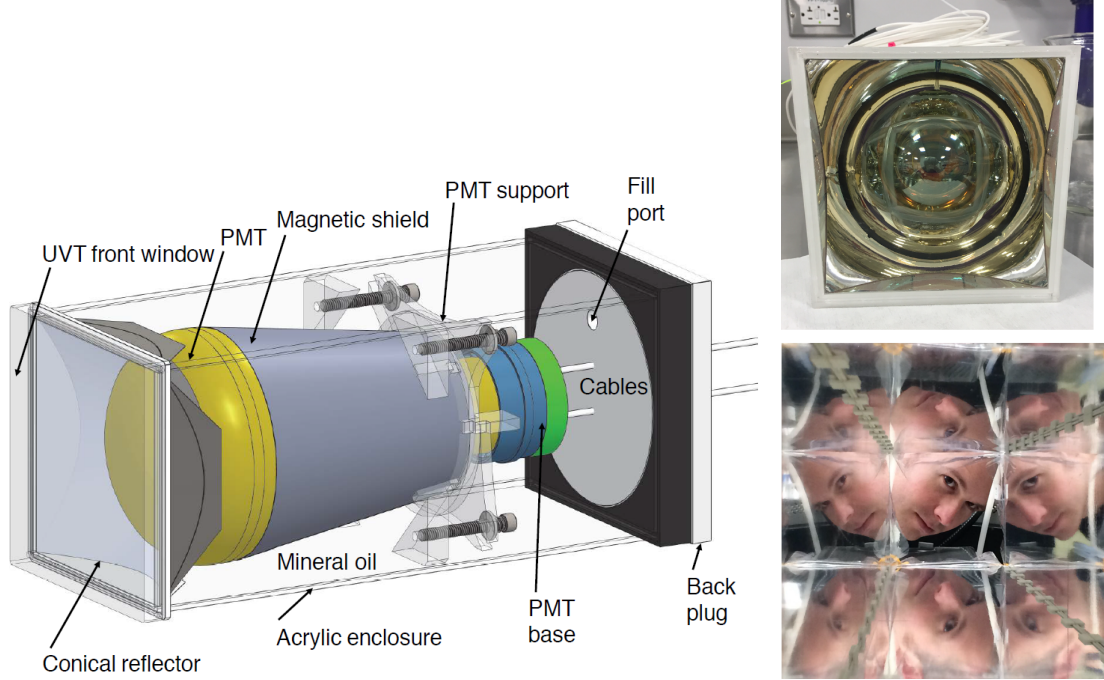


**Figure 2.5:** Left: Schematic drawing of PMT in the housing. Right: photo of a single PMT in the housing.

#### 2.1.4 Oscillation Search Strategy

To perform a successful search for sterile neutrino oscillations, PROSPECT utilizes the segmented design of the detector. Figure 2.8 illustrates that geometrically each segment is located at different distance from the reactor, so that electron antineutrino has to travel different distance to reach the segment. If sterile neutrino oscillations exist, there would be different probability of electron antineutrino to survive avoiding the oscillation, defined with the formula:

$$P_{ee} = 1 - \sin^2 2\theta_{14} \cdot \sin^2 \left( 1.27 \cdot \Delta m_{41}^2 \frac{L}{E} \right) \quad (2.5)$$

Since each segment has individual PMT-readout, we can measure the spectra individually at each segment. For better statistics, the spectra are combined for different baseline bins depending on the baseline from the detector, and those spectra are compared to each other to construct a map of possible oscillations for different parameters  $\theta_{14}$  and  $\Delta m_{41}^2$ . Figure 2.9 (left) shows theoretical model of the shape of the spectrum with oscillations for different PROSPECT baselines comparing

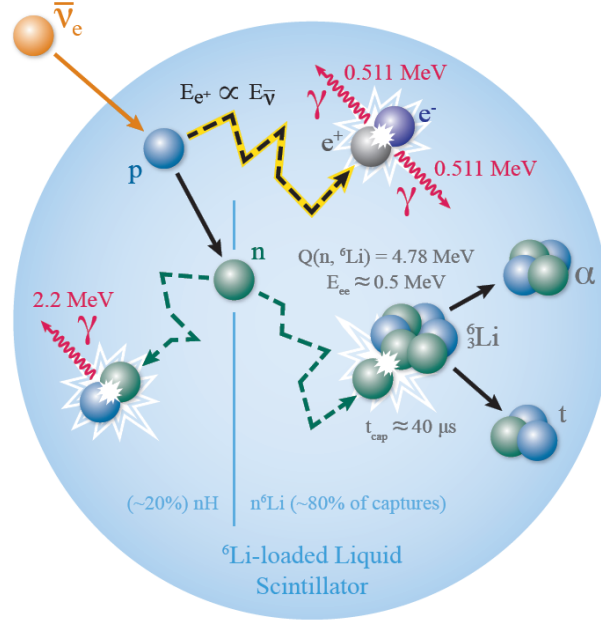


**Figure 2.6:** A schematic picture explaining the detection of  $\bar{\nu}_e$  in PROSPECT.

to the null oscillations for the total spectrum. However, to avoid uncertainty related to spectral shape, PROSPECT performs a relative comparison of oscillations. For this, the spectrum at each baseline bin is divided by the spectrum in the whole detector, therefore getting independent result from underlying reactor flux and spectrum models. The MC theoretical model results is shown in Figure 2.9 (right).

### 2.1.5 Achieved Parameters

The total target mass of PROSPECT antineutrino detector reached 3680 kg, while fiducialized mass was 2581 kg. Dead structural material reached 3.4% of the total mass of the detector. PROSPECT detector has excellent energy resolution of 4.5% at 1 MeV. Position resolution along x and y axis (cross section of the segments) reached 15 cm (length of a side of a square), and 5 cm along z-axis (along a segment). For the full data-taking period, a total number of  $50560 \pm 406$  (stat) IBD-pairs were detected, and the signal-to-background (cosmogenic/accidental) ratio reached 1.4 / 1.8. This ratio is one of the highest statistics parameter achieved for spectrum of  $^{235}\text{U}$  electron antineutrino<sup>10</sup>.

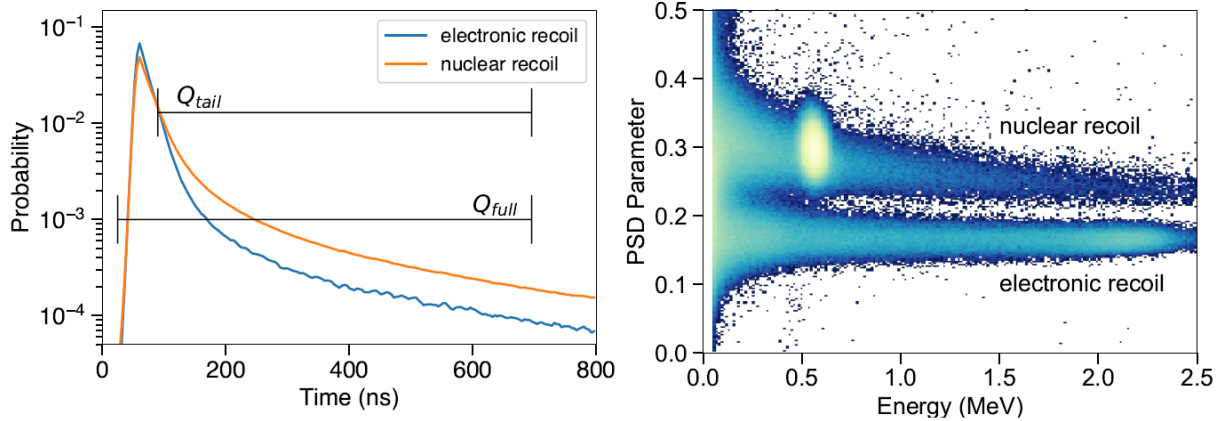


**Figure 2.7:** Left: Template waveforms from the PROSPECT-50 prototype detector showing the different shapes of electronic recoil and nuclear recoil energy depositions in the liquid scintillator. The source that was used is  $^{252}\text{Cf}$ . PSD is a metric that is equal to the fraction of charge in the tail of the pulse to the total integral charge. Right: The distribution of PSD parameters as a function of energy for the same detector and energy source<sup>9</sup>.

## 2.2 Detector Assembly and Installation

Prior to construction of the detector three prototype mini detectors were studied in 2014-2018:

- PROSPECT-2, containing about 2 l of liquid scintillator and mounted at HFIR site for characterization of background and rejection properties of liquid scintillator and passive shielding<sup>7</sup>. The detector was made of a cylindrical acrylic vessel with double-ended PMT readout.
- PROSPECT-20 was a 23 l acrylic cell detector that studied optical performance of a single PROSPECT segment with varying detector components and parameters such as optical separator and PMT configurations. The prototype detector allowed the optimization of light collection and PSD performance<sup>69</sup>. It was built and studied both at Yale University and also placed at HFIR for studying the optical characteristics during on and off reactor statuses.
- PROSPECT-50 consisted of two segments adjacent to each other and filled with 50 l of liquid scintillator. It was built and studied at Yale University. The detector was constructed in multiple iterations for achieving better parameters and improving characteristics. PROSPECT-50 studied parameters of collection of light, PSD and energy resolution. It also measured various parameters for performance of liquid scintillator<sup>9</sup>.

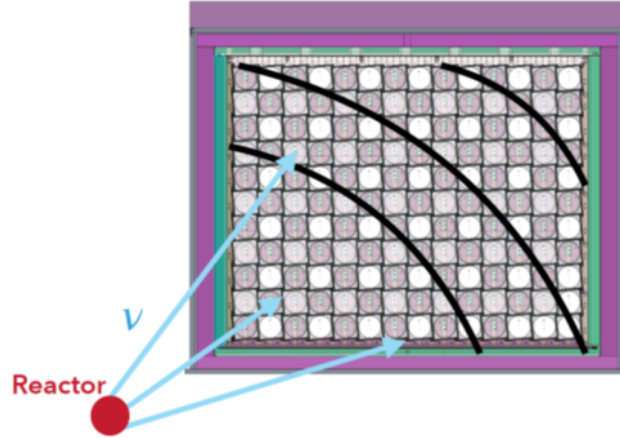


**Figure 2.8:** Different baselines for the reactor

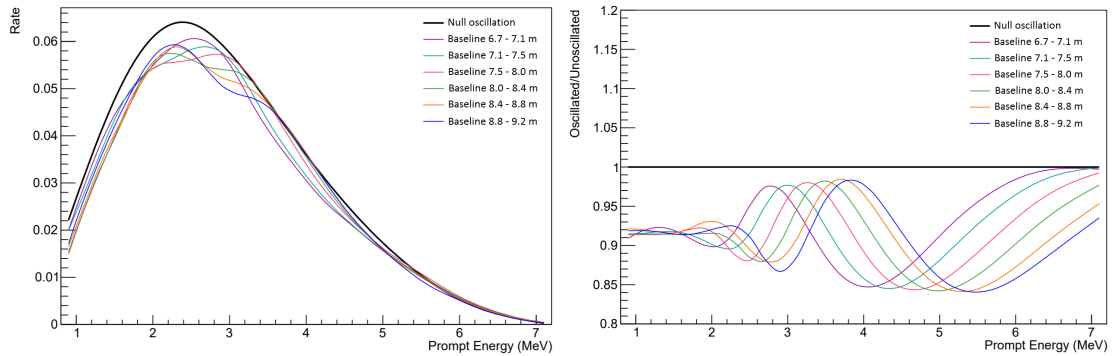


**Figure 2.9:** MC-generated oscillated spectra for different baselines for RAA best-fit point ( $\sin^2 2\theta_{14} = 0.165$ ,  $\Delta m_{41}^2 = 2.39 \text{ eV}^2$ ).

PROSPECT antineutrino detector was constructed at Yale University from November 2016 to January 2018. The insertion of PMTs into the housings and filling them with mineral oil, as well as sealing the electronics was done at Yale University in the clean room with all precautions (Figure 2.10). Inner detector and inserting the detector in the detector package was done in Yale Wright Laboratory. The optical grid and optical separators were prepared at Illinois Institute of Technology. In February 2018, the inner detector was shipped across the country to HFIR in Oak Ridge, Tennessee. At HFIR, the inner tank was filled with liquid scintillator and enclosed by the passive shield. The PROSPECT timeline prior to start taking measurements:

- November 2016 - November 2017: Component construction (PMTs, reflectors, etc.)
- November 2017 - December 2017: Assembly

- December 2017 - January 2018: Dry commissioning at Yale University
- February 2018 - March 2018: Transportation, arriving at ORNL, installation at HFIR
- March 2018 - May 2018: Wet Commissioning
- March 2018 - January 2019: Data taking



**Figure 2.10:** Work on PMTs and optical grid in Yale Wright Laboratory’s clean room.

### 2.3 Data Taking and Detector Evolution

The data taking started on March 5th, 2018 and finished on October 6th, 2018. The analysis covered five HFIR fuel cycles. PROSPECT was in data taking regime for 183 days, and HFIR was on (off) for 105 (78) of that days.

The calibration data-taking spanned 8 days. Finally, 95.6 (73.1) days of reactor-on (reactor-off) days were used for physics analysis. The examples of one of the first hadron event, muon, and IBD candidate as shown on detector display, are shown in Figure 2.11.

Throughout PROSPECT data taking, the detector was undergoing the evolution changes that we refer here as ”ingress”. During this process, it is assumed that the scintillator was leaking into the PMT housings overcoming the sealing. As the scintillator leaked in, the light signal in the detector was multiplying within the housings and leaked into recoil and neutron capture PSD bands resulting in more detected events, especially during reactor on periods.

Ingress was gradually happening with time, the most affecting the bottom of the detector due to pressure on the housings. The least affected areas were the top of the detector. Ingress not only caused the extra rates due to reflections in high PSD band, but was also responsible for instability of the electronics of the most affected PMTs, which resulted in some of the segments being turned off during the data taking, and excluded from the analysis.

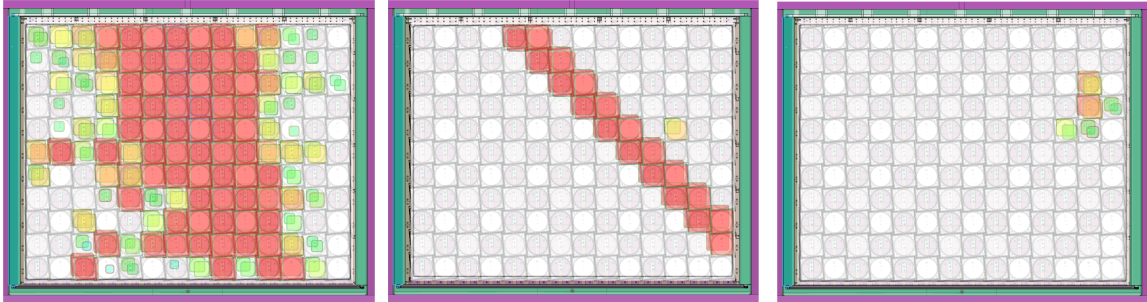


**Figure 2.11:** One of the first displayed detected hadron, muon and IBD-candidate. The color and size indicate how much energy was deposited.

## 2.4 Event Classification

### 2.4.1 Pulse Cruncher

The raw waveforms of the signals collected in the detector have to undergo analysis, that will reconstruct the position, time, energy and pulse shape of the triggering event.

The waveforms, written down in the Data Acquisition (DAQ) System in a special file for location and characterization. The example of one pulse is shown in Figure 2.12. Initial pulse candidates are identified as a sample with one global maximum and with local maxima, if they are present. The negative-polarity waveforms are inverted. After subtraction of a baseline from all samples in the waveform, the global maximum and any local maxima are selected as having at least 30 Analog to Digital Converter (ADC) and more units.

The area of a pulse is calculated as the sum of the samples that lie between 3 samples prior and 25 samples after the pulse's maximum. The time of arrival  $t$  of the pulse is measured at first-level crossing at 50% of pulse's maximum. PSD value is defined as the ratio of the integral under tail vs

integral over the whole pulse, where tail is calculated as integral between 11 and 50 samples after  $t$ , and the total pulse is calculated as the area between 3 and 50 samples after  $t^{10}$ . Those criteria were found through calculation of figure-of-merit for maximising PSD based on neutron captures type of events and  $\gamma$ -rays.

The parameters of all analyzed pulses are written down in HDF5 format. The parameters include arrival time  $t$ , PSD, area  $S$ , baseline  $b$ , and peak height  $h$ . The next step is combining the pulses that happen close in time to the groups of pulses called clusters. The condition of the combining is that the pulses have to have time of arrival  $t$  separated by less or equal to 20 ns. Due to double-ended PMT-readout, pulses that are detected with both PMTs of the same segment are also paired together. They are analyzed together to obtain the main calibrated parameters including time, position, energy, and PSD.

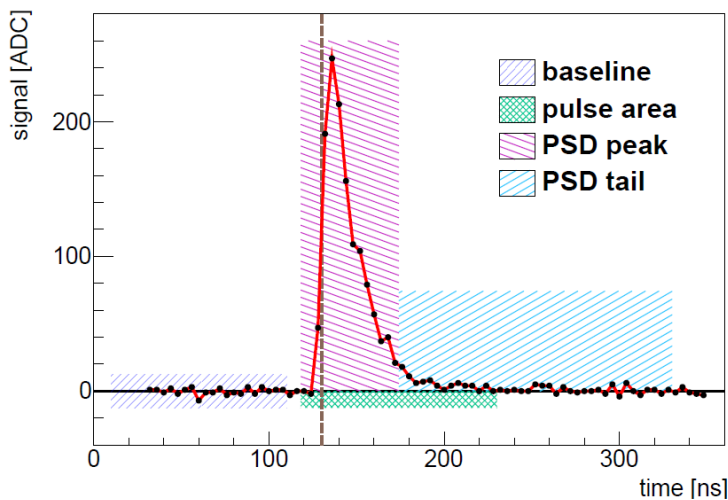


**Figure 2.12:** An example of electron pulse and how it looks into analysis. The dashed vertical line is the half-height leading edge timing. The presented plot is obtained after being inverted and baseline subtracted<sup>10</sup>.

## 2.4.2 Low Level Calibration

Low level calibration includes timing calibration, PSD calibration, position calibration, and energy calibration.

### Timing Calibration

Timing calibration of PMT channels is necessary because of small, but non-negligible variation in two PMTs electronic response at different points in the detector. The calibration is performed with the use of through-going muons tracks. The muon tracks are selected as pulses with a summed pulse ADC area  $S$  above  $10^5$  with having 4 paired segments or more. The muons cross the width of the detector creating a tail of pulses behind it. The energy deposition is typically above  $\sim 15$  MeV. Muons are identified through well-shaped waveform signals at "corner-clipping" track sections. As muons travel across multiple segments, they produce tracks which are almost coincide in time. By using the estimated transit time of muons between segments, the timing is calibrated by minimizing an overdetermined linear system of equation of time variance between each pair of segments. This system of equation consists of time matrices made of two values: the average arrival time  $t^i$  and a timing difference  $\delta t^i$ :

$$t^i = \frac{1}{2}(t_0^i + t_1^i), \quad \delta t^i = t_1^i - t_0^i, \quad (2.6)$$

Here,  $t_0^i$  is the hit time fixed with PMT 0 in segment  $i$ , and  $t_1^i$  is the hit time fixed with PMT 1 in segment  $i$ , and the muon transit time through each segment time is cancelled out.

### PSD Calibration

For each two channels a unified PSD parameter is recalculated from the PSD values of original pulses. This is performed because PSD values have some position dependency we need to extract before getting the average value. The position dependency happens because when the light travels from the ends of the segments toward the center, the scintillation light shifts in time and broadens the PMT pulse. As a result, the PSD tail value was found to be higher at some distance from PMT creating a non-uniformity in the PSD distribution. We can fit this distribution with a formula:  $p \cdot (1 + d \cdot [1 - e^{k\Delta t}])$  and subtract the position-dependent term  $p \cdot d \cdot [1 - e^{k\Delta t}]$  from each pulse, therefore leaving position-independent term only for averaging between 2 PMTs. Before the averaging, the values also get weighted by the number of photoelectrons in the pulse.

Such a procedure is repeated for each segment in each run to find the values of parameters  $p$ ,  $d$ , and  $k$ . With time, the values of  $p$  tend to decrease due to increasing attenuation. This value is used to define PSD-cuts for electron-like events, and neutron capture cuts.

### Position Calibration

The information about the position of the event along  $z$ -axis is found through a relative timing  $\Delta t$  between two PMTs, and their relative signal amplitude. The log of a ratio of pulse areas:  $R = \ln S_1/S_0$  is also used to characterize the position value.

The  $z$  values behaves differently at the location where the active detector values changes. Light transport perturbations in the locations of support rod clips also affect the  $\Delta t$  distribution. The position if fit with the following formula:

$$z = a\Delta t + b(\Delta t)^3 \quad (2.7)$$

Another formula that is used to estimate position through the relative light collection, is dependence of  $R$  on  $\Delta t$ :

$$R = a + b\Delta t + c(\Delta t)^3 \quad (2.8)$$

After performing these two fits, parameters of  $z(\Delta t)$  and  $z(R)$  are inserted into calibration database. Eventual estimate  $z_{rec}$  of the event is calculated from a statistically-weighted average between those two  $z$ -estimates.

The PROSPECT detector evolves in time and so does its optical characteristics. Thus, the detector is being calibrated throughout the whole datataking period. The total timeline was divided into 11 calibration periods for collecting enough statistics in each segment to finely perform  $z$ -calibration.

### Energy calibration

The energy calibration of PROSPECT detector is complicated with scintillator non-linearity, trigger acquisition thresholds, and having multi-segment design. The energy calibration is developed in two

stages: first stage is obtaining the values of visible energy  $E_{vis}$  before PMT gain effects, and second stage is working with Monte-Carlo (MC) simulation and fitting the parameters of detector response. The MC model is aimed to reproduce  $E_{vis}$  values.

$E_{vis}$  is calculated through the formula:

$$E_{vis} = \frac{S_0 n_0 / g_0 + S_1 n_1 / g_1}{n_0 \eta_0(z_{rec}) + n_1 \eta_1(z_{rec})} \quad (2.9)$$

Here,  $S_0$  and  $S_1$  are pulse areas of signals detected with both PMTs,  $z_{rec}$  is a reconstructed  $z$ -position,  $g_0$  and  $g_1$  is the pulse area signal per  $E_{vis}$  that is deposited at the center of the segment, and  $n_0$  and  $n_1$  is the number of photoelectrons (PE) detected per  $E_{vis}$  at the center of the segment, and  $\eta_0(z)$  and  $\eta_1(z)$  is light transport efficiency to each PMT.

The neutron capture on  ${}^6\text{Li}$  has the properties of having the constant energy and being easily distinct from gamma-rays through difference in PSD and time correlations. The gain stabilizing  $g_i$  calibration constants are obtained from this neutron capture events for each run and each PMT. Light transport curves of  $\eta_i(z)$  are also determined through neutron capture signals; however, those are combined into two-weeks datasets for better statistics. Finally,  $n_i$  is determined through the width of neutron capture peak.

All the constants are written down in the calibration database, and while the gain stabilizing constants are calculated for each run, the light transport constants and photoelectron collection constants are calculated from two-weeks combined statistics.

As the time passes, the optical properties of liquid scintillator drop, and  $E_{vis}$  resolution also decreases. To adjust for this effect, the smeared energy  $E_{smear}$  was introduced. Smeared energy is obtained from  $E_{vis}$  through including random fluctuations into  $E_{vis}$  in order to get rid of the resolution equivalent to 325 PE/MeV in each segment during each time period.

### Calibration Performance from Background Events

Finally, another step of calibration included characterization of detector performance through different background events including

- detector-intrinsic ( $^{219}\text{Rn}$ ,  $^{215}\text{Po}$ ) correlated alpha-decays from  $^{227}\text{Ac}$  dissolved into liquid scintillator
- correlated ( $^{214}\text{Bi}$ ,  $^{214}\text{Po}$ ) and ( $^{212}\text{Bi}$ ,  $^{212}\text{Po}$ ) ( $\beta+\gamma$ ,  $\alpha$ ) decays from  $^{238}\text{U}$  and  $^{232}\text{Th}$  decay chains from natural radioactive contamination of the detector
- mono-energetic 2.2 MeV gamma-ray from n-H capture
- gamma-ray peaks from intrinsic  $^{208}\text{Tl}$  contamination in the detector combined with capture of reactor-generated neutrons on metals in HFIR and PROSPECT shielding

### 2.4.3 Cluster Analysis and Event Reconstruction

The higher level analysis is happening at a cluster level, and the events are classified, collected and analyzed in cluster terms. Due to variations in energy response in different segments and thresholds in hardware response, the energy cut for clusters that are allowed to get into analysis is  $E_{smear} > 90$  keV with  $\pm 5$  keV uncertainty. The threshold was obtained after comparison with "Zero Length Encoding" (ZLE) ADC threshold throughout the dataset and the whole detector.

The parameters reconstructed for cluster are derived directly from parameters for pulses described before.

- Cluster time  $T_{rec}$  is the median of  $t_{rec}$  of the individual pulses in that cluster.
- Cluster energy  $E_{rec}$  is obtained through summation of the smear energies  $E_{smear}$  of individual pulses.
- Cluster  $z$ -position  $Z_{rec}$  is calculated as  $z$ -position  $z_{rec}$  of the highest energy pulse in that cluster.
- Similarly, cluster segment number  $S_{rec}$  is the segment number of the highest energy pulse in that cluster.

Cluster segment multiplicity, pulse energies, pulse PSD values,  $z$ -positions, and all other pulse-related parameters are also used for the later analysis for better selection of events.

## Chapter 3: Background for Surface Experiments

### 3.1 PROSPECT Shielding and Background Rejection

The background at the HFIR location can be divided into two main parts: reactor correlated background and the cosmogenic background.

#### 3.1.1 Reactor Related Background

The background from the reactor consists of high-energy gamma-rays and fast neutrons. High-energy gamma radiation above 2.4 MeV is largely dominated by thermal neutron captures. Those captures happen on the materials of the reactor and detectors themselves, as well on the materials surrounding them, such as cooling media. Thermal neutron captures typically yield gamma signals at 6.1 MeV from  $^{16}\text{N}$  and 7.6 MeV from  $^{57}\text{Fe}$ <sup>70</sup>. Fast neutrons, produced by the reactor are born in the process of fission of isotopes. Usually their emission is prevented by neutron shielding around nuclear core. However, the measurement of a fast neutron flux at HFIR location obtained a flux of  $2\text{-}3\text{ cm}^{-2}\text{ s}^{-1}$  with the peak at the range of 1-2 MeV<sup>70</sup>. Reactor related background can be very high in such a close proximity as 7 m; therefore, efficient techniques of passive shielding are necessary in order to not overwhelm the data rates in data acquisition system, and reduce rate of accidental gamma and neutron coincidences that can mimic IBDs. The results of prototype studies showed that layered shielding system is the most efficient in suppression of reactor related background. The following materials are founded to be the best suppressors of the fast neutrons with energies below a few MeV, thermal neutrons and gamma-rays:

- Polyethylene: eliminates neutrons. About 0.6 m of polyethylene suppresses neutrons at 1 MeV with a factor of  $10^{-6}$ <sup>70</sup>.
- A hermetic layer of borated shielding successfully suppresses thermal neutrons due to large thermal neutron cross-section and low gamma-emission of  $^{10}\text{B}$ .

- Lead or other high-Z materials help attenuate prompt neutron-capture gamma-rays. However, lead can also lead to cosmogenic spallation near the active detector volume.

PROSPECT collaboration used these materials to design the passive shielding of the detector. However, weight and space constraints at the HFIR site transformed some original decisions. The optimal lead layers thickness was found to be from 0.05 to 0.1 m<sup>11</sup>; however, 0.025 m lead was used to satisfy the weight constraints.

### 3.1.2 PROSPECT Shielding Structure

The inner detector, that includes <sup>6</sup>LiLS, supporting structure and calibration system is enclosed by a system of layers of shielding, tightly and nearly hermetic nested one into another. The first layer is the acrylic tank. The thickness of tank walls is 0.063 m, and its purpose is to house the optical and support systems and PMTs. The acrylic material was chosen for compatibility with the materials inside. The next layer is a mix of borated polyethylene (BPE) and deionized water with the thickness from 0.025 m to 0.075 m<sup>11</sup>. The reason for this layer is to increase the attenuation of thermal neutrons<sup>71</sup>. Inner detector, acrylic tank and BPE/water layers are enclosed by a secondary welded aluminum tank. The purpose of this tank is to prevent possible leakages of <sup>6</sup>LiLS. With the thickness of walls of the tank of 0.025 m, it provides a rigid support to the mass of the outer shielding. The outer shielding, or passive shielding has a layer of 0.025 m lead bricks enclosing the aluminum tank. The lead layer is tightly fitting the side walls and the bottom of the detector, but a layer of 0.127 m of BPE<sup>71</sup> is placed between the aluminum tank and a lead at the top of the detector. The lead layer is surrounded by a 0.10 m of high-density polyethylene lumber (HDPE) structure<sup>11</sup>. The plastic lumber layer at the top of the detector is thicker and is traversed by steel pipes for better support of the detector structure. The next layer of outside shielding is another layer of 0.025 m BPE. The reason for this BPE layer is to provide attenuation of 2.2 MeV gamma-rays that were produced by thermal neutron captures in the HDPE level<sup>11</sup>. Finally, the overall enclosing layer is aluminum sheets. The reason behind this additional shielding is fire safety at HFIR. As it can be seen in Figure. 3.1, the upper shielding is thicker in order to provide shielding from cosmic rays. Another layer of polyethylene WaterBricks filled with tap water is placed at the top of the

detector. Fiberglass fire blanket covered WaterBricks layer to provide fire safety.

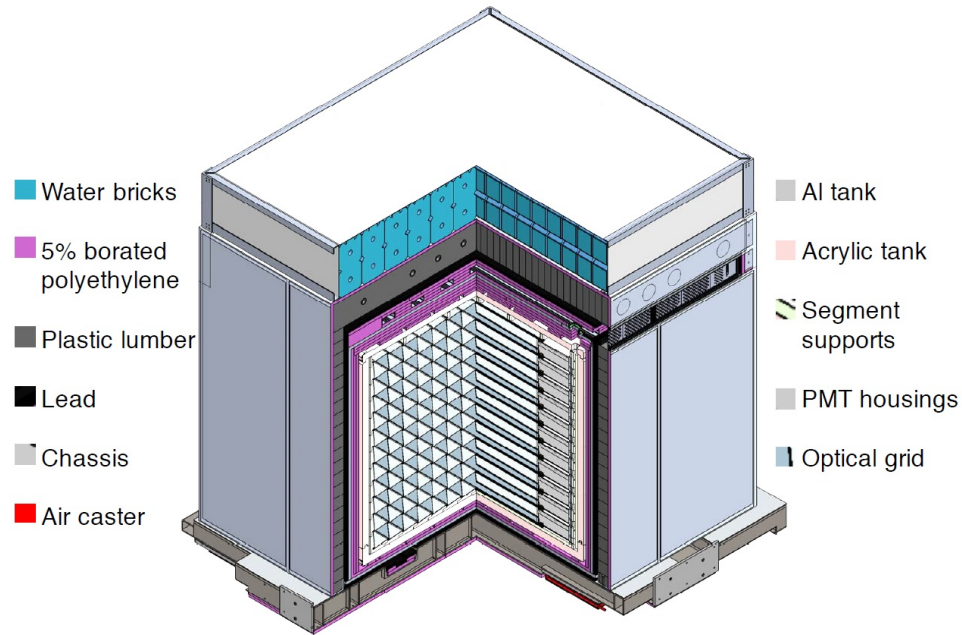


**Figure 3.1:** The 3D design of detector shielding layers. The inner detector, separated in array of 11 x 14 segments is surrounded by acrylic tank, shown in rose color. Acrylic segment supports (light green), optical grid and PMT housings (beige) are indicated in the picture. The essential layers of the shielding include 5% borated polyethylene (purple), secondary aluminum tank (light gray)<sup>11</sup>

The shielding underneath detector includes BPE sheets of thickness of 0.025 m in order to suppress thermal neutrons background from the experiments, conducted by other research groups below the PROSPECT experiment room. BPE sheets are installed to the structure of chassis (Fig. 3.2) from below. A 0.025 m layer of lead is installed on top of the structure of chassis. Chassis itself is a rectangular welded steel frame. The chassis serves multiple purposes at once, which include enabling mounting of the detector, enabling motion of the detector to the three different baselines, distribution the weight of the detector to meet the weight requirements, and allowing tilting of the detector while filling it with liquid scintillator<sup>11</sup>.

The layered shielding design is not the only shielding that was used in the PROSPECT experiment. As shown in Fig. 3.3 (right), a one-meter-thick concrete wall separates a reactor pool from the Experiment Room, where detector is located. However, this concrete wall is penetrated by un-

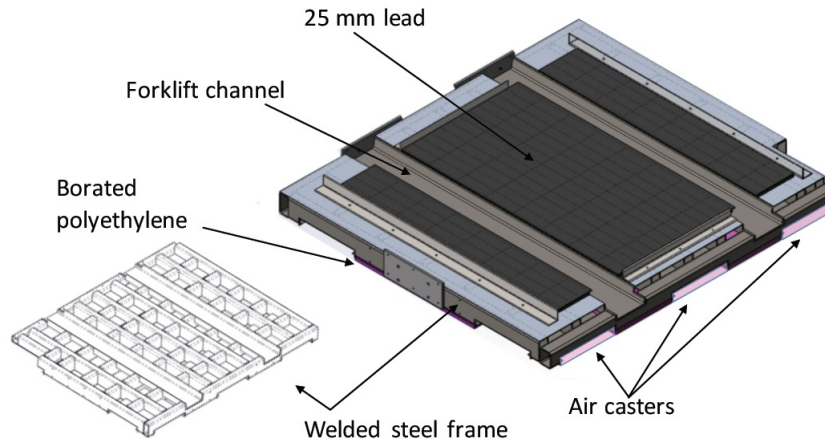


**Figure 3.2:** Detector bottom part of the shielding and the support chassis<sup>11</sup>.

used beam lines and pipes to the reactor water pool. Studies with NaI(Tl) scintillator detectors<sup>72</sup> indicated that these beam lines and pipes serve as additional hot spots with higher reactor related gamma-background. The largest source of the background is the EF-4 beam line in front of the detector. In order to eliminate this background, a fixed lead wall had to be mounted in front of the wall. This fixed wall did not have to satisfy weight limitations, and therefore was allowed to be sufficiently more thick, than passive shielding of the detector. The thickness of the wall is 0.10 m in the center, and 0.05 m at the right and left sections. Extra mini-wall of 0.10 thickness of lead was added in front of the location of EF-4 beam line for extra protection from that hot spot (Fig. 3.3, right)<sup>11</sup>. The design of the wall steel supports allow it to withstand seismic activities. The photograph of the local shield wall is shown in Fig. 3.4

A thick, solid, polygonal shaped, concrete monolith supports the reactor pool on the bottom. PROSPECT detector partially rests on this concrete monolith, as shown in Fig. 3.3 (right). This monolith creates a good suppression of the background caused by the experiments downstairs. However, as shown in Fig. 3.3, part of the detector is supported by a thinner steel reinforced concrete floor of thickness of 0.15 m. The uneven shielding underneath detector will result in the local hot spot above thinner part of the floor - on the south side of the detector opposite to reactor. This hot spot manifests itself during reactor-on periods in form of higher flux of gamma-rays from the beam

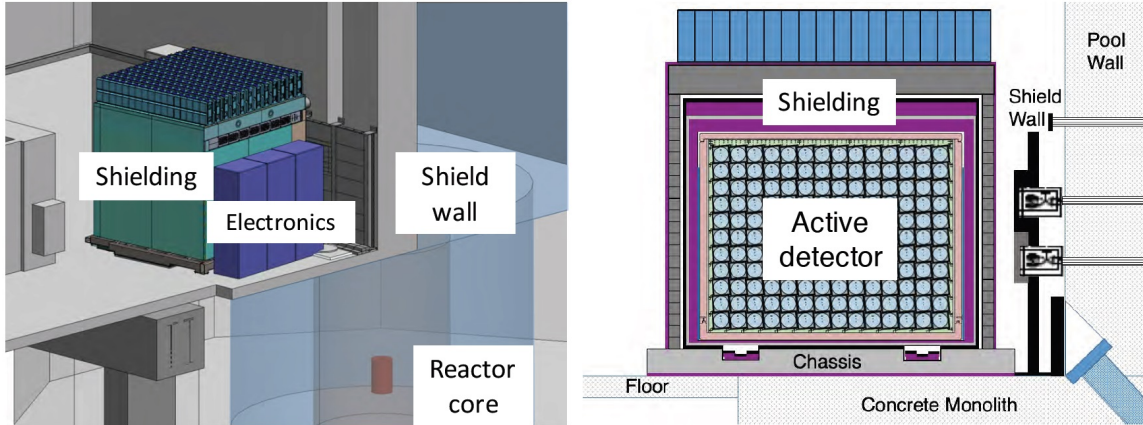


**Figure 3.3:** (left) 3D layout of detector, Experiment Room, shield wall, reactor and the water pool. (right) 2D disposition of PROSPECT detector. The scheme shows shield wall that covers the holes in the pool wall to provide shielding from this source of high reactor background. The picture also shows the disposition of the detector on concrete monolith under the floor.<sup>11</sup>

line products due to experiments below the Experiment Room<sup>71</sup>.

### 3.1.3 Shielding from Cosmogenic Background

Another type of background other than reactor related, is cosmogenic background. PROSPECT is a ground experiment with minimal overburden. Therefore, the cosmogenic background is much higher than for the experiments located underground.

The cosmogenic neutrons background come from the cosmic rays or secondary rays either interacting in the atmosphere, or in the surrounding structures in the roof of Experiment Room. They can also be born through a spallation within a detector. The roof of the HFIR building is made of 0.2-m-thick steel reinforced concrete, which does not attenuate those cosmic particles effectively. The cosmogenic neutrons can have the whole range of different energies from thermal to fast and can mimic IBDs in an accidental or correlated way. Correlated neutron event can happen when fast neutron interacts with scintillator resulting in inelastic proton recoil, following with a neutron capture on  ${}^6\text{Li}$ . When muon interacts with scintillator and produces shower, or due to shower of neutron spallation, multiple neutrons can be result of these showers, and therefore mimicking IBD even in different ways. For example, when one neutron is captured on  ${}^1\text{H}$  and another is captured on  ${}^6\text{Li}$ , or when a fast neutrons is scattered inelastically on  ${}^{12}\text{C}$  with the following capture on  ${}^6\text{Li}$ <sup>71</sup>.

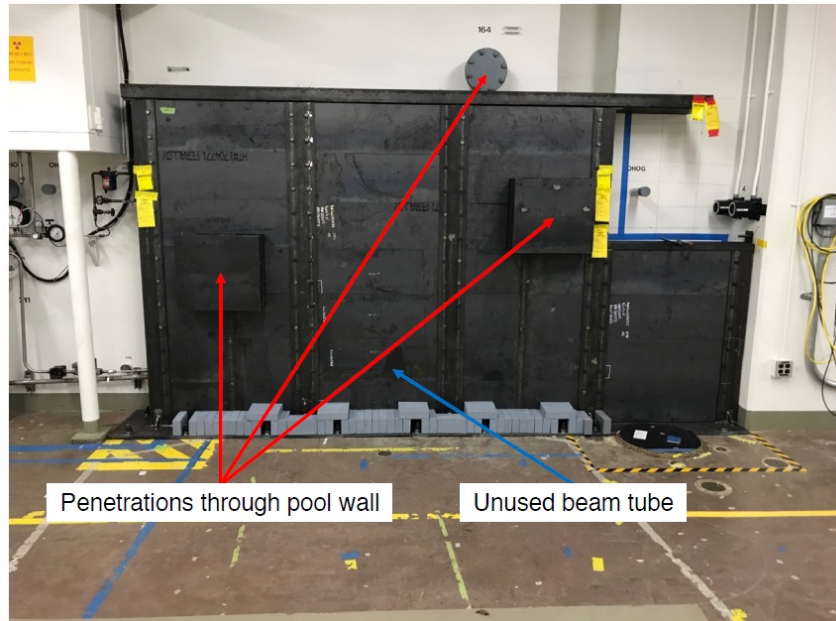


**Figure 3.4:** A photograph of the lead wall. The red arrows indicate the pipes penetrating to the reactor water pool. A blue arrow indicates EF-4 beam line that is directed toward the reactor vessel. The central part of the wall is 2.1 m tall and 3.0 m wide.<sup>11</sup>

In addition, different neutrons coming from the same cosmogenic shower can simply be captured at different times accidentally passing the IBD time, energy, and topology cuts, therefore also mimicking the signal. Considering the high rate of muons in a ground detector, and also a present hadronic component, the shower veto system is necessary to implement in as one of the the active background rejection methods.

Fig. 3.5 shows the simulation of the cosmogenic background rates that pass all IBD cuts with all the shielding discussed above. The outer segments exhibit rates of cosmogenic mimicking events 10-100 higher than in inner segments due to loss of the information about back neutron scattering near the edge of the detector. Therefore, the fiducial cut that required prompt and delayed signals lay in the innermost segments is another effective active technique to reduce cosmogenic background. For PROSPECT analysis, fiducial cuts not only includes taking the outer segments out, but also taking out the ends close to PMTs of each segments, leaving only middle part of each element.

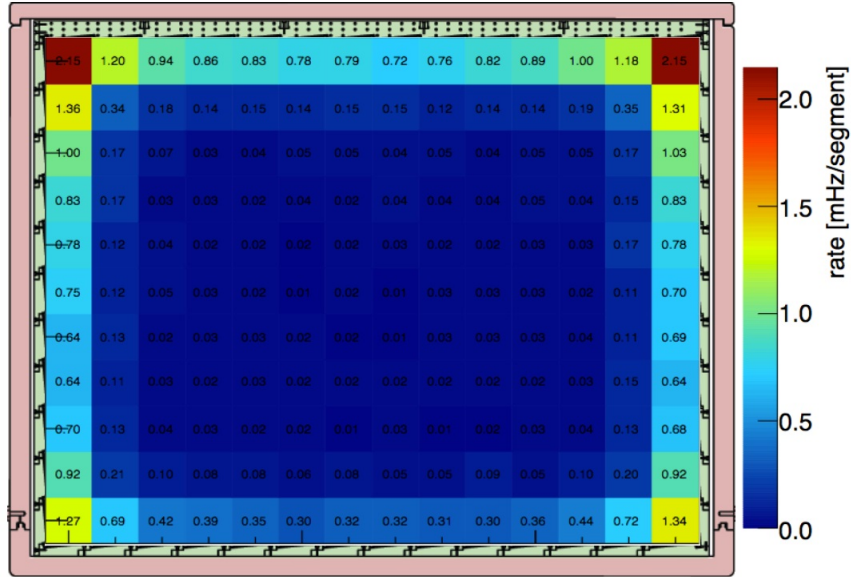


**Figure 3.5:** A simulation of the cosmogenic neutrons interactions that pass IBD topology cuts and segment-end fiducialization.<sup>11</sup>

### 3.2 Primary Cosmic Rays

Every surface and underground experiment in particle physics has to deal with cosmic rays as a inevitable background they produce. In fact, even the field of particle physics started in its early years in 1930s could study energetic particles only through the cosmic rays<sup>73</sup>. Cosmic rays are beams of high energy particles that consist of ionized nuclei, of which 90% are protons (ionized hydrogen atoms), 9% are alpha-particles (ionized helium atoms), and the other 1% are heavier nuclei. The majority of cosmic rays are relativistic, and the rate with which they hit our Earth's atmosphere reaches about 1000 per square meter per second.

The vast majority of cosmic rays arrive on Earth from outside of our Solar System but from within our Galaxy. When the Sun is more active, the solar wind it emits - magnetized plasma - actively deflects cosmic rays from reaching Solar System. In contrast, when the Sun is "quiet", more cosmic rays have a chance to reach the Earth. Small portion of cosmic rays that reach Earth come from the Sun itself as a result of violent events such as solar flares. The cosmic rays that have the highest energies can come from outside of our Galaxy<sup>73</sup>.

### 3.2.1 Solar Modulation of Galactic Cosmic Rays

The emission of the Sun of a stream of ionized plasma is called a solar wind. The solar wind mostly consists of electrons, protons, alpha particles and traces of heavier ions and atomic nuclei. Solar wind travels with a velocity of about 500 km/s<sup>73</sup>. Since the emission radiates outward from the Sun, the Galactic cosmic rays have to travel upstream of the wind to reach the Earth. They lose their energy during the process that is called solar modulation, and the lowest energy cosmic rays are fully deflected and do not reach our atmosphere at all. The solar modulation depends on the 11-years cycle of solar magnetic activity.

Solar activity is often measured in terms of sunspot numbers. Sunspots are darker areas on the surface of the Sun that are caused by different, cooler temperatures in the region of the sunspot (3000 - 4500 K) comparing to surrounding regions (typically, 5780 K). The Sun's surface is made of charge gases that are constantly moving, and this motion of charge generates magnetic fields. In the areas where magnetic fields are particularly strong, they trap the hot gas underneath therefore keeping some of the heat from reaching the surface. This causes appearance of cooler areas which are sunspots<sup>74</sup>. The Sun's magnetic field goes through 11-years cycle with complete flip of the poles, which follows with the solar minimum - or the least number of sunspots during the solar minimum. The maximum of solar activity, or solar maximum, happens in the middle of 11-years cycle with the maximum number of sunspots. Then, the solar activity goes down with the number of observed sunspots until the new cycle begins. The example of last six solar cycles through the sunspot numbers is shown in Fig. 3.6. We can note, that 2018 when the PROSPECT experiment took place somewhere close to the minimum of 24th solar cycle. This is how the website SpaceWeatherLive.com described solar activity on April 17, 2018:

*"Solar activity has been pretty boring lately with no solar flares or sunspot regions really worth mentioning. A tiny region with a reverse magnetic polarity did appear a few days ago which likely belonged to the next solar cycle but it faded away pretty quickly. It is normal for sunspot regions from two solar cycles to overlap around solar minimum but it does show we are closing in on true solar minimum. This combined with the fact that we are hardly seeing any sunspots or flaring activity at*

*the moment means this solar cycle might be a shorter than average cycle.”<sup>75</sup>*

The solar activity modulation deflects part of the cosmic rays with energies below about 10 GeV from reaching Earth’s atmosphere, and comparison of solar activity with rates of a neutron detector on Earth is shown in Fig. 3.7. This means that PROSPECT detected higher number of cosmogenic rays comparing how much it would detect during solar maximum.

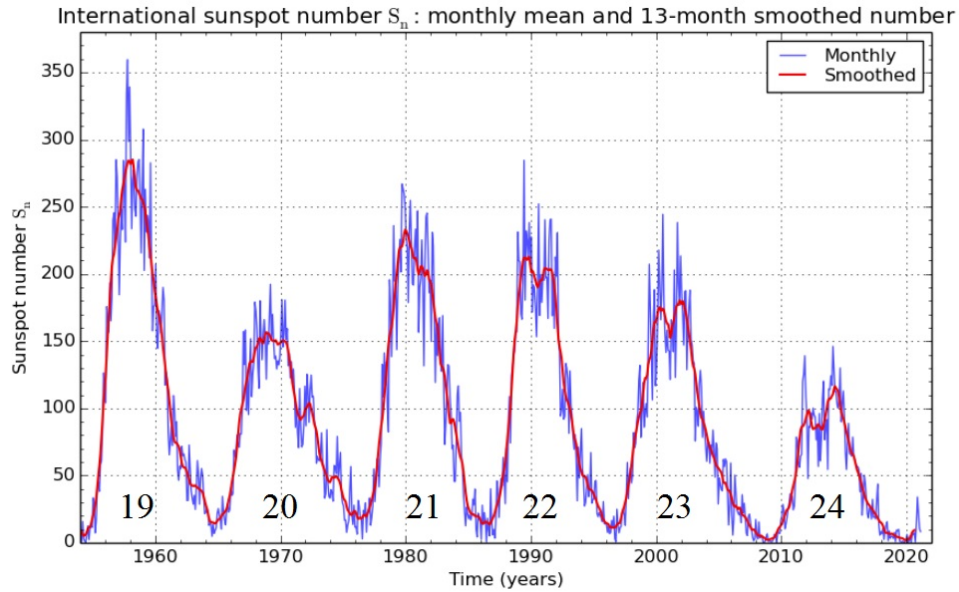


**Figure 3.6:** Plots of the monthly sunspot number (blue) and smoothed sunspot number (red) for the solar cycles 19-24<sup>12</sup>.

### 3.2.2 Solar Events and Solar Cosmic Rays

The solar activity is accompanied with violent solar events such as solar flares and coronal mass ejections. Solar flare is a sudden emanation of high energy electromagnetic radiation from the surface of the Sun. It usually happens near the sunspot group. Solar flare can be seen as just a flash of brightness or often follow by a coronal mass ejection (CME) - a powerful release of radiation and plasma into the space. The Sun generates about 3 CMEs each day during solar maxima, and about 1 CME every 5 days during solar minima. CME can reach the speed of up to 2000 km/s<sup>76</sup>. Solar flares are caused by reorganizing of magnetic field lines near the sunspot regions.

During solar flare or CME, a large magnetic disturbance happens in the direction toward Earth.

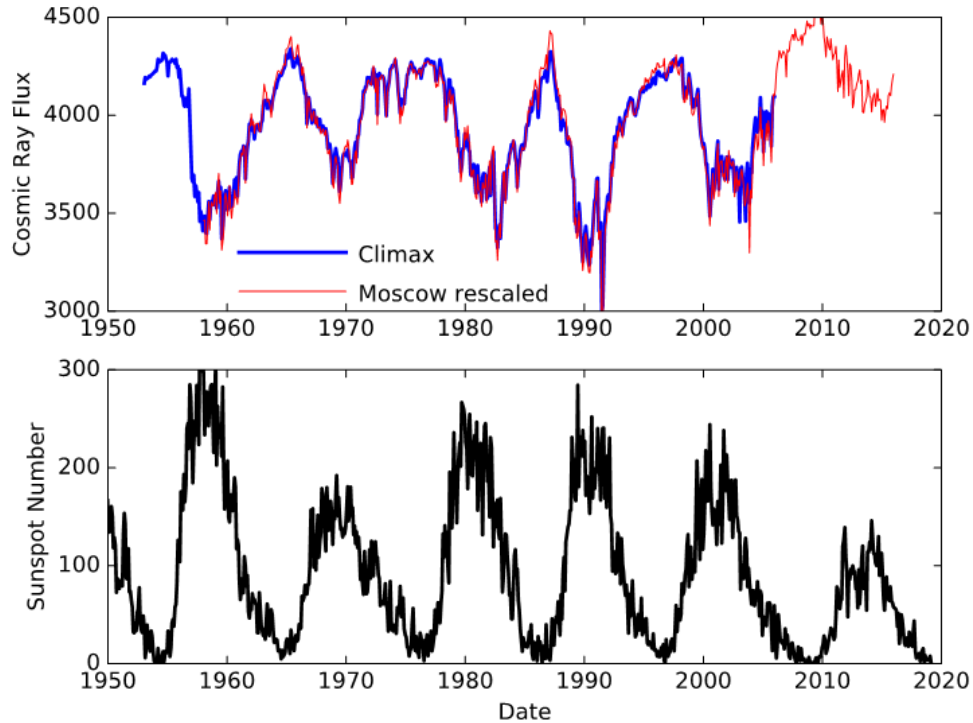


**Figure 3.7:** Solar modulation of cosmic rays. The upper plots show rates of cosmic rays from Climax neutron monitor (blue), and from Moscow, Russia that is rescaled and plotted in red. The lower plots shows monthly sunspot numbers<sup>13</sup>.

When such disturbance arrives at Earth, it sweeps away part of the Galactic cosmic rays, therefore causing the rapid decrease in their detected rates on the ground. Such decreases are called Forbush decreases. Forbush decreases usually happen within few hours, and the initial rate of galactic cosmic rates restore within few following days. Rarely, solar energetic particles from coronal mass ejection can penetrate Earth’s atmosphere, reach the ground and be detected by ground-based neutron monitors. Such even is called Ground Level Enhancement/Event (GLE). For this to happen, the amount of particles must be significant, and they have to have high energies. Whether GLE is happened or not, also depends on where on Sun the flare occurs whether magnetic field structure of the Sun accelerates those particles toward Earth.

However, GLE are rare events. There have been only 72 GLE detected by neutron monitors since 1942<sup>77</sup>, in which the last one, number 72, was detected on September 10, 2017. Therefore, there were none GLE happening during the PROSPECT experiments.

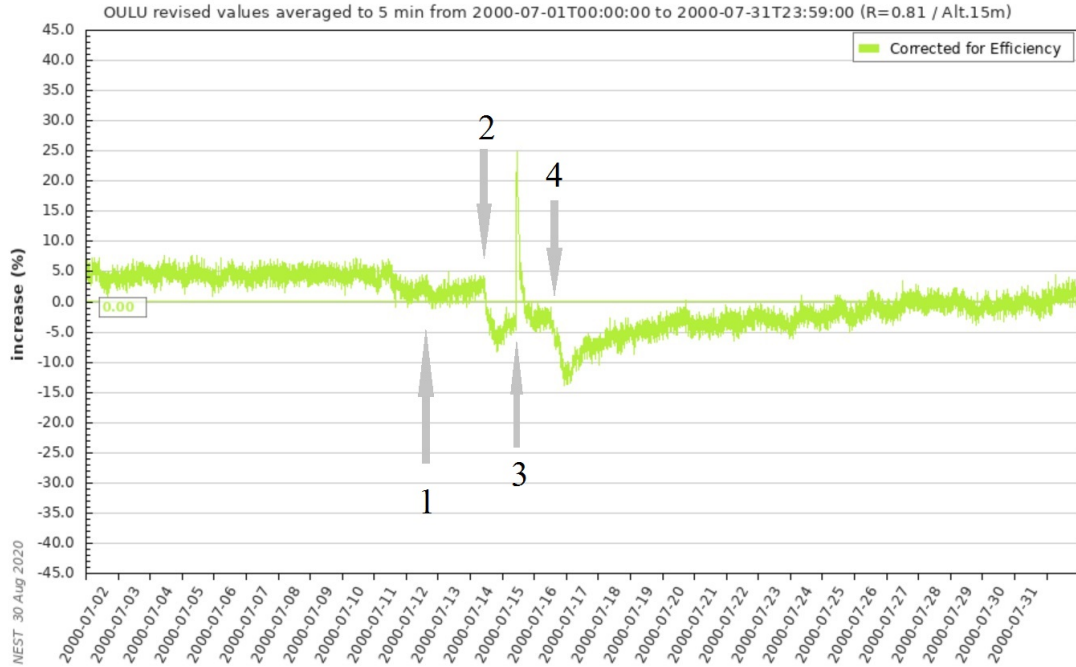


**Figure 3.8:** A record of Oulu neutron monitor during GLE in July 14, 2000. As shown in the picture, first CME (1) at the Sun happens on July 11th. It arrives on Earth on July 13 (2), and the Forbush decrease in rates of cosmic rays is observed. On July 14, a second powerful CME happens on the Sun, which accelerates high energy solar particles that reach Earth within minutes. This sudden increase in cosmic rays of solar origin is observed as GLE (3). Finally, second CME arrives on Earth on July 15 (4) and sweep away galactic cosmic rays. Another Forbush decrease is detected by Oulu neutron monitor. Second CME also produces the largest geomagnetic storm on Earth in 10 years. The plot is obtained from Neutron Monitor Database NEST<sup>14</sup>.

### 3.2.3 Geomagnetic Field Effect on Cosmic Rays

Another aspect that affects the detection rate of cosmic rays is the Earth's geomagnetic field. It deflects low energy cosmic rays thus suppressing the chance of them to penetrate the Earth's magnetosphere and reach the ground. Depending on the location on the globe, the threshold (cut-off) rigidity for cosmic rays arriving at a zenith angle  $\theta$  and azimuth angle  $\phi$  can be defined. The primary cosmic rays with the lower rigidity get deflected by the geomagnetic field and do not enter the Earth's atmosphere<sup>16</sup>. The geomagnetic field suppresses the cosmic rays near the equator much more than near the poles by the means the magnetic field lines are distributed. Therefore, the cut-off rigidity can be less than 1 GV near the geomagnetic poles, and up to 16 GV for vertical particles around the equator<sup>16</sup>.

Another geomagnetic effect that is correlated with cosmic rays is geomagnetic activity. Though geomagnetic activity is not the source of deflection of cosmic rays, the geomagnetic activity (including storms) tracks Sun's activity, and therefore the correlation exists.

### 3.3 Secondary Cosmic Rays

Primary cosmic rays while being in atmosphere, collide with atoms and molecules, which primarily are oxygen and nitrogen. During this interactions, cascades of lighter particles are produced in form of air showers (Fig. 3.9). Typical secondary cosmic rays are gamma-rays, protons, alpha-particles, pions and kaons, muons, electrons and positrons, neutrinos and neutrons. Except for protons and electrons that are produced at the top of atmosphere, all other particles are generated during interactions of primary cosmic rays with the air (Fig. 3.10).

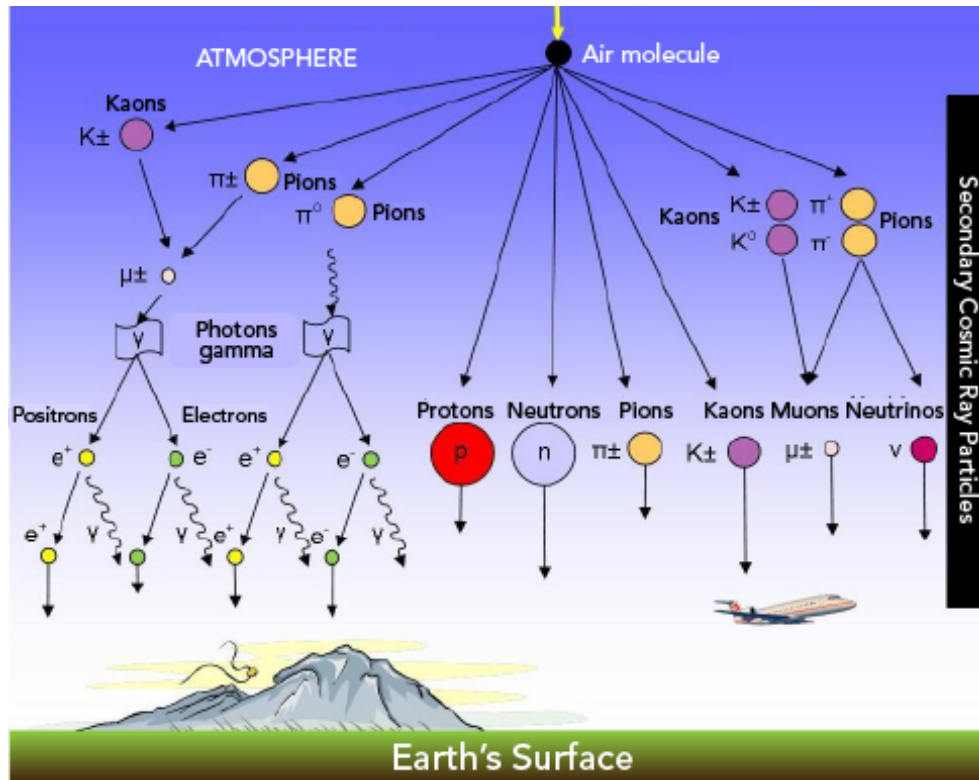
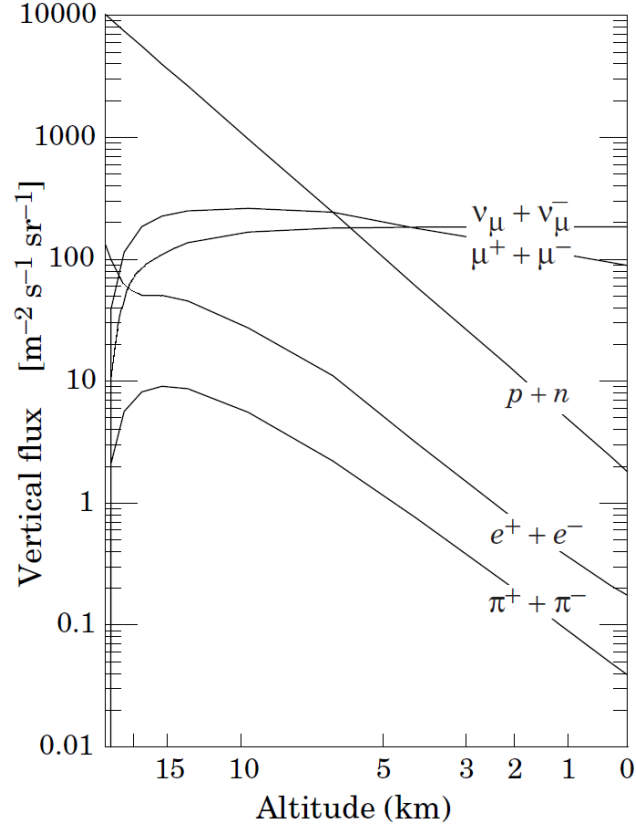


Figure 3.9: Production of cosmic ray showers in the atmosphere<sup>15</sup>.



**Figure 3.10:** The estimations of vertical fluxes of cosmic rays with energies above 1 GeV in the atmosphere as a function of altitude. The energy regions used were the regions in which the particles are the most present, except for electrons<sup>16</sup>.

### 3.3.1 Mesonic Component: Pions and Kaons

The interactions of primary cosmic rays produce three kinds of pions ( $\pi^+$ ,  $\pi^-$ , and  $\pi^0$ ) and two kinds of kaons ( $K^+$  and  $K^-$ ). Both pions and kaons are mesons with very short life times:  $\pi^{+/-}$  life time  $\approx 26$  ns,  $K^{+/-}$  life time  $\approx 12$  ns, and  $\pi^0$  lifetime  $\approx 10^{-6}$  s. Thus, they either interact with the nucleons of the matter and get absorbed in the atmosphere, or decay before reaching the ground.  $\pi^0$  almost immediately decays into two photons. The decays of pions and kaons lead to creation of muons and neutrinos:

$$\pi^- \rightarrow \mu^- + \bar{\nu}_\mu, \quad \pi^+ \rightarrow \mu^+ + \nu_\mu \quad (3.1)$$

$$K^- \rightarrow \mu^- + \bar{\nu}_\mu, \quad K^+ \rightarrow \mu^+ + \nu_\mu \quad (3.2)$$

A fraction of charged pions also decay to electrons, thus producing electron neutrinos and antineutrinos:

$$\pi^- \rightarrow e^- + \bar{\nu}_e, \quad \pi^+ \rightarrow e^+ + \nu_e. \quad (3.3)$$

The neutral pions decay into gamma rays.

### 3.3.2 Mesonic Component: Muons and Neutrinos

The mean life time of muons is three orders of magnitude higher than that of the charged mesons, and is  $2.2 \mu\text{s}$ . With such a lifetime and small cross-section, muons are the few cosmic ray particles that penetrate the Earth and even reach underground. Muons are often used as a source to calibrate cosmic ray detectors.

High-energy muon neutrinos and antineutrinos are produced in pair with muons in the process of meson decay. Electron neutrinos are also produced as a result of muon decay, primarily at low energy.

$$\mu^- \rightarrow e^- + \bar{\nu}_e + \nu_\mu, \quad \mu^+ \rightarrow e^+ + \nu_e + \bar{\nu}_\mu \quad (3.4)$$

Similar chains are held for kaon channel.

The typical production altitude of muons is about 15 km. In the Earth's atmosphere, the muon decay length exceeds 15 km for energies of muon higher than about 2.5 GeV. Therefore, depending on the energy of the muons, the ratio of electron neutrino to muon neutrino rapidly decreases over 1 GeV<sup>73</sup>.

### 3.3.3 Electromagnetic Component: Electrons, Positrons and Photons

About 1% of primary galactic cosmic rays consists of high energy electrons. However, at the sea level, the electromagnetic component mostly consists of electrons, positrons, and photons as a result

of decays of neutral and charged mesons. A neutral pion decays into two gamma-rays, which may in turn create electron-positron pairs when gamma-rays encounter air nuclei. Charged pions decay into electron-positron and muon-antimuon pairs. Those pairs can also generate more gamma radiation with Bremsstrahlung ("breaking radiation") process. In this process, charged particles passing near air nuclei produce more gamma-rays. The dominant source of low-energy electrons is a muon decay described in Section 3.3.2.

### 3.3.4 Hadronic Component: Protons and Neutrons

The next abundant particles at the sea level after muons are neutrons. Neutrons are produced when primary and secondary cosmic rays interact with the atmosphere, particularly - nitrogen and oxygen nuclei. Due to their zero electrical charge, neutrons do not lose their energy with the interactions with electrons in the atmosphere. The amount of protons and electrons produced in the upper-atmosphere is the same, but protons while traveling downward, lose their energy due to interactions with electrons and disappear faster than neutrons. Neutrons, on the other hand, undergo elastic collisions with nuclei. At the energies below 10 MeV neutrons continuously lose their energy due to elastic collisions, and later are captured by nucleons. At the sea level, about one third of all nucleons coming from the vertical direction, are neutrons<sup>16</sup>.

### 3.3.5 Air Showers

While undergoing cascade events in the shower, the primary and secondary particles quickly lose their energy through each interaction. At some point, the number of stopped particles increases and exceeds the number of created particles - so-called "shower maximum". With the gradual decline, only few particles arrive to a sea level. For them to arrive, the primary cosmic ray particle must have an energy of at least 500 MeV per nucleon in the top layers of the atmosphere. Only with this energy per nucleon it can generate a cascade of particles that would reach the ground. On the Earth's surface, the amount and proportion of arrived particles mainly depend on the energy and type of the initial cosmic ray, as well as ground altitude.

As was discussed in the previous sections, the average composition of secondary cosmic ray

particles consists mostly of muons where with per 10,000 of muons, there are about 200 primary particles (protons and rare neutrons), about 20 high-energy electrons with energy about 1 GeV, and 4 pions. In addition, there may be high abundance (up to 100,000) of low-energy electrons coming from cascades<sup>78</sup>.

### 3.4 Dependence of Secondary Cosmic Rays on Atmospheric Parameters

#### 3.4.1 Dependence on Atmospheric Pressure

The thickness of atmosphere is one of the main parameters that affect the rate of observed secondary cosmic rays on the ground. The pressure, or barometric, effect on intensity of cosmic rays includes changes of absorption, decay and generation of them in the atmosphere. For example, the higher the atmospheric pressure, the higher the probability for a particle to be absorbed in thicker atmosphere before being detected on the ground. In addition, the pressure dependence also affects muon generation and decay in the atmosphere. Thus, atmospheric pressure effect leads to the time-varied anti-correlation of detected rates with the atmospheric pressure fluctuations.

With approximation of constant incoming cosmic rays flux, this dependence has the form<sup>79</sup>:

$$dN = -\beta N dP, \quad (3.5)$$

where  $dN$  is the change in measured intensity  $N$ ,  $\beta$  is barometric coefficient, and  $dP$  is difference in atmospheric pressure. From this law we can obtain equation for the atmospheric pressure adjustment:

$$N_{adjusted} = N_{initial} e^{\beta(P_0 - P)}, \quad (3.6)$$

where  $P_0$  is a reference pressure. This is the law neutron monitor detectors use to scale their rates with pressure<sup>80</sup>. The classic studies for fast neutrons rate barometric coefficients report -0.72/-0.73 %/mb<sup>81;82</sup>. On the other hand, some of the newer studies show -0.67 %/mb<sup>83</sup> and -0.57 %/mb for the newer model in recent study<sup>84</sup>.

### 3.4.2 Dependence on Temperature

The temperature effect is the most prominent in muons rate observed at the sea level. There are two mechanisms competing with each other, in which temperature of the atmosphere affects the count rate of muons on the surface. Positive effect shows increase of rate with increasing temperature. Negative effect, in contrast, shows decrease of rate with increase of temperature.

Negative effect happens because with the expansion of the atmosphere in the summer, the majority of muons are generated at higher altitude and therefore they need to travel along the longer path to reach the ground. During this travel, part of muons with lower energies has a higher chance of decay into other particles, and the rate at the ground will be lower. Positive effect happens because at higher temperatures in the summer the atmosphere is less thick, and the parent pions in the upper layers of atmosphere have a higher chance to decay before being absorbed. In winter, when the atmosphere is more thick, the pions more often interact with air molecules, therefore generating less muons during decays.

The competition between positive and negative effects of temperature on the observed rates lead to the opposite correlations with temperature for surface and underground experiments. Lower energy muons prevail over higher energy muons in surface detectors, and the anti-correlation with the season is observed, as mentioned in<sup>21;85</sup>. On the other hand, lower energy muons do not reach underground detectors, and only high energy portion of them is detected, therefore revealing positive correlation with the season<sup>85</sup> as observed, for example, in Daya Bay experiment<sup>86</sup>. For both cases, the positive and negative correlations with the season result in the harmonic periodic behavior with maximum in winter for ground experiments, and maximum in summer for underground detectors.

In contrast to muons, the neutrons intensities almost are not affected by the temperature effect, as can be seen in neutron monitors data. It affects only small portion of neutrons that are generated in the cosmic ray shower that is coming from pion/muon components<sup>21</sup>.

## Chapter 4: Event Selection and Vetoes

As cosmic rays reach the detector, they are able to interact with PROSPECT shielding and produce showers of events through spallation. Among those shower events, neutrons can mimic delayed PROSPECT signal, so a special mechanism called "shower veto" is used to remove this signal contamination.

Three types of events are considered in PROSPECT shower veto: muon-like events, neutron-like events, and recoil-like events. The muon lifetime is  $2.2 \mu\text{s}$ , so in general muons reach the ground without decaying in the atmosphere. However, some low energy muons have a chance to decay while traveling through PROSPECT detector, producing event showers, following the initial muon-like detected event. On the other hand, if two or more neutron captures are detected too close to each other in time, they can be a result of a shower due to spallation. Finally, if a recoil of a neutron is closely followed by a neutron capture, it can be that both events are experienced by the same neutron. Shower veto helps to identify those events that are likely coming from cosmic ray showers and vetoes neutron captures that otherwise would pass cuts for delayed-like event.

Shower veto is applied to delayed-like neutron capture candidate only. The time windows of different lengths are considered around the candidate. If another event that is identified as muon-like event, neutron-like event, or recoil-like event is happening prior to or after delayed-like candidate within a specific time window, then this delayed-like candidate is vetoed and does not proceed into the IBD statistics.

Another type of veto, pileup veto, is introduced for prompt-like events. This veto takes care of multiple signals recorded by DAQ that are caused by piling up of signals in the system. If two or more events are happening within very short period of time, we veto those events.

Considering that vetoing mechanism reduces the live time of the detector because the events in specific time windows are vetoed and are not included in the statistics, a dead time is introduced.

## 4.1 Cuts for Single Background Events

This work discusses two types of events: single events and coincidence events. Single events are events that consist of only one cluster and represent the isolated event of muon-like, recoil-like, neutron capture, prompt-like, or delayed-like events. On the other hand, the coincidence events consist of two single events that have specific separation in time and distance: usually in specific order like in IBD where delayed-like event follows prompt-like event. The coincidence events we consider here are IBD events, recoil and neutron capture pairs, and neutron capture and neutron capture pairs. Shower veto is triggered by single background events including muon-like, recoil-like, and neutron capture events. The cuts with which they are selected with are presented in Table 4.1.

Muon-like events are defined only through energy of the cluster: the total energy of the cluster  $C.E_{tot}$  must be above 15 MeV. Due to the flexibility of this cut, there can be contamination at low energies with neutron recoils which can be seen as the peak at energies below 60 MeV in Fig. 4.1 b. Fig. 4.1 c shows PSD distribution of muons, while Fig. 4.1 a shows two dimensional PSD-energy distribution of muon like events for one run during reactor on. There is no observable difference in these characteristics plots between reactor on and reactor off periods.

Recoil-like events are identified through the PSD cut function. If at least one pulse in the cluster passes PSD recoil cut, the whole cluster is considered recoil-like event. The PSD recoil cut function is called *Time invariant recoil PSD cut* and is defined through the following relation: depending on which is smaller, this recoil PSD cut lies below the PSD center of recoil band by  $2\sigma$  in PSD or by the difference between PSD center of the recoil band and PSD cut above  $1.5\sigma$  of center of gamma band for the given energy. At the same time, the total energy of the cluster must not exceed 15 MeV. The PSD-energy distribution for recoil-like event is shown in Fig. 4.2 a, and Fig. 4.2 b and 4.2 c show, correspondingly, one-dimensional energy and PSD distributions obtained for one run during reactor on period.

Finally, neutron capture event is defined as a distribution of  $3\sigma$  around neutron capture energy peak (0.526 MeV) and  $1.8\sigma$  around neutron capture PSD peak. The typical picture of the "box" in PSD-energy dimension is shown in Fig. 4.3 a, and its energy and PSD one-dimensional distribution

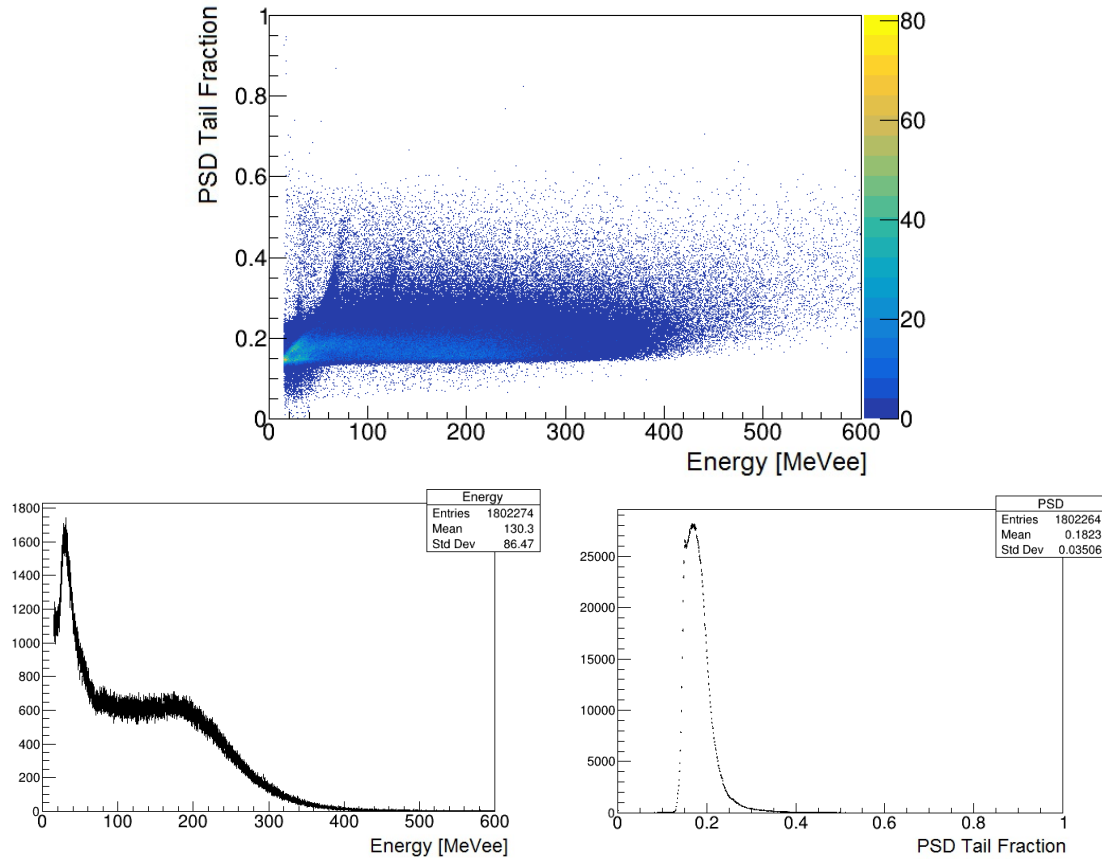


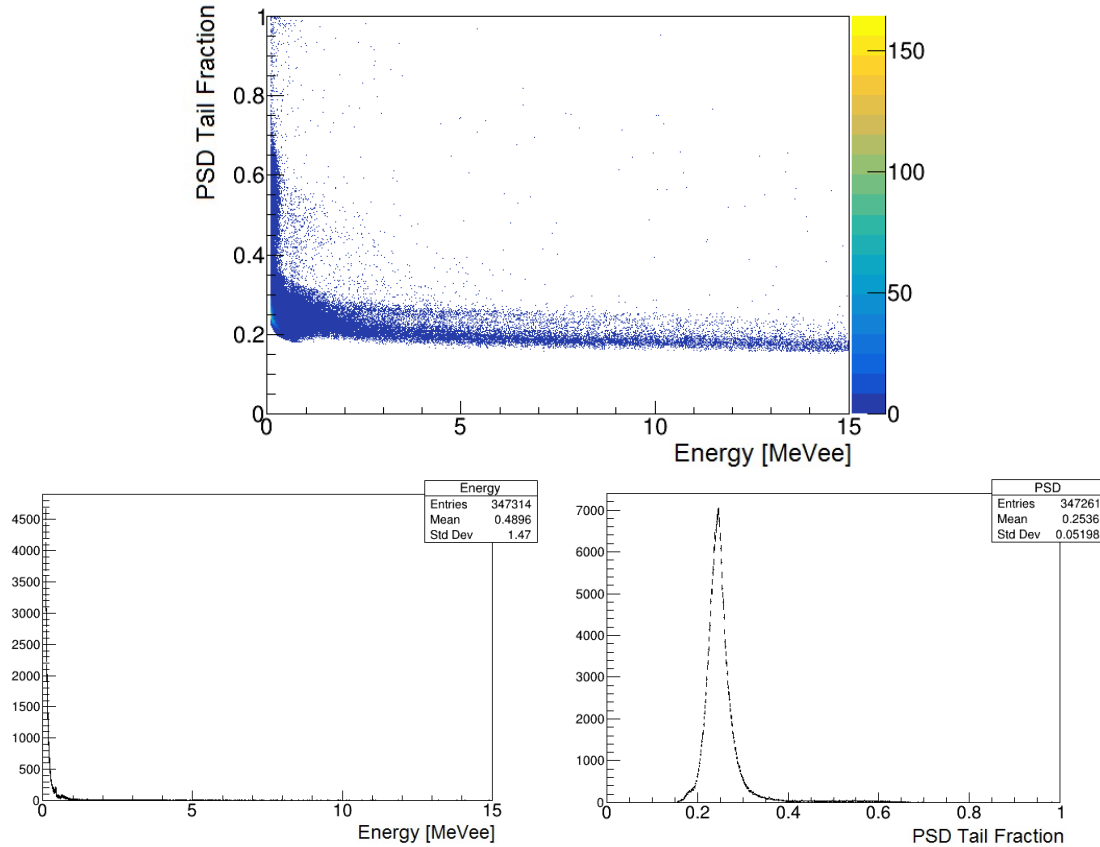
**Figure 4.1:** Illustration of cuts on muon-like events. Muon-like events are selected with energy cut only. (a) PSD vs Energy distribution for one RxOn run; (b) Energy distribution for one RxOn run; (c) PSD distribution for one RxOn run.

in, correspondingly, Fig. 4.3 and 4.3 c.

## 4.2 Rates of Single Background Events

### 4.2.1 Muon-like Single Events

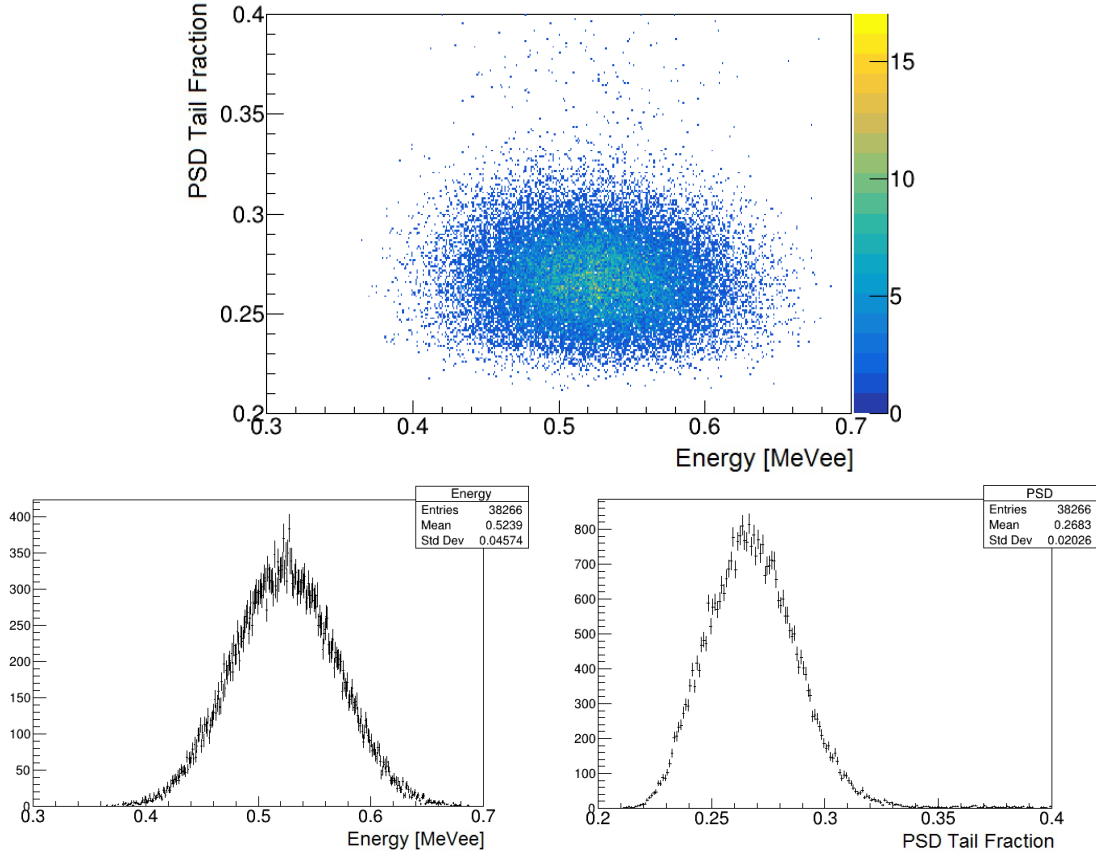
The behavior of muon-like events with time is shown in Fig. 4.4. We can see that it is highly fluctuating with the atmospheric pressure while having a decreasing trend with time. In contrast to other cosmogenic events, muons have a sinusoidal dependence on the season or the temperature distribution in the atmosphere. Scaling with atmospheric pressure and analysis of the behavior of muons with the temperature are discussed in Chapter 7.



**Figure 4.2:** Illustration of cuts on recoil-like events. The PSD and energy plots were done for the pulse, which lets the cluster to pass the selection. (a) PSD vs Energy distribution for one RxOn run; (b) Energy distribution for one RxOn run; (c) PSD distribution for one RxOn run.

#### 4.2.2 Recoil-like Single Events

The recoil-like events demonstrate very clear reactor dependent behavior, shown in Fig. 4.5. This is happening due to ingress process, discussed in Section 2.3. Since we have significantly more detected events during reactor being turned on, more multiplication in the leaked inside the housings scintillator is happening, and the rates of recoil-like events go up. At the same time, the behavior of recoil-like events during reactor-on periods follows the behavior of prompt events shown in Fig. 5.4, especially shift around 08/06, but also goes up as the time goes on. Similar trend with time is shown for rates during reactor-off, as shown in Fig. 4.6. This is happening because, as it assumed, as the time went on, the more scintillator was able to leak into the housings, and the ingress effect was raising.

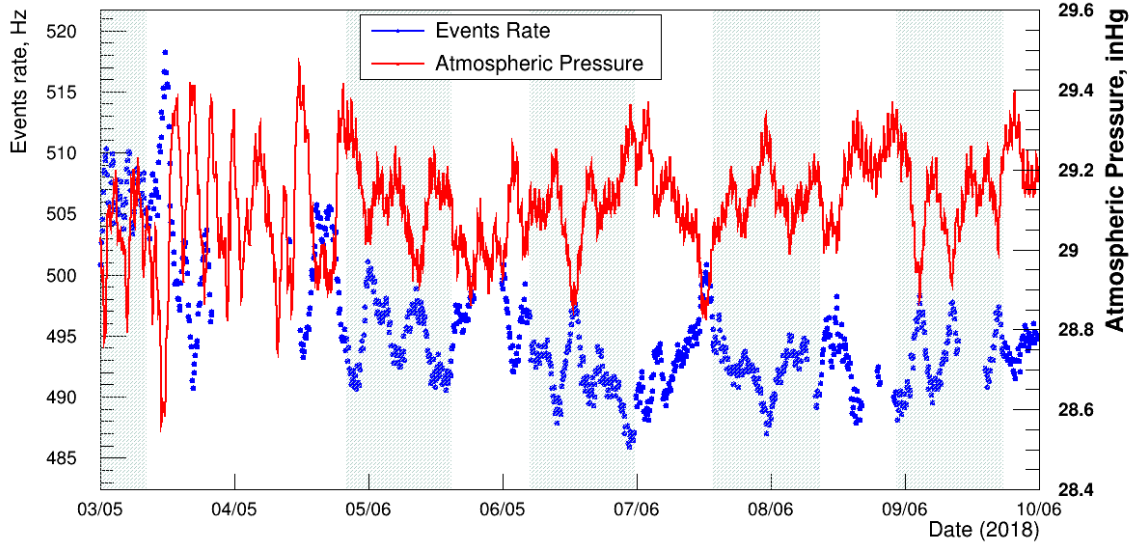


**Figure 4.3:** Illustration of cuts on neutron capture events. The energy is smeared energy. (a) PSD vs Energy distribution for one RxOn run; (b) Energy distribution for one RxOn run; (c) PSD distribution for one RxOn run.

To evaluate the behavior of the recoil-like singles, a spatial study was done for the rates of the events (discussed in the Appendix A). In this study, the detector was separated into 9 parts, and it was shown that leaking into recoil-band is happening more in the bottom of the detector, than at the top. Also, the leaking was happening more on the right side that is above hot spot than on left side that is closer to the reactor. The correlation coefficients on the pressure and their  $\chi^2$  were calculated for events from different parts. It was found, that the least leaked parts of the detector (top and left) have the higher correlation coefficient with the atmospheric pressure, and significantly lower  $\chi^2$  than events with more leaked in signals (bottom, right). This spatial distribution and dependence on the atmospheric pressure supports the ingress nature of abnormalities in the recoil-like band.

**Table 4.1:** Cuts for single background events.

	Cluster size	Energy, MeV	PSD	Other
Muon	$\geq 1$ pulse	$15 < C.E_{tot} < 1e12$		Not OCS signal
Neutron	1 pulse	C.E <sub>tot</sub> is in range of $3\sigma$ around neutron capture energy peak	PSD $> -1.8\sigma$ around neutron capture PSD peak PSD $< 0.4$	
Recoil	$\geq 1$ pulse	$C.E_{tot} \leq 15$	If at least one pulse (that is not identified by its PID as an ingress hit) with PSD $> \textit{time invariant recoil PSD cut}$	Not a neutron Not OCS signal

**Figure 4.4:** Rates of muon-like singles with time.

### 4.2.3 Neutron Capture Single Events

Neutron capture rates demonstrate both clear dependence on the atmospheric pressure, and increase of the rates during reactor-on comparing to reactor-off, as well as slow increase of rates in time (Fig. 4.7). The mechanism for this behavior is the same as for recoil-like singles, which is due to ingress. However, the neutron capture cut better filters out those extra events, comparing to recoil-like singles because false events rather leak into higher PSD values.

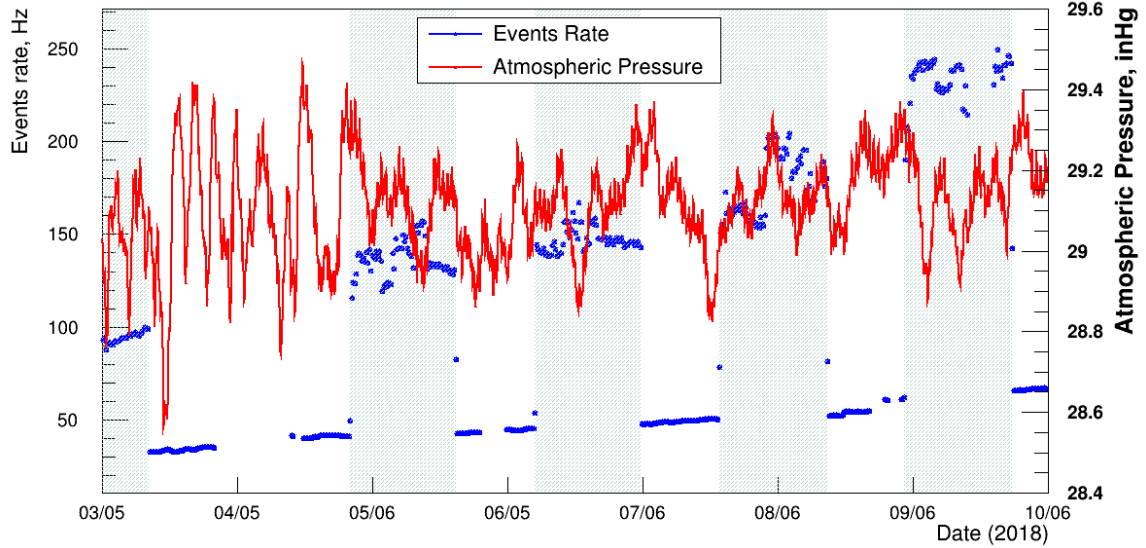


Figure 4.5: Rates of recoil-like singles with time.

#### 4.2.4 All Single Events

Finally, taking into account that the pileup veto, although not being cosmogenic, depends on the total number of events, it is interesting to see the evolution of total rate with time. Fig. 4.8 shows the total number of events during PROSPECT timeline. We can see, that the rates are highly dominated by the reactor background. Fig. 4.9 shows only reactor-off rate.

### 4.3 Veto Application

Fig. 4.10 represents scheme of how we apply the cosmic shower veto on delayed-like candidate. The following shower veto windows are introduced around potential delayed-like candidates:

- One-sided preceding muon veto from  $(-200 \mu\text{s}, 0)$
- One-sided preceding recoil veto from  $(-250 \mu\text{s}, 0)$
- Double-sided neutron veto from  $(-400 \mu\text{s}, 400 \mu\text{s})$

If any of these events (muon-like event, recoil-like event, neutron capture) is found in the corresponding time window around delayed-like candidate, the candidate is vetoed.

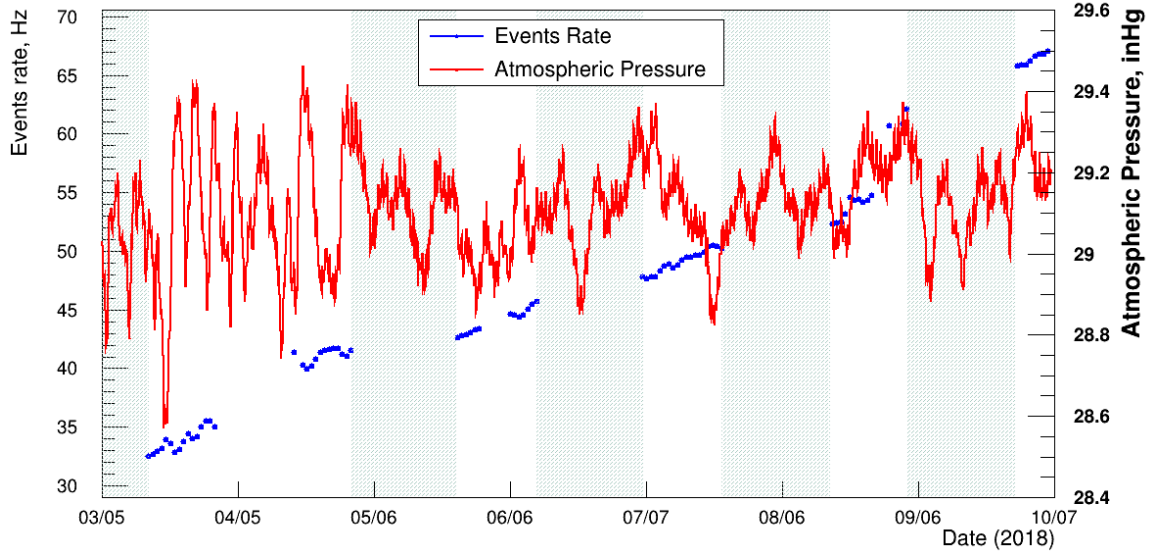


**Figure 4.6:** Rates of recoil-like singles with time for RxOff only.

The pileup veto that is applied to prompt-like candidate has similar mechanism: if any other event (cluster) is happening within 800 ns prior to prompt-like candidate, this candidate is vetoed.

Figure 4.11 demonstrates the reduction in the IBD candidates as different cuts are applied, including cosmic and pileup vetoes.

#### 4.4 Dead Time

When the veto is applied, the time window in which it is applied does not write down any information, and therefore, a detector live time must be reduced through introduction dead time due to veto mechanism.

The scheme of implementation of shower dead time is shown in Fig. 4.12. For each veto causing event, a time window around this event is considered as a dead time because any possible delayed-like candidate (for shower veto) or prompt-like candidate (for pile up veto) would be vetoed in that period. The following time windows are considered:

- After muon-like events:  $(0, 200 \mu s)$
- After recoil-like events:  $(0, 250 \mu s)$
- Around neutron capture:  $(-400 \mu s, 400 \mu s)$

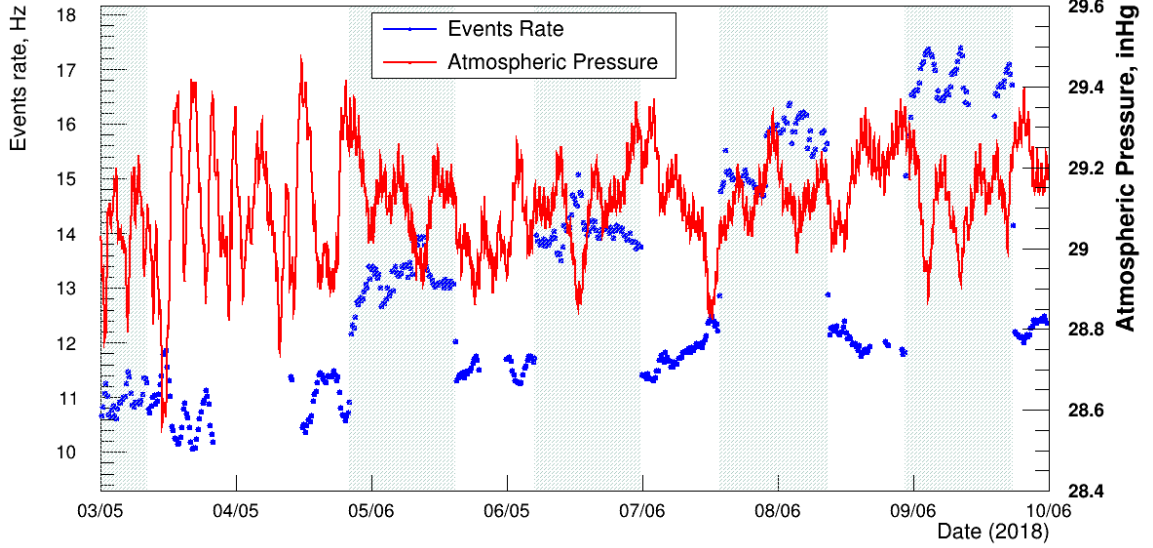


**Figure 4.7:** Rates of neutron captures with time.

Pileup veto deadtime is considered in similar way: after every cluster a window of (0, 800 ns) is a pileup deadtime.

Shower veto and pileup deadtimes are inserted into interval vectors for prompt main, prompt accidental, delayed main and delayed accidental rates. Inserting in special interval vectors allows to solve the overlapping issue with of different time intervals. A special function merges them into 4 single time intervals, and deadtime for each of 4 cases is calculated. Then, veto deadtime correction is calculated with the formula<sup>87</sup>:

$$\text{Deadtime correction coefficient} = \frac{t_{run}^2}{(t_{run} - t_{dead}^{prompt})(t_{run} - t_{dead}^{delayed})} \quad (4.1)$$

separately for main and accidental rates.

The comparison of fractional detector-wide rates of deadtime with time for all types of vetoes is shown in Fig. 4.13. Veto dead times are higher during reactor-on periods, while at the same time steadily increasing with time for neutron, recoil and all vetoes during both reactor-on and reactor-off periods. Therefore, we can see the importance of the correction for the deadtime that has to be done for our IBD analysis.

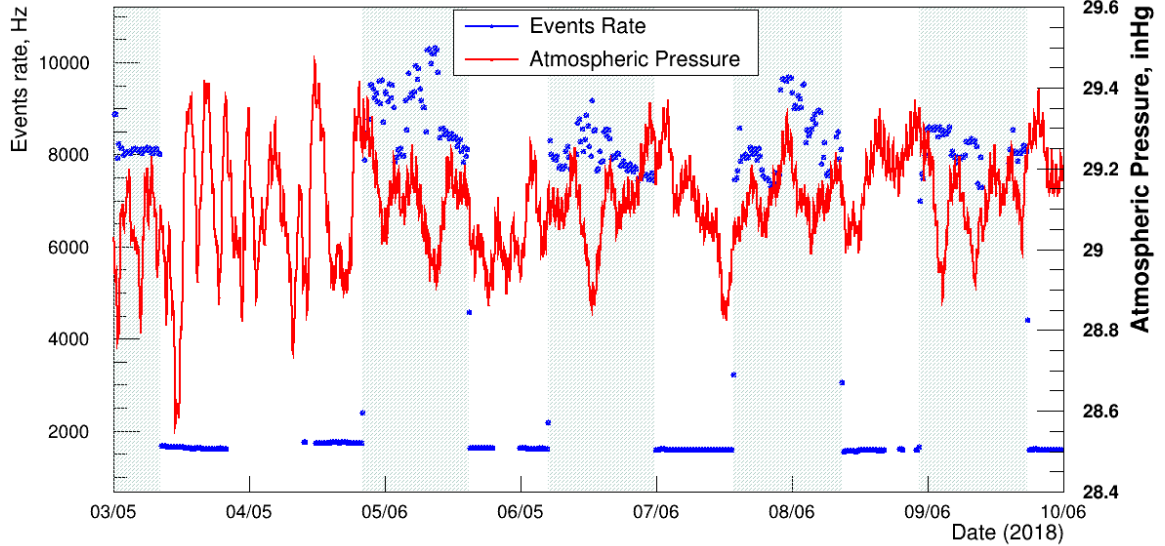


**Figure 4.8:** Rates of all single events with time.

#### 4.5 Water Pool Level Singles Study

The water level in the pool, where reactor is placed, was lowered for 3 days during RxOff period in order for researchers to get access to the core vessel to facilitate maintenance inside the reactor vessel. The nominal height of water is 3 m above the PROSPECT target volume y-center, and it was lowered to approximately 2 m below it. The dates, time of the procedure and the height were documented by the reactor operations staff of HFIR. To assess, if the change in water level affected the registered background rates during that periods, a study was performed. In this study, the rates of single events were looked as dependent on the water level height, and this dependence was estimated. If the dependence would be comparable with atmospheric pressure dependence, a corresponding scaling correction was meant to be done to perform a correct background subtraction.

As shown in Fig. 4.14, theoretically, a cosmogenic event, coming at some angles, can more freely come to the detector when the water level is lowered. At the same time, the same event, coming from the same level, would be blocked by the water, when the water level is 3 m.

The events of concern we are interested in include fast neutrons that create inelastic  $nC^*$ -scattering, or  $(n,2n)$  IBD-like events, and low energy muon-induced neutron spallation (multi-neutron captures:  $(nLi,nLi)$ ,  $(nH, nLi)$ , and  $(nH,nH)$  ).

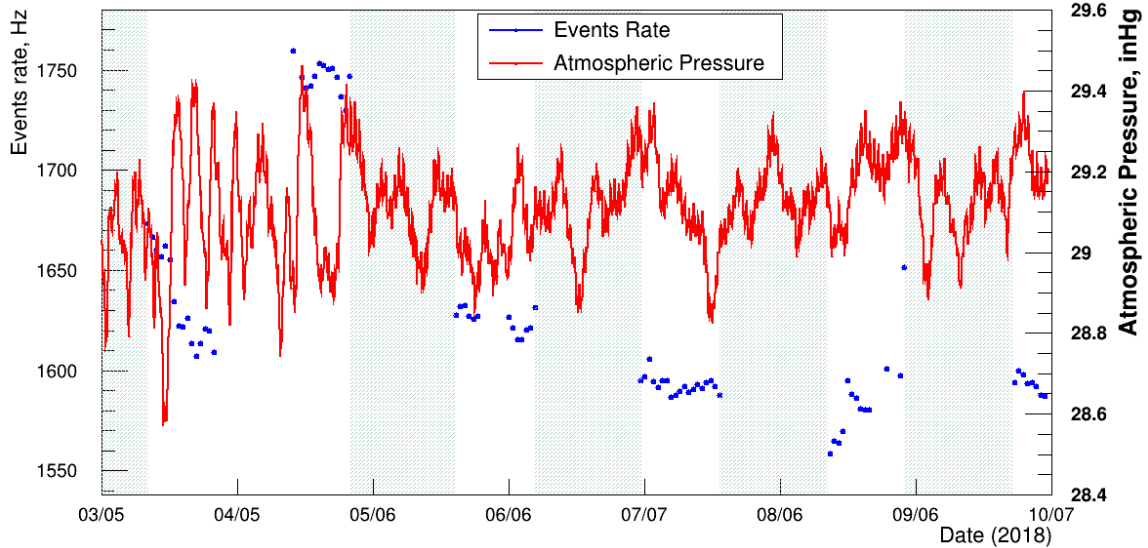


**Figure 4.9:** Rates of all single events with time for RxOff only.

In the study, the rates of the single n-Li captures and recoil-like events were compared to water levels, and the dependence was evaluated. Fig. 4.15 shows the zoomed in rate of neutron captures (top) and recoil-like singles (bottom) superimposed with water level drop, shown in red. The water level shown for this time period has the longest duration (1 day), but by eye we cannot observe the increase in the rate. The study did not show any significant correlation with water levels, and the parallel study on muons<sup>88</sup> estimated the rates of events during low pool level periods compared to the rates during nominal pool level periods to be unchanged within a conservative 2% interval.

As a conclusion for these studies, the water pool level scaling coefficient is estimated as 1.00 with 2% uncertainty and should be applied only to about 5% of reactor-off data, during which the water level was lowered. The correction for this effect then would have a negligible contribution (only 0.05%) to the total uncertainty due to correlated background atmospheric scaling effect (0.5%).

The described cosmic veto mechanism successfully cuts of portion of delayed-like neutron captures that are not born in IBD reaction, but come from the cosmic showers. The pileup veto cuts the signals that are caused by DAQ limitations, and not real events from the reactor. The next chapter discusses how the individual components of the IBD signal - prompt-like single rates and delayed-like single rates - are selected and describes their time, energy and spatial distribution as well as what

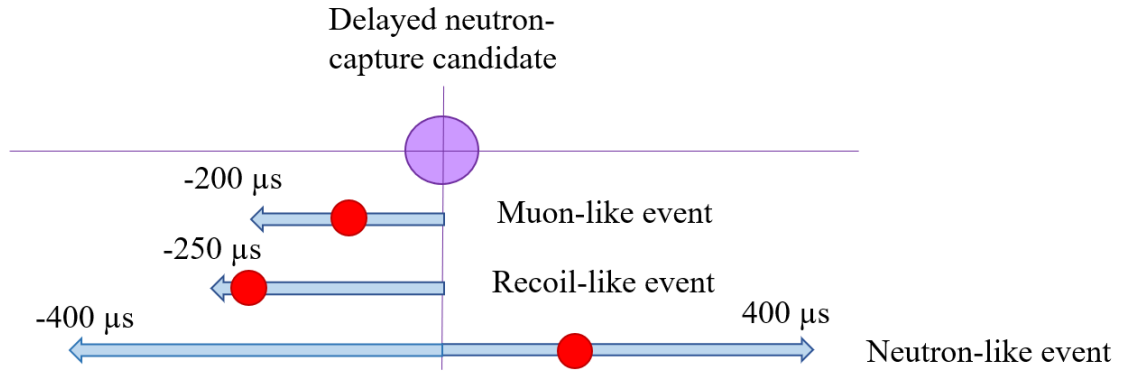


**Figure 4.10:** Scheme of implementation of cosmic shower veto. Delayed neutron-capture candidate is shown in purple, veto triggering events are shown in red, and time window are represented with blue arrows.

role study of their evolution plays in better understanding of the detector.

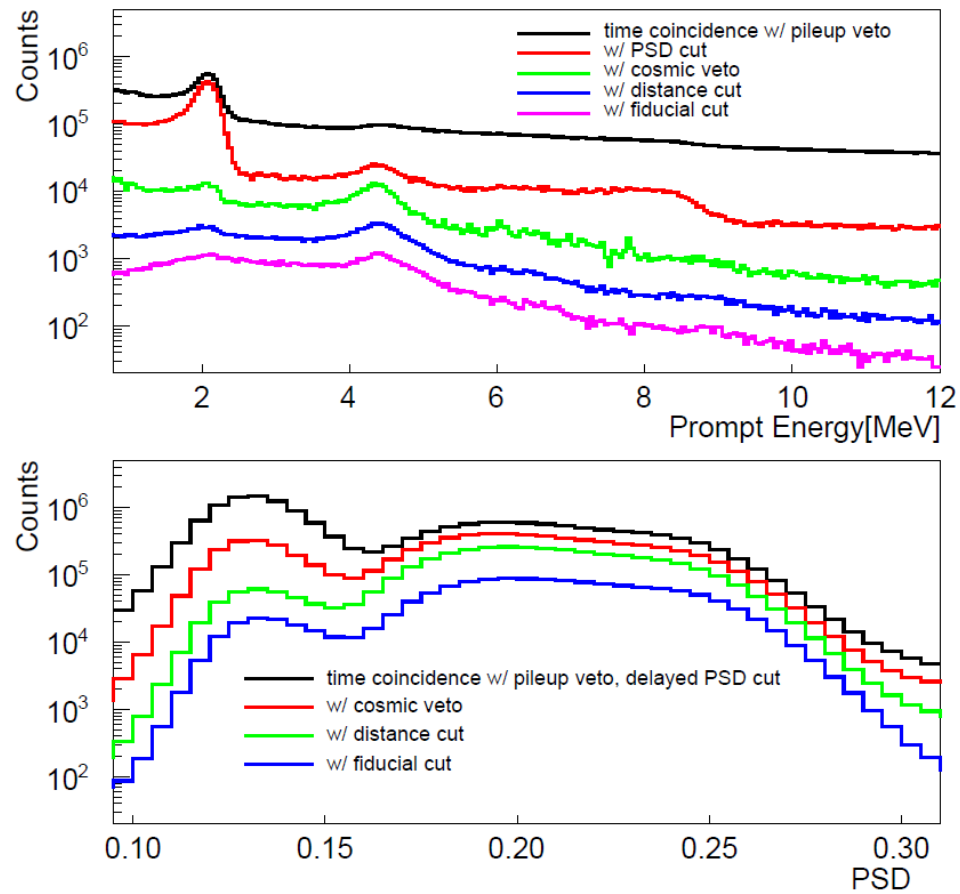


**Figure 4.11:** Smearing spectra of reconstructed energy of prompt event in IBD candidate. Spectra with different cuts illustrate the effectivity of these cuts. The accidentals are subtracted<sup>10</sup>.

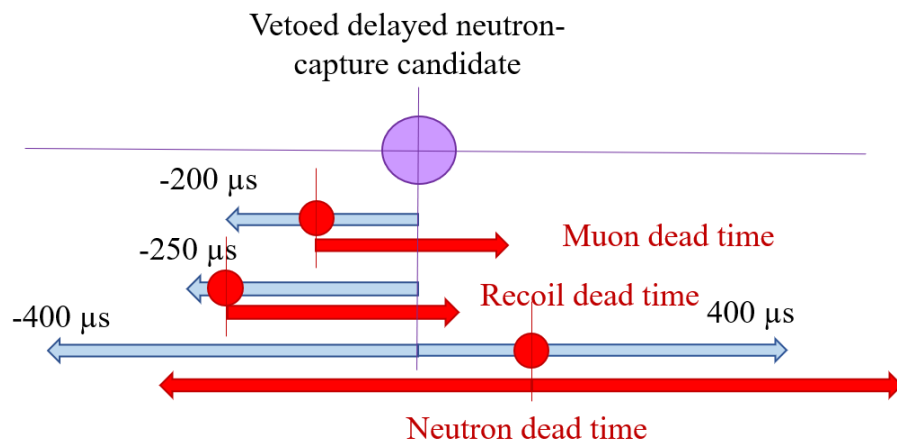


**Figure 4.12:** Scheme of calculation of dead time.

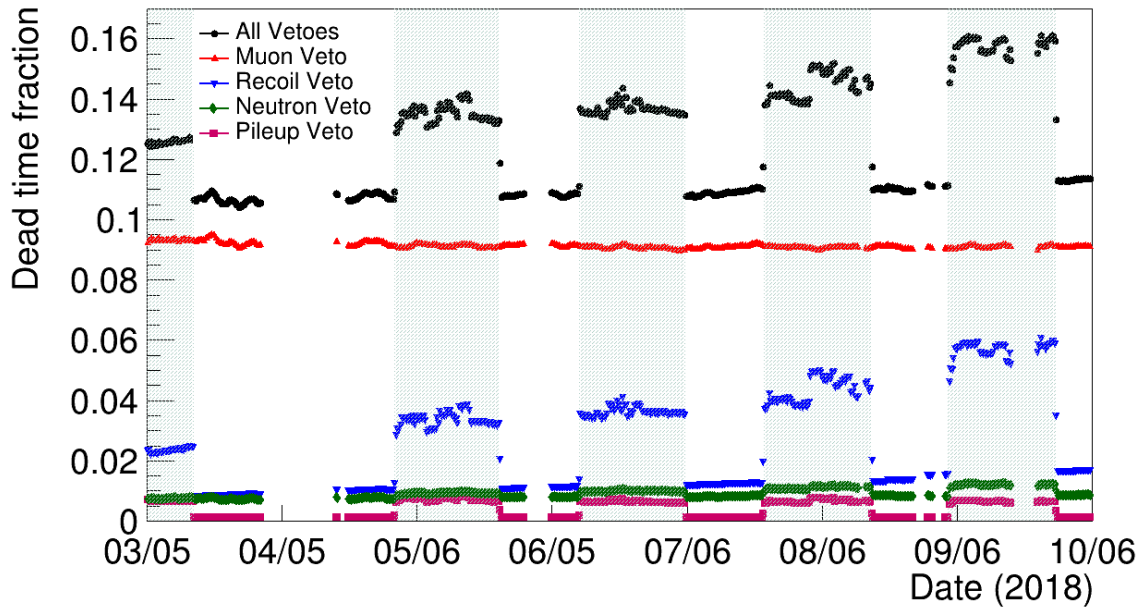


Figure 4.13: Comparison of deadtime for different types of vetoes over time.

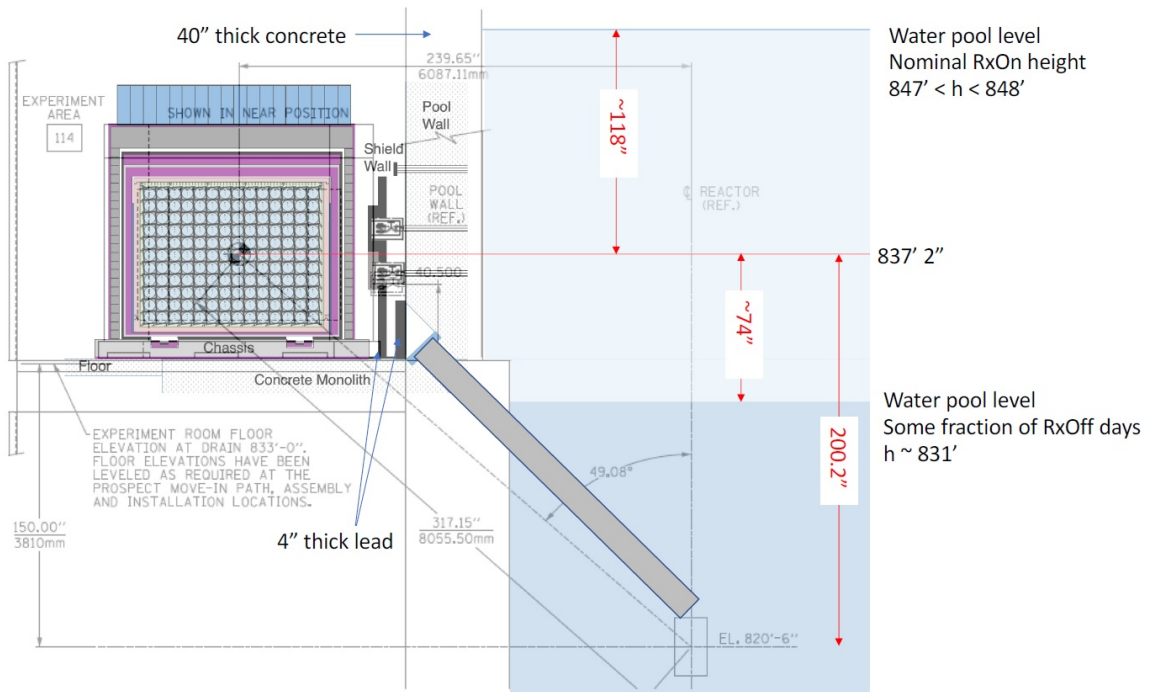
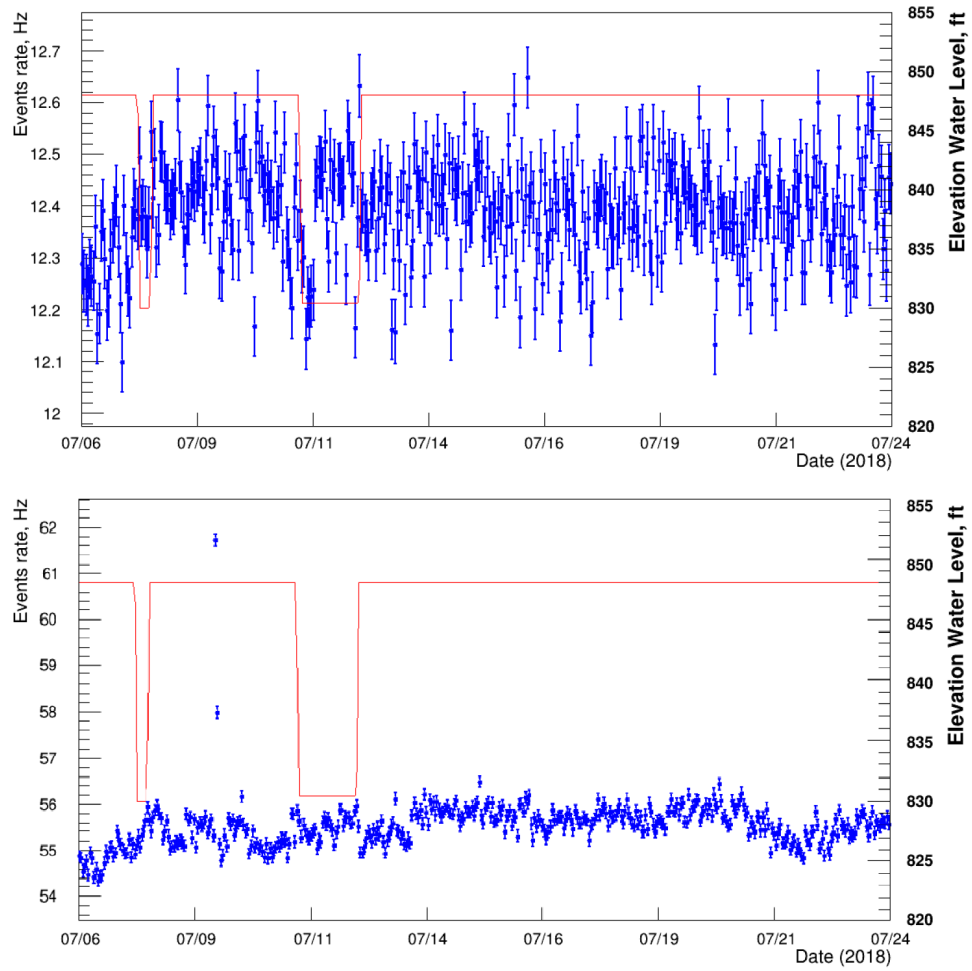


Figure 4.14: Reactor scheme of change of water level<sup>17</sup>.



**Figure 4.15:** The rates of single neutron capture events (top) and recoil-like single events (bottom) comparing to the water level drop in the period 07/06 - 07/24 when the longest water level drop happened. Water level is shown in red.

## Chapter 5: Prompt and Delayed Singles Analysis and Detector Stability

IBD-like coincidence events consist of prompt gamma-ray event, and delayed neutron capture on  ${}^6\text{Li}$ . To understand better our background, we present here a study of single prompt-like events and single delayed-like events.

### 5.1 Prompt-like Single Events

#### 5.1.1 Selection of Prompt-like Single Events

Prompt-like events are selected in a way so that for multi-pulse events each pulse in a cluster must have PSD within  $2\sigma$  from the center of the gamma-band. Therefore, every pulse has to be in the gamma-band. Table 5.1 summarizes the cuts on prompt-like singles. Fiducial cut excludes the events from outer layer of segments (top and bottom rows, and right and left columns of segments) and segments 25 and 26. Fiducial cut also excludes events close to PMTs: with  $z$  either  $> 444$  mm, or  $< -444$  mm.

**Table 5.1:** Cuts for prompt-like single events.

	Cluster size	Energy, MeV	PSD	Other
Prompt-like event	$\geq 1$ pulse	$0.8 < \text{C.Esmear}()$ $\text{C.Esmear}() < 15$	Each pulse P in cluster C with energy $> 0.1$ MeV has PSD $< 2\sigma$ above center of $\gamma$ -band	Fiducial cut Not OCS signal Pileup veto

Fig. 5.1 illustrates PSD and energy cuts for the prompt-like events for one run during reactor-on and one run during reactor-off periods. The PSD-energy distribution is plotted for a pulses with maximum energy in the selected clusters, and PSD here is the PSD of this pulse, while energy is a total non-smearred energy of the cluster.

A pileup veto, described in Chapter 4, is applied for prompt-like delayed candidate. The rates were adjusted after taking into account the pileup veto dead time. The scaling factor used for

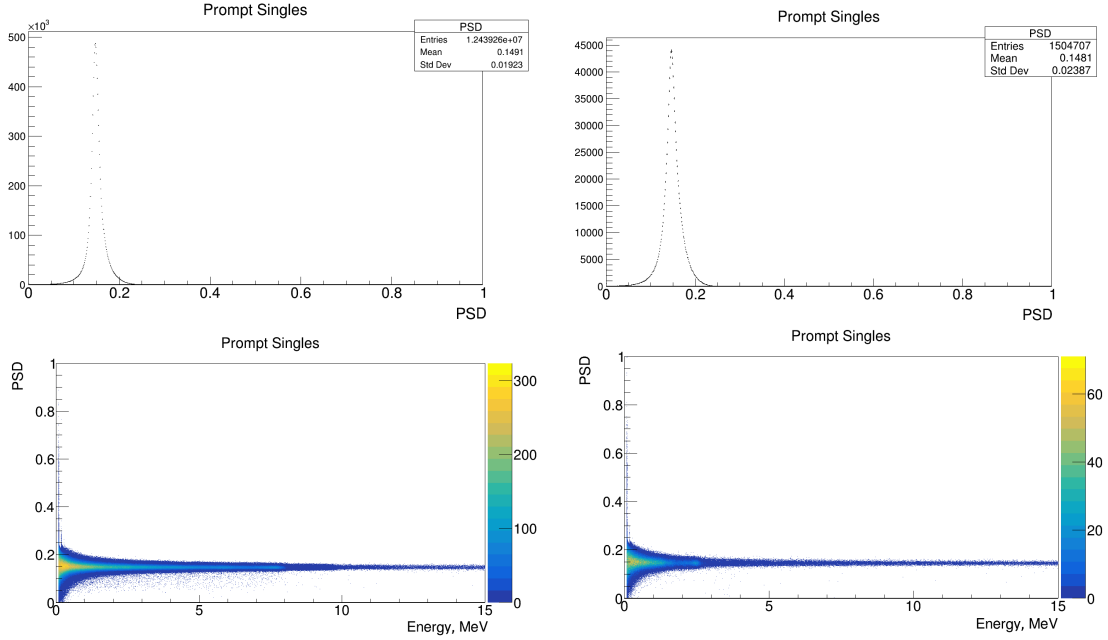


**Figure 5.1:** Illustration of cuts on single prompt-like events. Total PSD distributions and PSD vs energy distributions are shown for one run for reactor on (on March 5th, left plots) and reactor off (on March 16, right plots)

adjusting rate of single events has the form:

$$\text{Scaling factor} = \frac{\text{runtime}}{\text{runtime} - \text{deadtime}}, \quad (5.1)$$

where runtime is a total duration of the run, and deadtime is calculated in the same run. The pileup deadtime fraction with respect to runtime over the whole dataset timeline is shown in Fig. 4.13. Since the deadtime is created for every cluster in our detector, it correlates with the total rates, and we can see the significant increase of deadtime fraction during reactor-on periods, shown with green belts.

### 5.1.2 Rates and Energy Spectra of Prompt-like Single Events

The cumulative energy spectra for prompt-like candidates are shown in Fig. 5.2. The rates have been collected over the whole PROSPECT data taking timeline, and adjusted to deadtime. Reactor on periods are combined together and plotted in green, whilst combined together reactor off periods are plotted in blue. The spectra are shown in logarithmic scale.

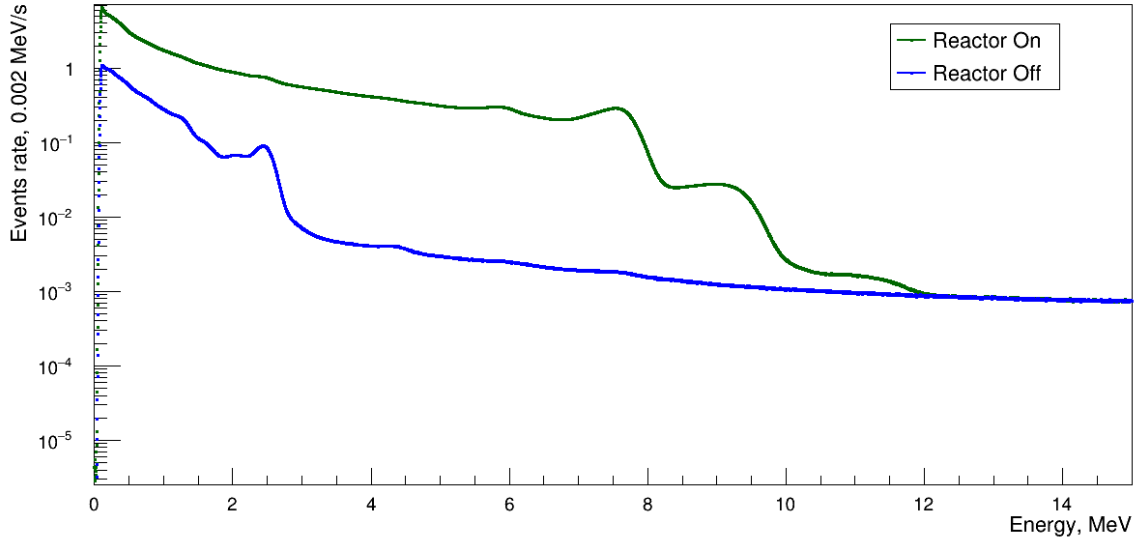


**Figure 5.2:** Cumulative spectra of prompt-like singles for reactor on and reactor off periods.

The spatial distribution of rates of prompt-like single events is shown in Fig. 5.3. Left plot shows rates during reactor on periods, and right plot rates during reactor off periods. Both plots are cumulative which means that they combine rates during reactor on and reactor off periods over the whole PROSPECT timeline and adjust for deadtime. The plots do not include non-fiducial segments. Missed segments are segments that were not include in the current analysis due to being turned off because of the ingress process.

During reactor-on periods, the gamma-ray background, coming from the reactor is so high that it dominates any other background. The rates in the bottom back corner are significantly (2-10 times) higher than in other parts of the detector. These events leak to the so-called "hot spot" because the concrete monolith does not support this part of the detector, and the floor does not provide as strong shielding from the gamma-rays (Fig. 3.3). During reactor-off periods, the difference in rates throughout the detector is substantially less and reaches up to 2 times difference between segments in the center of the detector and the outer part of the detector.

The time evolution of the prompt-like singles rates is shown in Fig. 5.4. The rates are adjusted to deadtime, and the spectrum was separated in five energy bins (0.25-0.75 MeV, 0.75-1.7 MeV, 1.7-3.2 MeV, 3.2-5.5 MeV and 5.5-15 MeV). The rates drastically and almost immediately go up

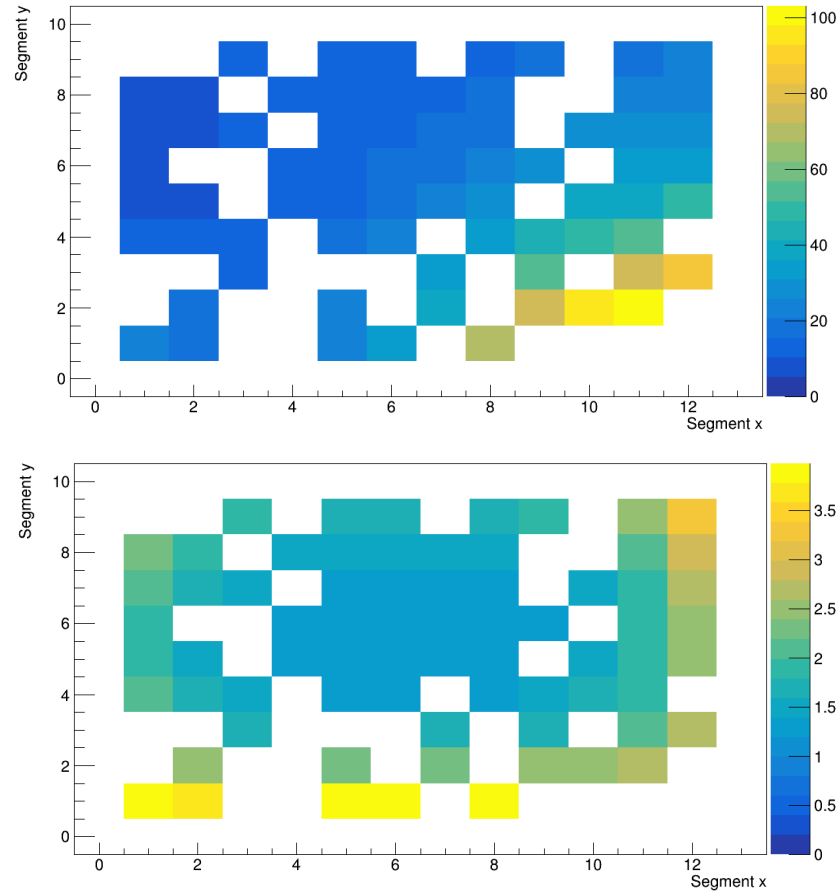


**Figure 5.3:** Cumulative rates of prompt-like singles per segment during reactor on (top) and reactor off (bottom) periods.

during reactor-on periods (shaded in green belts), and drop once the reactor is stopped. The visible and significant variations of rates during reactor-on is caused by gamma-ray activity from neutron scattering experiments, conducted in the building during reactor-on periods. The identical behavior between rates of different energies shows consistency of gamma rays rates with the neutron experiments. The gaps in the rates during reactor-on and reactor-off periods are caused either detector maintenance in early April, or detector stop in late September.

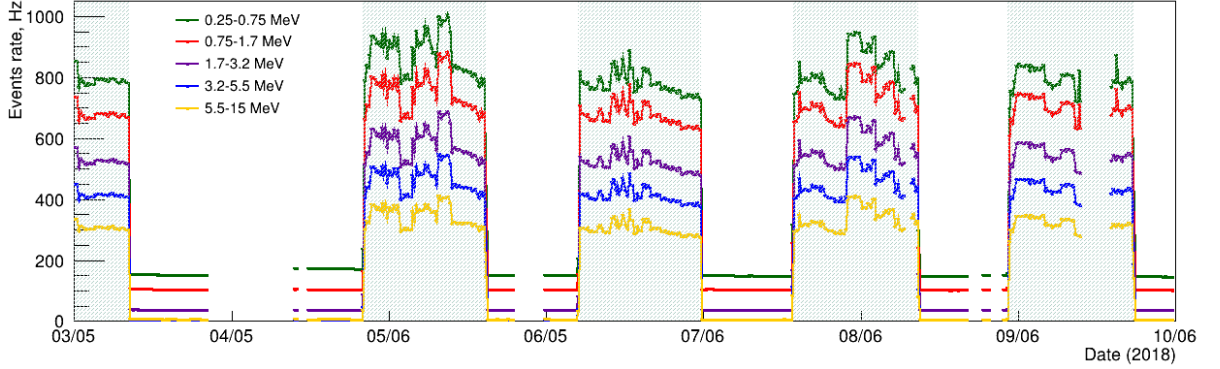


**Figure 5.4:** Rate of prompt-like singles vs time for different energy bins

### 5.1.3 Prompt-like singles peaks stability

To show consistency of spectrum features with time, for RxOff and RxOn a peak of Tl-208 decay and neutron scattering correspondingly were chosen and fitted with the function:

$$A_{Gauss} \times e^{-\frac{(x-mean)^2}{2\sigma^2}} + A_{Erfc} \times Erfc\left(\frac{x-mean}{\sqrt{2}\sigma}\right) \quad (5.2)$$

This function fits gamma-rays with a Gaussian peak distribution and models a continuum background with an error function.

For reactor off periods, the peak was fitted within energies 2.35-2.65 MeV with initial values of  $A_{Gauss} = 0.653746$ ,  $mean = 2.47847$ ,  $\sigma = 0.136389$ ,  $A_{Erfc} = 0.154587$ . For a better statistics in the fit, the rates were combined into 48 hours bins. An example of Gaussian fit for one time bin is shown on Fig. 5.5. The results for mean energy and width of the peak evolution with time are presented on Fig. 5.6 and Fig. 5.7 and show the consistent stable behavior over time.

For reactor on, the peak was fitted within energies 7.39-7.98 MeV with initial values of  $A_{Gauss} = 0.491573$ ,  $mean = 7.59448$ ,  $\sigma = 0.234050$ ,  $A_{Erfc} = 0.0985314$ . Each data point also includes 48 astronomical hours. An example of Gaussian fit for one time bin is shown on Fig. 5.8. The results for mean energy and width of the peak evolution with time are presented on Fig. 5.9 and Fig. 5.10 and show slight detector evolution over time.

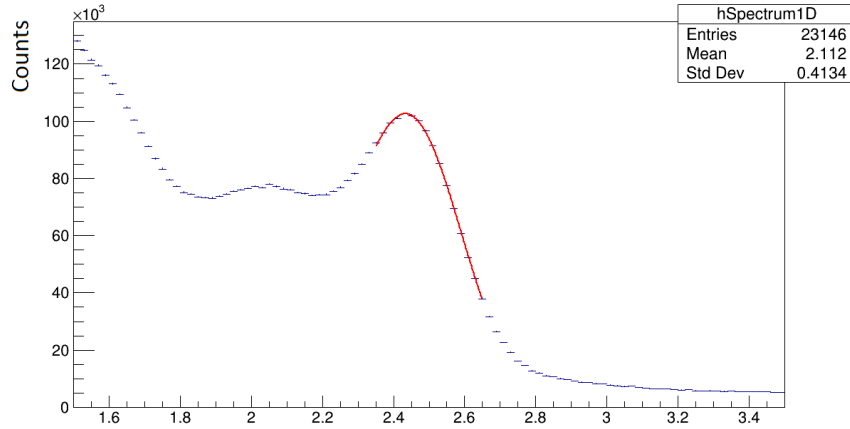


**Figure 5.5:** Fitted value of the peak of Tl-208 shown for one time bin of 48 hours during reactor off period.

## 5.2 Delayed-like Single Events

### 5.2.1 Selection of Delayed-like Single Events

Delayed-like candidates are selected from the general pool of neutron capture events (PSD cut) with additional fiducial and shower veto cuts. The events have to have only one pulse in the cluster with defined energy and PSD around neutron capture energy peak. The fiducial cuts is identical to the one described in Sec. 5.1.1. Since the delayed-like events have a sufficient risk of having cosmogenic nature rather than coming strictly from IBD, we apply shower veto to avoid cosmogenic neutron contamination of the signal. Shower veto is caused by three different types of background events: muon-like events, neutron-like events, and recoil-like events and the procedure is described in details in Chapter 4. Table 5.2 summarizes the cuts on delayed-like singles.

**Table 5.2:** Cuts for delayed-like single events.

	Cluster size	Energy, MeV	PSD	Other
Delayed-like event	1 pulse	C.Etot is in range of $3\sigma$ around neutron capture energy peak	PSD $> -2\sigma$ around neutron capture PSD peak PSD $< 0.4$	Fiducial cut Shower veto

Fig. 5.11 illustrates PSD and energy cuts for the delayed-like events for one run during reactor on and one run during reactor off periods. The rates of delayed-like singles are scaled with deadtime in the same manner, as rates of prompt-like single events. The scaling factor formula has the same

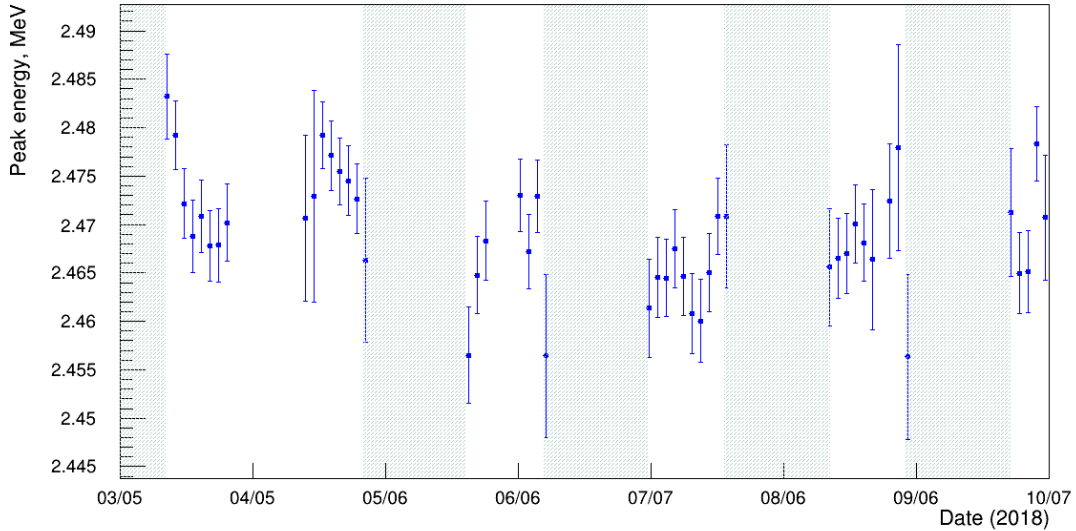


**Figure 5.6:** Mean energy of the peak Tl-208 vs time.

form as in 5.1.1. The total deadtime for cosmic veto is calculated overlapping the deadtime for cosmic veto components, as shown in Fig. 4.13.

### 5.2.2 Rates and Energy Spectra of Delayed-like Single Events

The energy spectra for delayed-like events is shown in Fig. 5.12. The plot shows event rates as function of energy over the whole timeline for reactor on and reactor off periods. The reactor on spectrum, shown in green, has a higher rate than reactor off rate. This is happening because some portion of high-PSD gamma-ray activity contributes to the delayed-like signals, that also have high-PSD values.

Rates for delayed-like singles vs segment for reactor on and reactor off are shown in Fig. 5.13. The rates are averaged along the dataset separately for reactor on and reactor off.

The rates for delayed-like singles are mainly uniform, with a little increase near "hot spot" where concrete shielding is absent. The variations across the detector between segment rates reaches at maximum the factor of 2. Rates are also comparatively consistent during reactor-on and reactor-off periods.

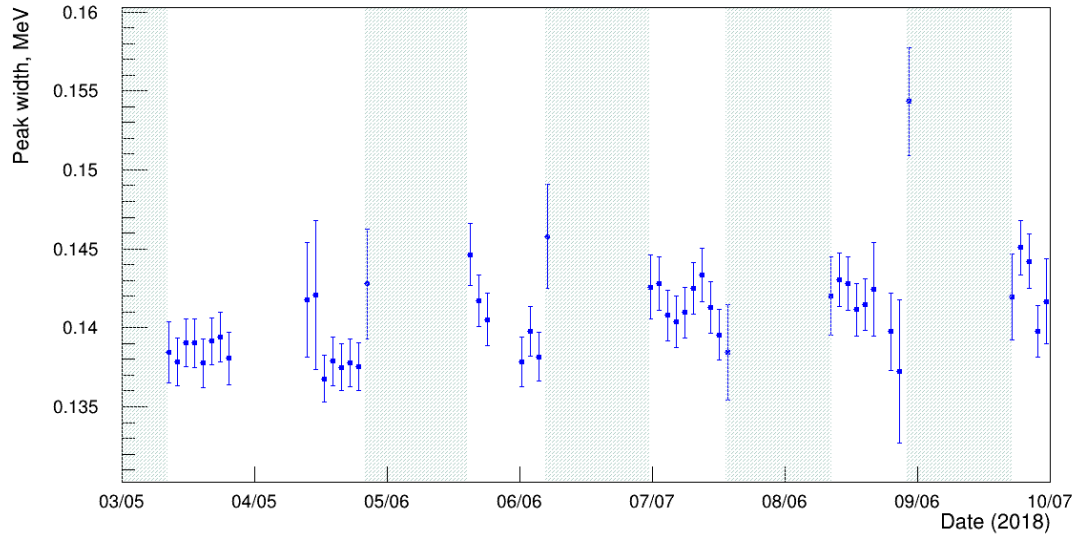


**Figure 5.7:** Width of the peak Tl-208 vs time.

### 5.2.3 Time Dependence of Delayed-like Rates

Rates of delayed-like singles with time over the whole PROSPECT timeline were obtained and plotted on Fig. 5.14. The rates are scaled with total overlapped deadtime for cosmogenic shower veto. The rates show increase over time and increase of reactor on periods compared to reactor off periods starting with the second reactor on period in May 2018. We can also see that this shift increases over time, showing a very significant difference during fifth reactor on period in September 2018. Both total increase of rates with time and shift during reactor on periods happen because of ingress in the detector that causes PMTs to detect extra events in recoil and neutron capture bands.

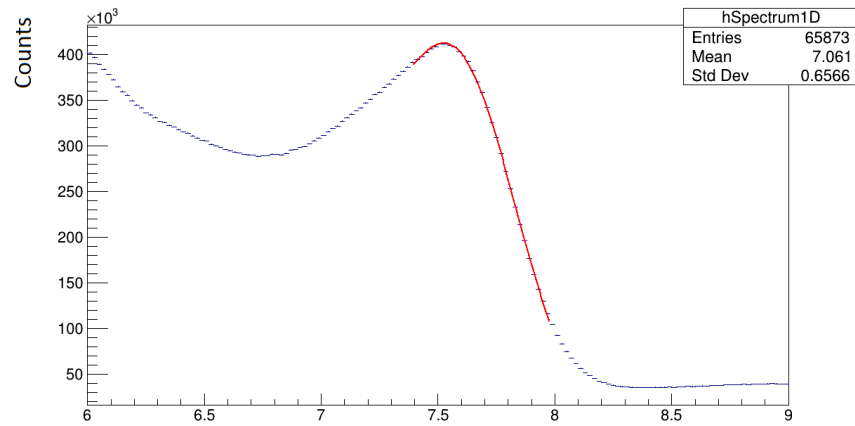


**Figure 5.8:** Fitted value of the peak at 7.7 MeV shown for one time bin of 48 hours during reactor on period

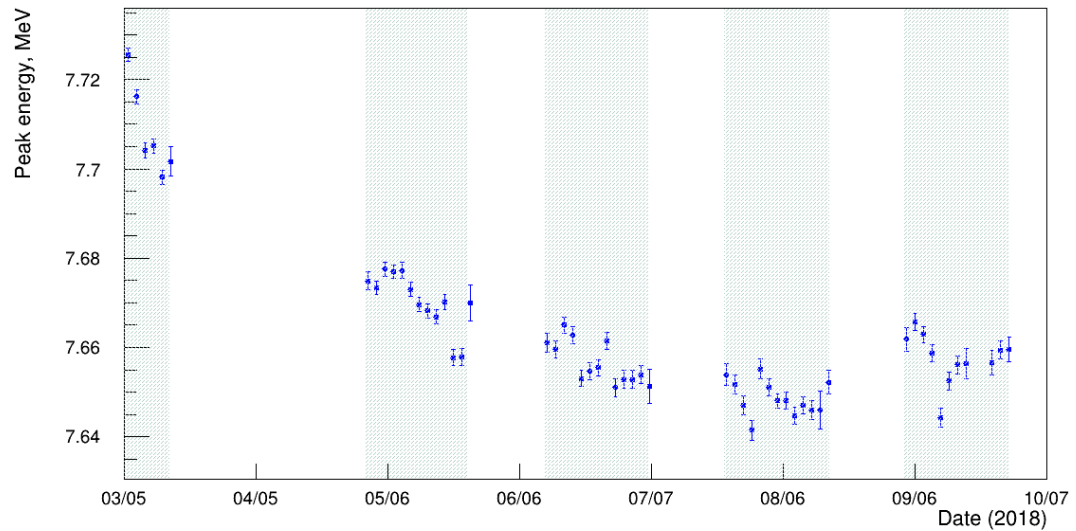


**Figure 5.9:** Mean energy of the peak at 7.7 MeV vs time.

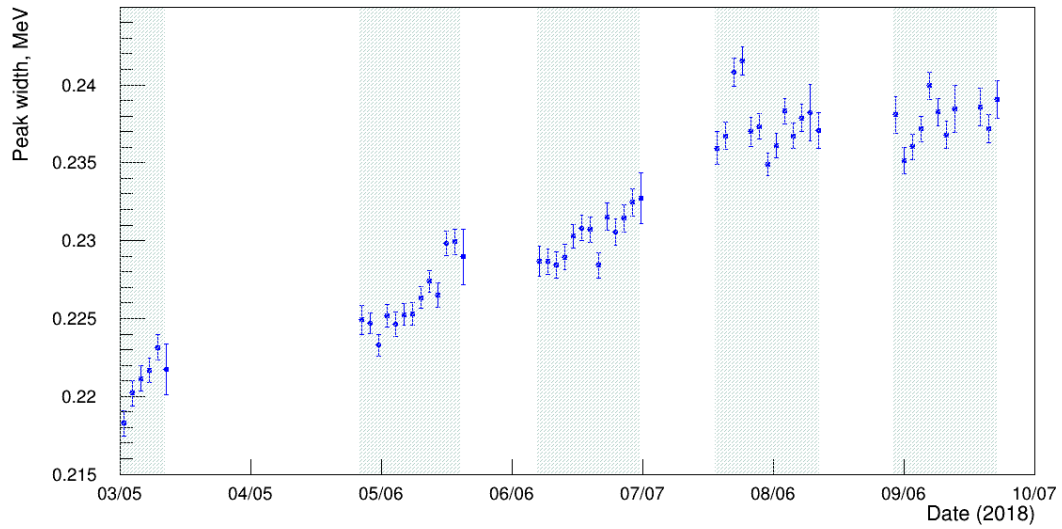


**Figure 5.10:** Width of the peak at 7.7 MeV vs time.

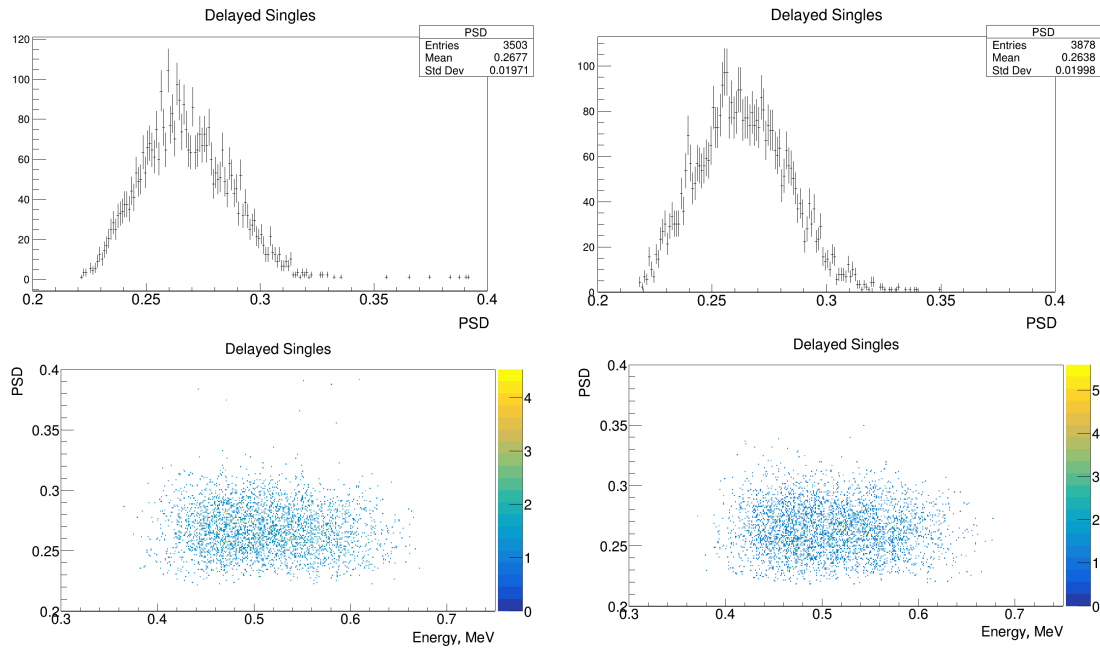


**Figure 5.11:** Illustration of cuts on single delayed-like events. Total PSD distributions and PSD vs Energy distributions are shown for one run for reactor on (on March 5th, left plots) and reactor off (on March 16, right plots)

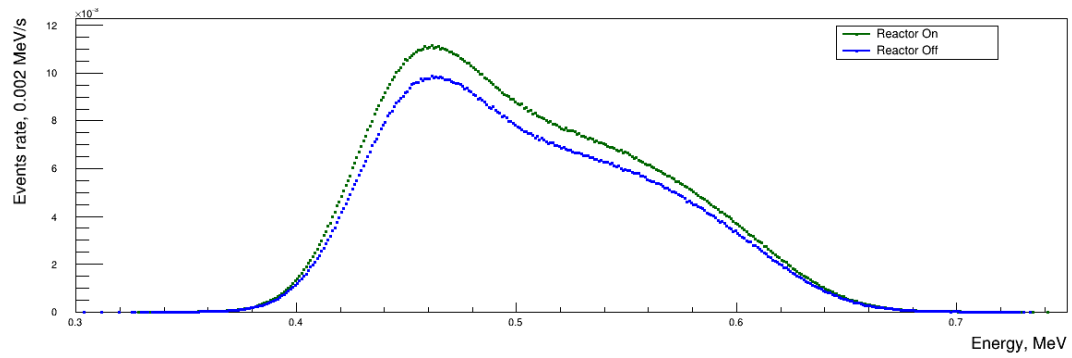


**Figure 5.12:** Energy of delayed-like singles for reactor on (blue) and reactor off (green)

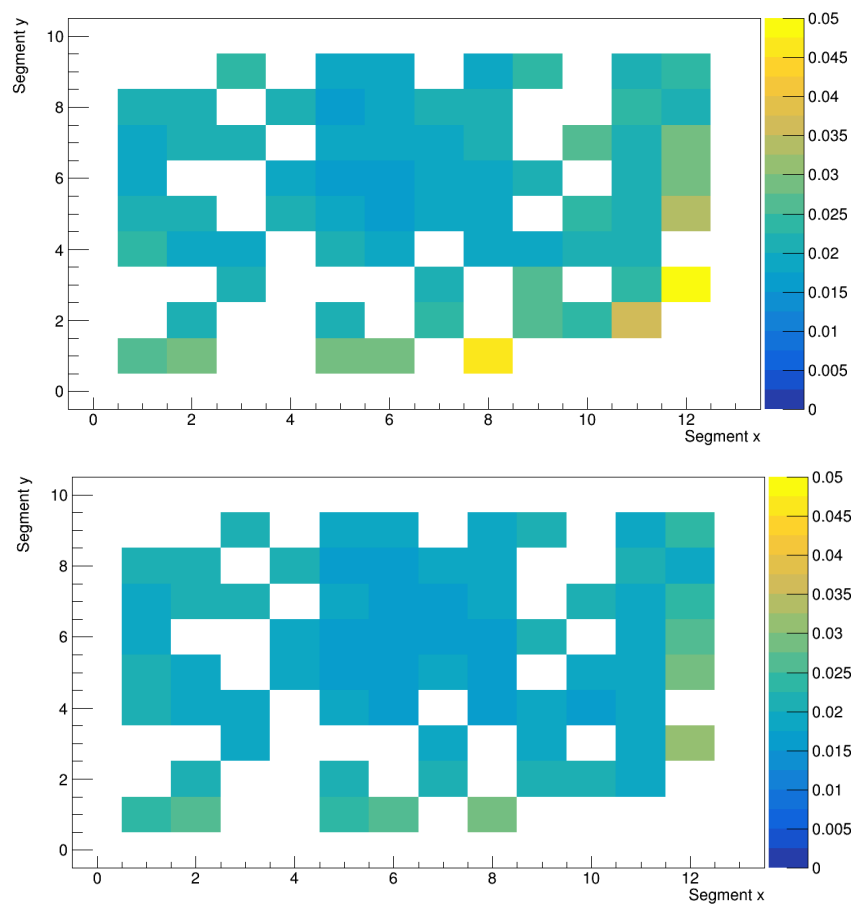


**Figure 5.13:** Cumulative rates of delayed-like singles per segment during reactor on (top) and reactor off (bottom) periods.

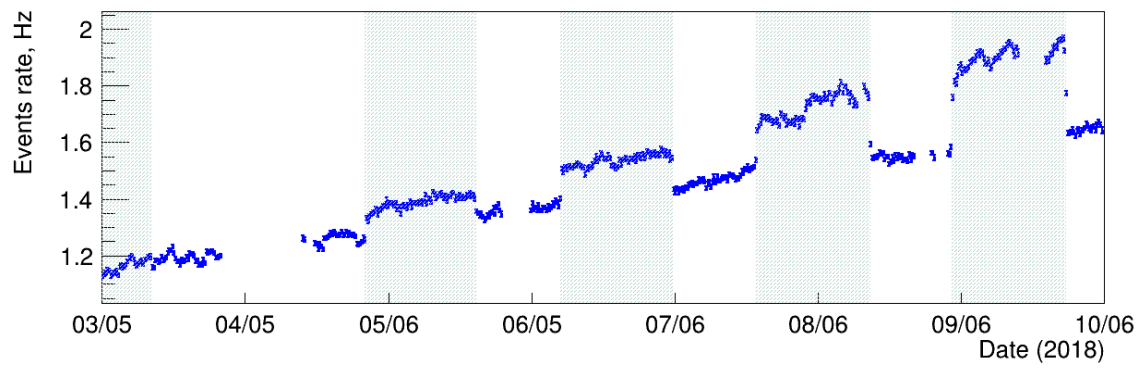


**Figure 5.14:** Time evolution of rates of delayed-like singles.

## Chapter 6: Coincidence Analysis and Background Scaling

### 6.1 Coincidence Analysis

The primary background for PROSPECT IBD-like events can be divided into two parts: accidental coincidences of gamma-rays from the reactor with (n,  ${}^6\text{Li}$ ) captures and time-correlated cosmogenic neutron background.

A recoil of a fast neutron from the nucleus of an atom in the scintillator and its subsequent capture on  ${}^6\text{Li}$  tracking is aimed to study the evolution of fast neutron background with time and its average variations in reactor-on vs reactor-off rates for estimation of reactor-on fast neutron contribution to our IBD-background.

The class of nLi + nLi coincidences requires each of neutron captures on  ${}^6\text{Li}$  to pass the same cuts as delayed-like single event plus happen in the same topology and time delay requirements, as IBD-like pairs. The goal of this class of events is to track the generation of multi-neutron showers with time and comparison between reactor-on and reactor-off rates.

Another goal for both types of coincident backgrounds is to look at their environmental parameters dependence, specifically dependence on atmospheric pressure for later scaling of IBD signal cosmogenic background with pressure before the background subtraction.

In this chapter, I study the recoil + nLi and nLi + nLi coincidence backgrounds, IBD-like coincidence events, look at their time and pressure dependence, discuss pressure scaling procedure, and discuss PROSPECT spectrum and sterile neutrino oscillation results in Section 6.4.

#### 6.1.1 Coincidence Events Cuts

Three type of coincidence events are discussed in PROSPECT experiment: IBD-like pairs, discussed in Chapter 3 that contain only cosmogenic background during reactor-off periods, and cosmogenic background plus IBD-signal from the reactor during reactor-on periods; recoils + nLi coincidence events and nLi + nLi coincidence events. The later two have clear cosmogenic origin and are not

supposed to show the reactor-on increased rate. Since both of them have cosmogenic nature, they are also expected to scale with atmospheric pressure.

The coincidence type of events share the same topological and time cuts, as long as the same shower and trigger vetoes discussed in Chapter 5. The following fiducial cuts were applied:

- $z_{\min} = -444$ ,  $z_{\max} = 444$ ,  $x_{\min} = 1$ ,  $x_{\max} = 12$ ,  $y_{\min} = 1$ ,  $y_{\max} = 9$
- Segments 25 and 26 were excluded

The following cuts for distance and time separation between prompt and delayed signals were used:

- Distance separation: 140 mm along z-axis (segments are in the same segment), 100 mm along z-axis (events are in adjacent segments)
- Time separation: from 1 to 120  $\mu\text{s}$  for the actual rates and from 17020  $\mu\text{s}$  to 5120  $\mu\text{s}$  for accidentals

The cuts applied on prompt and delayed signals are presented in Table 6.1. The cut on delayed event - neutron capture - is the same for all 3 types of events, and it is also the same cut as for prompt event in  $n\text{Li} + n\text{Li}$  coincidence. This is also the same cut as in delayed-like singles, described in Chapter 6. The cut on prompt-like event in IBD-like pairs is the same as cut on prompt-like singles in Chapter 6.

The following pileup preceding veto was used for all prompt events:

- If another, any cluster from (-800 ns, 0) time window happened before prompt event - the signal was vetoed.

For the single veto-causing events, described in Chapter 5, the following shower veto windows were introduced:

- One-sided preceding muon veto from (-200  $\mu\text{s}$ , 0) around delayed neutron-capture.
- One-sided preceding recoil veto from (-250  $\mu\text{s}$ , 0) around delayed neutron-capture.
- Double-sided neutron veto from (-400  $\mu\text{s}$ , 400  $\mu\text{s}$ ) around delayed-neutron capture.

**Table 6.1:** Cuts for prompt and delayed events for IBD-like, recoil + nLi, and nLi + nLi coincidences. The delayed event for these pairs has the same cuts.

	Cluster size	Energy, MeV	PSD	Other
IBD prompt	$\geq 1$ pulse	$0.8 < C.Esmear()$ $C.Esmear() < 7.2$	Each pulse P with $E > 0.1$ MeV has $PSD < 2\sigma$ above center of $\gamma$ -band	Not OCS signal Pileup veto
Recoil prompt	$\geq 1$ pulse		If at least one pulse with $0.6 < P.E < 10$ MeV, is not ingress hit by its PID, and $P.PSD > 4\sigma$ above $\gamma$ -band	Not OCS signal Pileup veto
n-Li prompt	1 pulse	C.Etot is in range of $3\sigma$ around neutron capture energy peak	$PSD > -2\sigma$ around neutron capture PSD peak $PSD < 0.4$	Not OCS signal Pileup veto
n-Li delayed	1 pulse	C.Etot is in range of $3\sigma$ around neutron capture energy peak	$PSD > -2\sigma$ around neutron capture PSD peak $PSD < 0.4$	Shower veto

Shower veto and pileup deadtimes are inserted into interval vectors for prompt main, prompt accidental, delayed main and delayed accidental rates. Inserting in special interval vectors allows to solve the overlapping issue with of different time intervals. A special function merges them into 4 single time intervals, and deadtime for each of 4 cases is calculated. Then, veto deadtime correction is calculated with the formula<sup>87</sup>:

$$\text{Deadtime correction coefficient} = \frac{t_{run}^2}{(t_{run} - t_{dead}^{prompt})(t_{run} - t_{dead}^{delayed})} \quad (6.1)$$

separately for main and accidental rates.

### 6.1.2 Coincidence Analysis Accidentals Subtraction

The structure of PROSPECT analysis is made in a way that the data are separated into periods of approximately one hour each, called runs, with some dead time between the runs for relaunching the data acquisition system. The time of the start of each run is fixed in its name and the technical description, and the timer of the events defined as a function *getTime()* inside each run starts from zero. For better handling of the events, all the runs were added on the same absolute timeline (March 5th, 2018 - October 7th, 2018) and therefore the absolute time of each event was obtained

with the formula:

$$\text{Timestamp (event)} = \text{absoluteTime (start of run)} + \text{Timestamp (event) inside the run} \quad (6.2)$$

Here, timestamp (event) relative to the beginning of the run is a result from function getTime() (1, 2, ..., 3600 s), and absoluteTime (start of run) is a timestamp stored in run's name. After this procedure, a full time line of rates is obtained.

Since for the coincidence event pairs we need to subtract accidental coincidences from the actual rate, two types of time lines are obtained for each type of events. Below, by "actual" I call events that are in the time window of 1  $\mu\text{s}$  to 120  $\mu\text{s}$  preceding delayed event (the cut for IBD events), and by "accidentals" I call events that are in the time window of -17020  $\mu\text{s}$  to -5120  $\mu\text{s}$  preceding delayed event.

As discussed in Section 6.2.2, the frequency of pressure data points I use is one pressure value per hour, initially I combine events rates into 1 hour-bins. Each rate point in Hz for actual events and for accidentals is calculated as:

$$Rate_i^{actual/accid} = \frac{\text{Total number of actual/accidental counts in } i\text{'s 3600s-bin}}{\text{Live time within } i\text{'s 3600s-bin}}, \quad (6.3)$$

and uncertainty for each actual/accidental rate data point is calculated with the formula

$$\sigma_i^{actual/accid} = \frac{\sqrt{\text{Total number of actual/accidental counts in } i\text{'s 3600s-bin}}}{\text{Live time within } i\text{'s 3600-s bin}}. \quad (6.4)$$

After subtraction, subtracted rate is:

$$Rate_i^{subtr} = Rate_i^{actual} - 0.01 \cdot Rate_i^{accid}, \quad (6.5)$$

and final uncertainty of each subtracted rate data-points is:

$$\sigma_i^{subtr} = \sqrt{\sigma_{actual}^2 + (0.01 \cdot \sigma_{accid})^2} \quad (6.6)$$

Here, 0.01 is accidentals scaling coefficients that is equal to  $(120 \mu\text{s} - 1 \mu\text{s}) / (17020 \mu\text{s} - 5120 \mu\text{s})$ . The uncertainty for each subtracted rate data point together with uncertainty of each pressure measurement are used for obtaining linear fit coefficients  $a$  and  $b$  ( $p1$  and  $p0$ ) and their uncertainties  $\sigma_a$  and  $\sigma_b$ .

1-hour time bin is the finest time bin that is allowed in the current analysis. However, since the timeline of PROSPECT covers 8 months, the time bins with better statistics are more useful and produce less statistical uncertainty. A special built-in function allows to combine the data from the overall timeline to any integer number of hours. The most used are 4, 8, 24 and even 48 hours. Also, the script, used to obtain rate-pressure plots, in addition prepares a plot, showing what portion of each rate data point contains real data (Fig 6.1). Because due to non-uniformity of runs, in principle, 1-hour time bin can have as low as 1 s of live time, due to lack of statistics, such rate data points can be significantly off of average events rate. To avoid those off points, I introduce a threshold: each hour-bin must contain at least 3100 s of live time. The value of 7200 s was picked empirically for time binning of 4, 8, and 24 hours. For time binning of 2 hours, the threshold is 3600 s. Fig. 6.1 also shows that the usual amount of data points that do not pass this threshold is small.

## 6.2 Background Subtraction

### 6.2.1 Background Scaling with Pressure

As was discussed in Chapter 4, the equation for the atmospheric pressure adjustment:

$$N_{adjusted} = N_{initial} e^{\beta(P_0 - P)}, \quad (6.7)$$

where  $P_0$  is a reference pressure. This is the law neutron monitor detectors use to scale their rates with pressure<sup>80</sup>. We will use this formula for estimation of barometric coefficient  $\beta$  in %/mb for quantitative comparison of pressure dependences of different types of events with known neutron monitor reference values.

Using Taylor expansion around the mean atmospheric pressure, we approximate this dependence

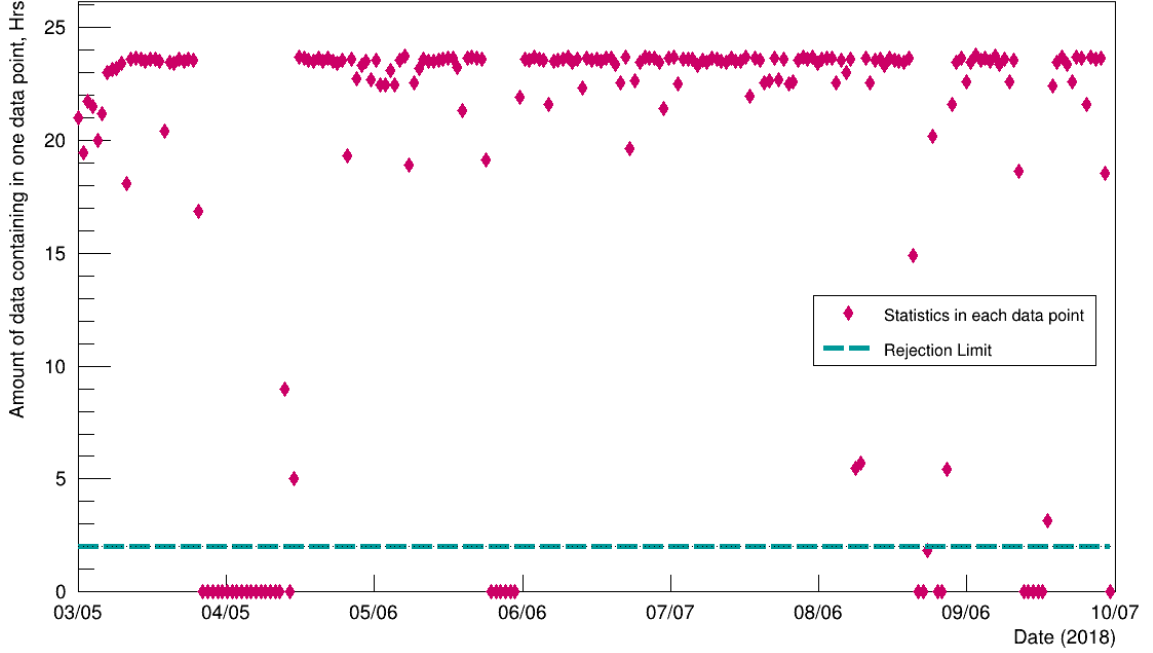


**Figure 6.1:** Plot of live time fraction of each data point when each time bin is 24 hours. The dashed line shows the cutoff limit: if the amount of the real data in the time bin is less than 2 hours, those data points got cut off.

with linear polynomial:

$$N = aP + b. \quad (6.8)$$

Due to linearity of this approximation, we can make a single scaling of reactor-off background on reactor-on based on average atmospheric pressure during each period. In this case, the scaling coefficient for pressure adjustment is:

$$\text{Scaling coefficient} = \frac{a \cdot \overline{p_{on}} + b}{a \cdot \overline{p_{off}} + b}, \quad (6.9)$$

where  $\overline{p_{on}}$  and  $\overline{p_{off}}$  are average atmospheric pressures correspondingly during reactor on and reactor off periods. Therefore, before the subtraction of RxOff spectrum from RxOn spectrum, we will scale

RxOff spectrum by run times and multiply by pressure adjustment scaling coefficient:

$$BG_{RxOff}^{subtr} = \frac{t_{On}}{t_{Off}} \cdot BG_{RxOff}^{initial} \cdot \frac{a \cdot \overline{p_{on}} + b}{a \cdot \overline{p_{off}} + b}. \quad (6.10)$$

Using error propagation formula for function  $u = u(x, y, z, \dots)$ :

$$\sigma_u^2 = \left(\frac{\partial u}{\partial x}\right)^2 \cdot \sigma_x^2 + \left(\frac{\partial u}{\partial y}\right)^2 \cdot \sigma_y^2 + \left(\frac{\partial u}{\partial z}\right)^2 \cdot \sigma_z^2 + \dots \quad (6.11)$$

we get the uncertainty of scaling coefficient:

$$\sigma_{coeff}^2 = \left(\frac{\overline{p_{on}} \cdot A_{off} - \overline{p_{off}} \cdot A_{on}}{A_{off}^2}\right)^2 \cdot \sigma_a^2 + \left(\frac{a \cdot (\overline{p_{off}} - \overline{p_{on}})}{A_{off}^2}\right)^2 \cdot \sigma_b^2 + \left(\frac{a}{A_{off}}\right)^2 \cdot \sigma_{\overline{p_{on}}}^2 + \left(\frac{a \cdot A_{on}}{A_{off}^2}\right)^2 \cdot \sigma_{\overline{p_{off}}}^2 \quad (6.12)$$

where  $A_{on} = a \cdot \overline{p_{on}} + b$ ,  $A_{off} = a \cdot \overline{p_{off}} + b$ ,  $\sigma_a$  and  $\sigma_b$  are errors for linear fit coefficients, and  $\sigma_{\overline{p_{on}}}$  and  $\sigma_{\overline{p_{off}}}$  are uncertainties in pressure measurements described in Section 6.2.2.

## 6.2.2 Average Pressures for Reactor-On and Reactor-Off Periods

The sources of data of the atmospheric pressure near HFIR is described in Appendix. The scaling factor described above is most sensitive to small variations in average atmospheric pressures. Thus, calculating correct average pressure for each period is the vital part of the procedure.

The simplistic calculations of average pressures during each reactor-off/reactor-on periods by hand proved causing a lot of mistakes, so a script was written to calculate average pressure for each period. The script utilizes 1/0 flags in the List of Good Runs for identification of reactor-on vs reactor-off runs.

To calculate average pressure correctly, we divide each 1 hour-time bin into 3600 bins for one bin for each second and fill them uniformly according to the pressure assigned for 1 hour time-bin. Thus, for the pressure  $P_1$  at 6:00 pm, we fill the time bins from 5:30 pm to 6:30 pm with this pressure, and next 3600 time bins from 6:30 pm to 7:30 pm we fill with pressure  $P_2$  that corresponds to 7:00 pm. For proper assigning timeline to the runs, we use the timestamp of the beginning of the run,

**Table 6.2:** Average pressure comparison between script’s and manual results for Period 1, Period 2 and Total from PRL paper dataset<sup>3</sup>.

	Script, inHg	Manual, inHg
Period 1, RxOff	29.0721	29.0723
Period 1, RxOn	29.1296	29.1290
Period 2, RxOff	29.0921	29.0912
Period 2, RxOn	29.1148	29.1149
Total, RxOff	29.0846	29.0817
Total, RxOn	29.1221	29.1220

written in its name, and run time written in the output file. For finding average pressure, we look at overlaps of runtimes with pressure time line (Fig. 6.2). Such approach solves the problem with non-uniformity of runs and excludes off-time between the runs that in some cases can reach two hours. As outcome, the script also gives total runtime for reactor-on/reactor-off periods which can be used as a check before background subtraction. The uncertainties for pressure according to their origin are also included in the calculation of average pressure.

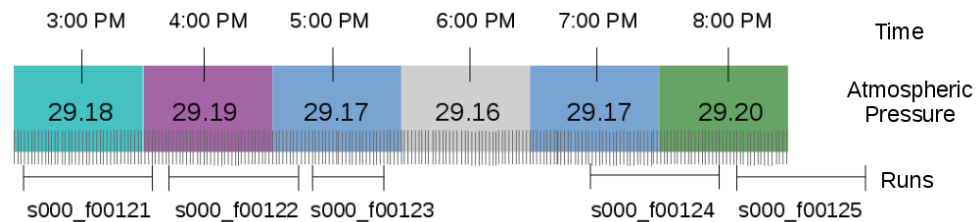


**Figure 6.2:** Overlapping of pressure time bins with runs

Average pressure results from the script were checked by manual calculation of the average: timeline is separated in large main periods for reactor-on and reactor-off and average pressure is calculated as a sum of pressures during that periods divided by the number of hours. The check was done for PRL dataset (March 5th - July 31st) only. The script/manual results comparison for Period 1, Period 2 and Total from<sup>3</sup> are presented in Table 6.2.

Average atmospheric pressures for studied events for the dataset used in the current analysis:

$$\overline{p_{on}} = 29.1137 \text{ inHg during } 2295.36 \text{ hours,}$$

$$\overline{p_{off}} = 29.1149 \text{ inHg during 1754 hours}$$

and uncertainty for each averaged pressure, calculated as  $\sigma_{\overline{p}} = \frac{\sqrt{\sum_i^N \sigma_{p_i}^2}}{N}$  is negligible:  $\sigma_{\overline{p_{on}}} = 7.18 \times 10^{-7} \text{ inHg}$ ,  $\sigma_{\overline{p_{off}}} = 1.08 \times 10^{-6} \text{ inHg}$ .

### 6.2.3 Barometric Coefficients

The  $\beta$  coefficient, mentioned in Section 6.2.1, called barometric coefficient, was calculated and compared for different types of events in PROSPECT analysis. For calculations of this coefficient, the fit of events rate vs atmospheric pressure was chosen exponential, as opposed to linear fit for scaling coefficients, and  $\beta$ -value was extracted from these fits. However, it is also interesting to compare the fit with the data, reported before in the literature.

The classic studies for fast neutrons rate barometric coefficients report  $-0.72/-0.73 \text{ \%/mb}$ <sup>81;82</sup>. On the other hand, some of the newer studies show  $-0.67 \text{ \%/mb}$ <sup>83</sup> and  $-0.57 \text{ \%/mb}$  for the newer model in recent study<sup>84</sup>.

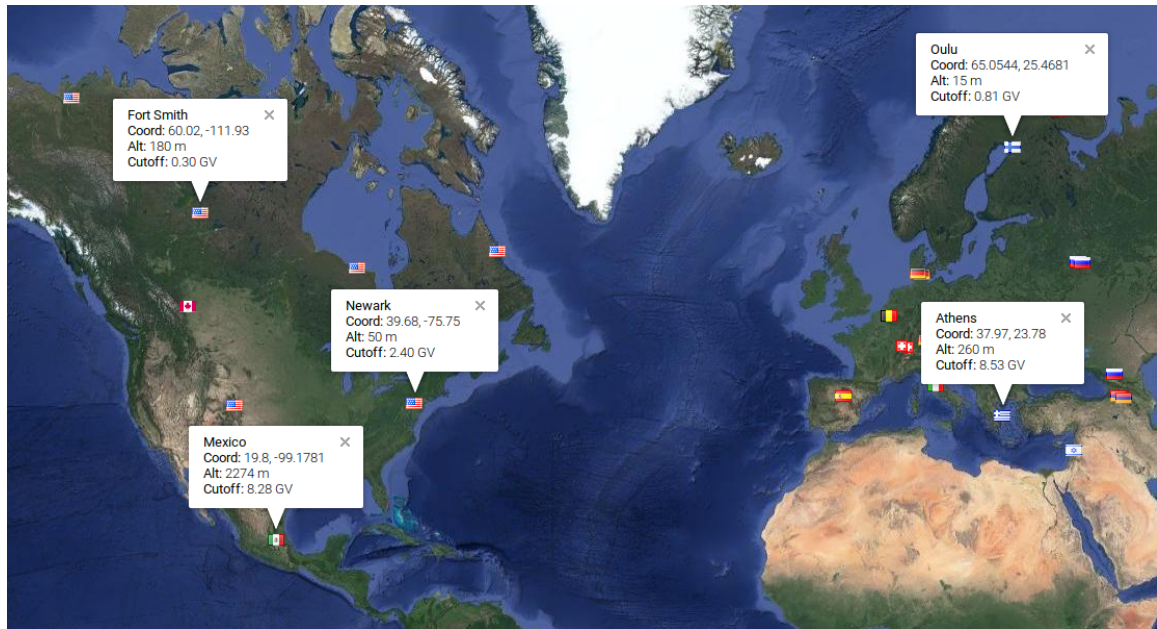


**Figure 6.3:** Neutron monitor stations locations

With online calculator at Athens Cosmic Ray station website<sup>89</sup>, we extract the barometric coefficients for the periods March 29 - October 6, 2018 for the following Cosmic Ray (Neutron Monitor)

Stations (Fig. 6.3):

- Newark (NEWK):  $-0.73 \pm 0.01$  %/mb
- Oulu (OULU):  $-0.75 \pm 0.01$  %/mb
- Mexico (MXCO):  $-0.71 \pm 0.00$  %/mb
- Athens (ATHN):  $-0.66 \pm 0.01$  %/mb
- Fort Smith (FSMT):  $-0.78 \pm 0.01$  %/mb

These barometric coefficients were used to compare with the barometric coefficients, obtained for background events, presented in this thesis.

## 6.3 Results

### 6.3.1 Evolution of Rates with Time and Pressure Dependence Inelastic Recoil and Neutron Capture Coincidences

The results for recoils + nLi coincidence events are shown in Fig. 6.4 and Fig. 6.5. The rate is stable with time and does not show the increase during reactor on periods, which means that ingress process does not leak in into the rates. There is also no increase of rates with time. Finally, the rate very well scales with atmospheric pressure not showing significant variation around the linear approximation.

#### Neutron Capture and Neutron Capture Coincidences

The results for nLi + nLi coincidence events are shown in Fig. 6.6 and Fig. 6.7. There is no significant increase during reactor on, the rate is stable and varies with atmospheric pressure. There is a slight drift up in rate with time. However, the average rate is very small and can reach 0.0145 Hz. The rate scales with atmospheric pressure.

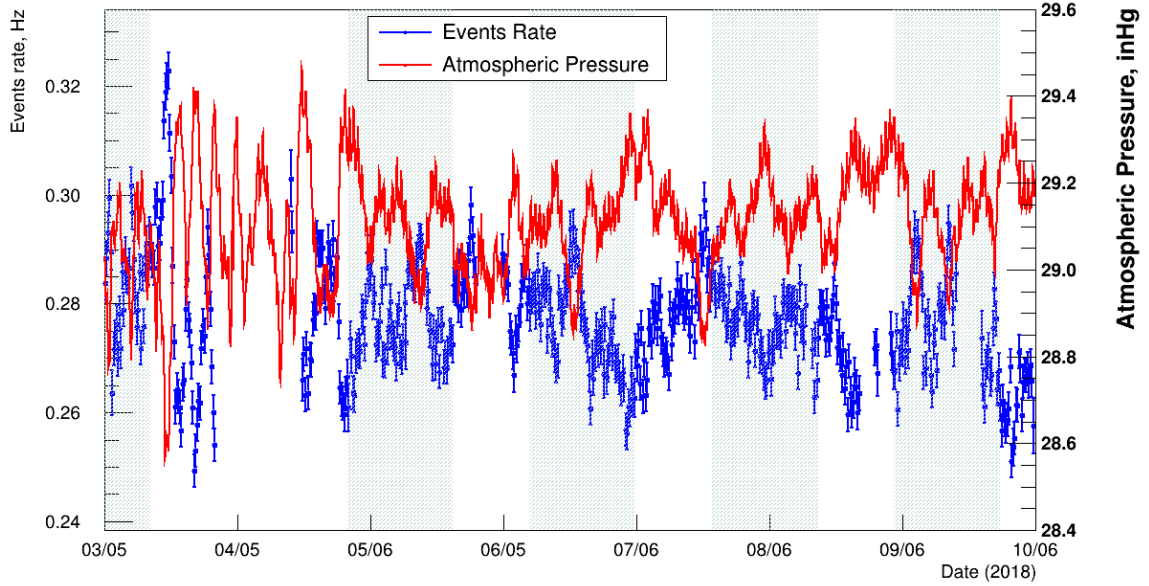


**Figure 6.4:** Rates of recoils + nLi coincidences with time. Each time bin is 8 hours.

### IBD-like Events

Fig. 6.8 shows a rate of IBD-like events per live day for the whole PROSPECT data taking timeline. The correlated events are shown in blue, while accidental rates are also plotted on this figure, in red. The accidental rates show significant time variation during reactor-on periods, which are mostly related to neutron experiments held in the room below PROSPECT detector. Very similar variations can be seen in the rates of prompt-like single events in Fig. in Chapter 5. However, we do not see those variations in the correlated events rates, which means that accidental coincidences in IBD-rates were accurately subtracted.

The clear shift in the rates of IBD-like events during reactor-on periods indicate a visible reactor antineutrinos signal. Smaller variations during both reactor-on and reactor-off periods are related to the variation of cosmogenic background with atmospheric pressure. The plots on Fig. 6.9 (a) shows that both reactor-off and reactor-on rates are scaling with pressure with approximately the same slope, and only shifted one comparing to another on a constant value. This shift is our IBD signal. For subtraction, we use the scaling coefficients, described in Section 6.2.1, from reactor-off fit only (Fig. 6.9 (b)).

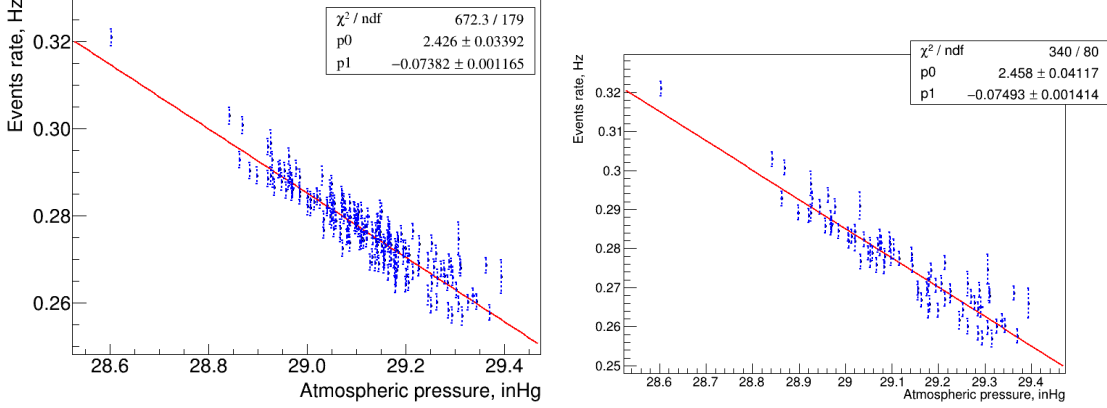


**Figure 6.5:** Rates of recoils + nLi events vs atmospheric pressure. Left: RxOn and RxOff periods. Right: RxOff only.

### 6.3.2 Average Rates, Barometric and Scaling Coefficients

**Table 6.3:** Rates, barometric coefficients, and on-off scaling coefficients for different types of single and correlated event categories.

Event type	Reactor-Off rate (Hz)	On-Off offset (Hz)	Barometric coefficient (%/mbar)	Scaling coefficient (%)
All events	1628	6708	-	-
Recoils	46.8	116	-	-
Neutrons	11.5	2.85	$-0.57 \pm 0.23$	$0.025 \pm 0.015$
Muons	497	-2.3	$-0.16 \pm < 0.01$	$0.006 \pm 0.000$
nLi + nLi	0.012	$8.5e-4$	$-0.53 \pm 0.01$	$0.022 \pm 0.024$
Recoil + nLi	0.33	$4.2e-4$	$-0.80 \pm 0.02$	$0.033 \pm 0.007$
IBD-like	0.0052	$7.1e-3$	$-0.70 \pm 0.01$	$0.028 \pm 0.048$

Fig. 6.4 shows the evolution of the recoils + nLi rate with time. The rate shows clear prominent variations with pressure, as long as a long-term downward drift with time. The average rate excess during reactor-on periods comparing to reactor-off periods consists less than 0.13%, which indicates that even though we see significant increase of single recoils during reactor operation, they do not appear in our coincidence rates. Thus, we also do not have to expect additional fast neutron background from the reactor leaking into our IBD spectrum. Therefore, we can consider that the subtraction of the recoil-related background, which is inelastic scattering on  $^{12}\text{C}^*$  (4.5 MeV peak in IBD-like spectrum), does not have to be additionally scaled to reactor-on mode. The decreasing

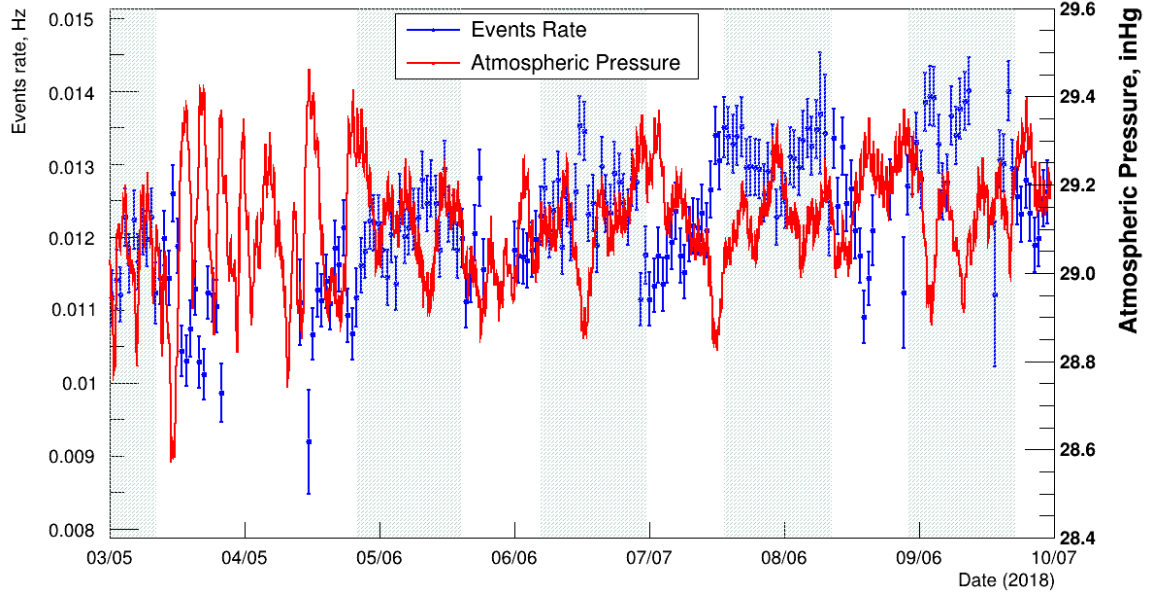


**Figure 6.6:** Rates of  $n\text{Li} + n\text{Li}$  coincidences with time. Each time bin is 24 hours.

trend with time can be caused by the seasonal variations.

Fig. 6.6 shows the upward drift of  $n\text{Li} + n\text{Li}$  coincidence rate with time, as long as daily variations with pressure. Some increase of average rates during reactor-on periods can also be seen, and constitutes about 7.1% of average rates. This increase can be explained if we remember that rates of single delayed-like events, described in Chapter 4, also show a) upward evolution with time; b) rise in rates during reactor-on periods, and c) increasing reactor-on/reactor-off difference with time. Overall, the small rate of  $n\text{Li} + n\text{Li}$  coincidences as well as a visible evolution of the detector on this small scale can indicate that the shower veto works efficiently, vetoing shower caused multi-neutron events throughout the whole experiment timeline.

Results for RxOn and RxOff average rates and barometric and scaling coefficients are summarized in Table 7.1. Results for coefficients of  $n\text{Li} + n\text{Li}$ , recoils +  $n\text{Li}$ , and IBD-like were taken from direct fits of events during RxOff periods with time-bins of 24 hours (as shown on Fig. 6.7b, 6.5b, and 6.9b, correspondingly). Considering the small difference in the atmospheric pressure between reactor-on and reactor-off periods, the scaling coefficients calculated from fits of all different types of events are very small and constitute  $(0.028 \pm 0.048)\%$  for IBD-like events. The barometric coefficients from

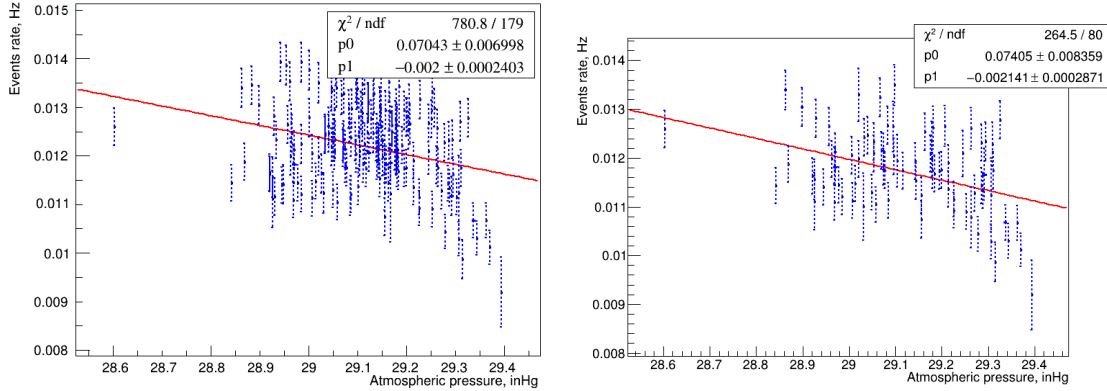


**Figure 6.7:** Rates of nLi + nLi events vs atmospheric pressure. Left: RxOn and RxOff periods. Right: RxOff only.

the exponential fits vary from  $(-0.53 \pm 0.01) \text{ \%/mbar}$  to  $(-0.80 \pm 0.02) \text{ \%/mbar}$  for neutrons and are substantially different for muons having only  $-0.16 \text{ \%/mbar}$ .

## 6.4 IBD Spectrum and Sterile Neutrino Oscillation Results

### 6.4.1 Spectrum Results

After subtraction of accidentals background and correlated cosmogenic background (scaled with exposure time and atmospheric pressure) a total number of  $50560 \pm 406$  IBD pairs have been detected during the experiment. The ratio of IBD signal to accidentals background constitutes 1.78, while the ratio to cosmogenic background is  $1.37^{18}$ .

Fig. 6.10 demonstrates the prompt spectrum  $E_{rec}$  of accidentals subtracted IBD-like signal. The spectrum during reactor-on periods shown in blue, while the spectrum during reactor-off - in red. Reactor-off spectrum was scaled with time exposure and atmospheric pressure to match exposure and atmospheric parameters during reactor-on. We can scale the spectrum during reactor-off, which is only our cosmogenic background, over the whole range because it is only intensity and not the spectrum features that is changing during different atmospheric conditions. Finally, the clear background subtracted IBD-like spectrum is shown in black.

There are two clear peaks that are seen in the spectra during both reactor-on and reactor-off periods.

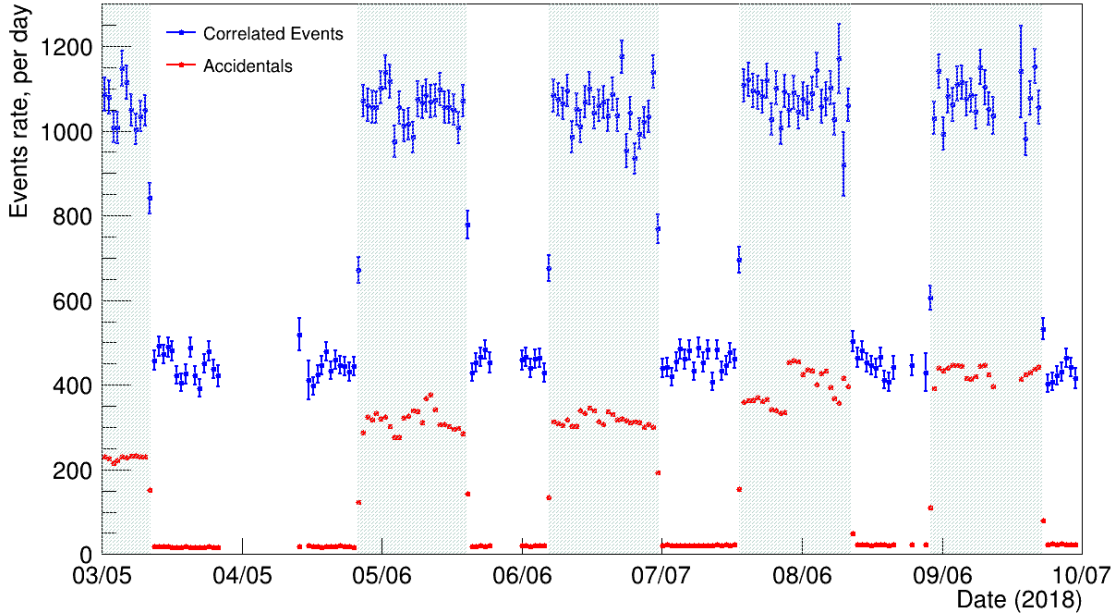


**Figure 6.8:** Rates of IBD-like events and accidentals with time. Each time bin is 24 hours.

- The first peak at 2.2 MeV is caused by multi-neutron shower mechanism, in which of the thermal neutrons is captured on  $^1\text{H}$ , which produces 2.224 MeV (deuterium binding energy) gamma, leaking into positron IBD-band. In coincidence, another neutron in this multi-shower event is captured on  $^6\text{Li}$ , accidentally matching the topology and time cuts, and therefore mimicking IBD-signal. The reverse in time coincidences of first neutron capture on  $^6\text{Li}$  and consequent neutron capture on  $^1\text{H}$  should also happen with the same frequency.
- The second peak around 4.4 MeV is caused by inelastic scattering of cosmogenic fast neutron on  $^{12}\text{C}$ . The carbon in this reaction reaches excited state  $^{12}\text{C}^*$  and emits a prompt 4.43 MeV gamma-ray. The scattered neutron meanwhile gets captured on  $^6\text{Li}$  in coincidence with the prompt event.

The shower veto helps to eliminate those types of IBD-background events but is not perfectly efficient. Finally, the continuum spectrum above 7 MeV without peaks comes as a mix of different high-energy neutrons related effects that include both neutron-proton elastic scattering, inelastic neutron scattering and also their combinations.

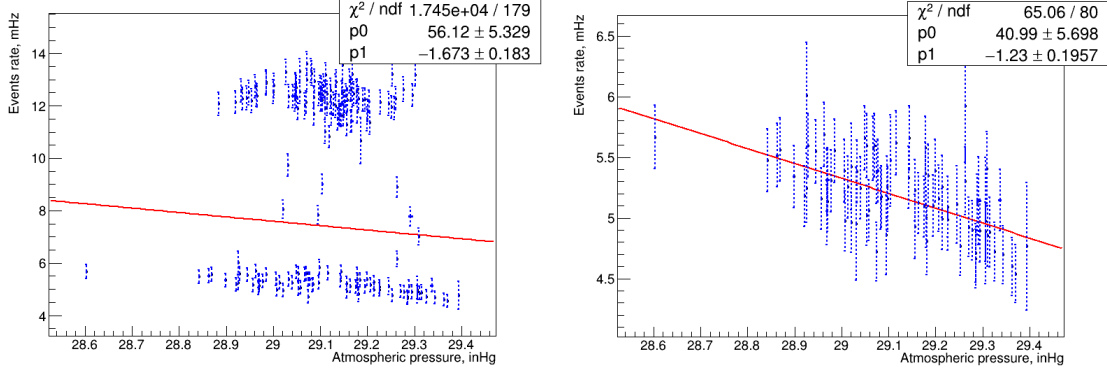


**Figure 6.9:** Rates of IBD-like events vs atmospheric pressure. Left: RxOn and RxOff periods. Right: RxOff only.

The subtracted IBD-signal matches our expectations of a spectrum of reactor electron antineutrinos, detected through IBD: we can see continuous distribution from 0 to 7 MeV, with a wide peak around 2.3-2.5 MeV. The peaks at 2.2 and 4.6 MeV are absent, which indicates a clear background subtraction. Another indication of proper scaling is the subtraction of a background above 7 MeV, in a 7-12 MeV region subtraction IBD-like backgrounds to approximately zero, because IBD signal in this region is minimal.

To reach one of the initial goals of the experiment, a comparison of the measured spectrum to the Huber model has been made. Two small deviations were observed around 2.5 MeV and 5 MeV energies. To compare in the interesting region between 4 to 6 MeV with the excess of events, found by the other experiments, a following procedure has been made: a Gaussian peak was added in this region to the true neutrino energy in theoretical prediction. The parameters of Gaussian peak - the mean value of 5.678 MeV and sigma of 0.562 MeV were taken from the fitting of the unfolded Daya Bay spectrum<sup>6</sup>. A small distortion has been observed in this region. The analysis described in<sup>18</sup> showed that the data have disfavored the hypothesis that  $^{235}\text{U}$  is entirely responsible for the distortion at  $2.44\sigma$  CL, and the null hypothesis of no distortion has been disfavored at  $2.17\sigma$ .

## 6.4.2 Oscillation Results

The search for sterile neutrino oscillations in PROSPECT is performed through comparison of prompt  $E_{rec}$  spectra between different baselines. The segmented structure of the detector allows the

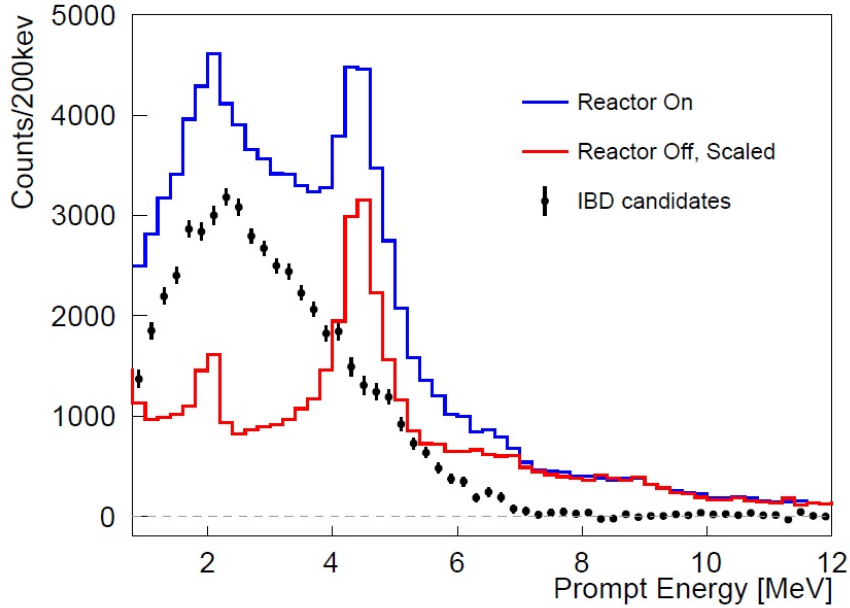


**Figure 6.10:** The observed prompt visible energy spectrum of IBD-like events (with subtracted accidentals) during reactor-on periods and during reactor-off periods. Reactor-off spectrum is scaled with time exposure and atmospheric pressure conditions to match the same parameters of reactor-on spectrum. The result of the subtraction, which is a final spectrum of IBD signal, is shown in black with only statistical errors<sup>18</sup>.

division of the fiducial segments into 10 baseline bins ( $l = 1, 2, \dots, 10$ ) depending on their distance from the reactor. The baseline bins assignment for the segments was chosen with the purpose of having approximately equal statistics in each baseline bin. Thus, each baseline bin has approximately 5000 IBD events in each baseline bin  $l$ , with per-bin relative variation of 10%.

The measured background-subtracted IBD signal prompt spectra  $E_{rec}$  in each baseline bin  $l$  ( $M_{l,e}$ ) is compared to the unoscillated spectrum that was Monte-Carlo generated with PG4 simulation package for that bin  $l$  ( $P_{l,e}$ ). PG4 spectrum is based on the best-fit detector response matrices for each segment applied to the predicted  $^{235}\text{U}$  electron antineutrino spectrum from Huber model<sup>55</sup> and the IBD cross-section measurement from<sup>48</sup>. Additional procedure to extract dependence of the oscillation results on the spectral shape and normalization uncertainty was to divide the spectrum in each baseline bin by the spectrum over the whole detector. Therefore the actual comparison of spectra between each baseline bin was relative and spectral shape independent.

The result of such comparison for PROSPECT results is shown in Fig. 6.12. Here, measured

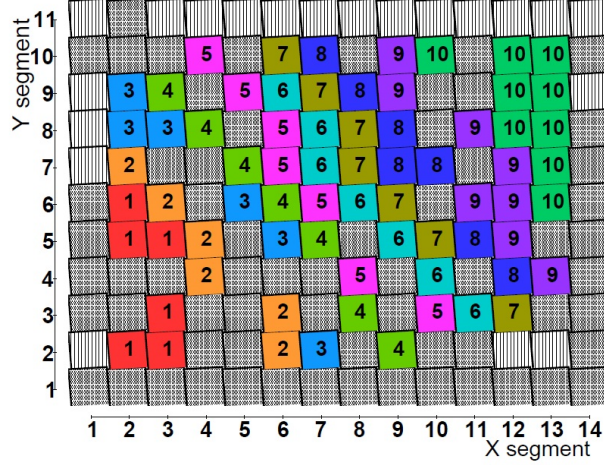


**Figure 6.11:** Assignment of baseline bins to the fiducial segments<sup>18</sup>.

spectra  $M_{l,e}$  are compared to the relative predicted spectra  $M_e \frac{P_{l,e}}{P_e}$ , where

$$M_e = \sum_{l=1}^{10} M_{l,e}, \quad P_e = \sum_{l=1}^{10} P_{l,e} \quad (6.13)$$

are total measured and predicted spectra, summed over all detector baselines. After the relativization, the relative spectra indicate only oscillations or the lack of thereof. Therefore, the relative measured spectra in Fig. 6.12 are compared not only with non-oscillated spectra (which gives flat unity value shown with dashed line) but also with oscillated predicted spectra ratios for best-fit point and RAA best-fit point. Visually, the plots do not represent any prominent indication of oscillated trends that would fit measured spectra more than flat unity.

To construct the exclusion contours for the possible oscillations of sterile neutrino, we need to quantitatively compare measured spectra  $M_{l,e}$  with theoretically predicted  $M_e \frac{P_{l,e}}{P_e}$ , when predicted spectrum is oscillated for the whole phase space of parameters of  $\sin^2 2\theta_{14}$  and  $\Delta m_{41}^2$ . For quantitative comparison, a  $\chi^2$  is defined as:

$$\chi^2 = \Delta^T V_{tot}^{-1} \Delta. \quad (6.14)$$

Here,  $\Delta$  is a 160-element vector (10 baselines bins  $l$  times 16 energy bins  $e$ ) which measures the

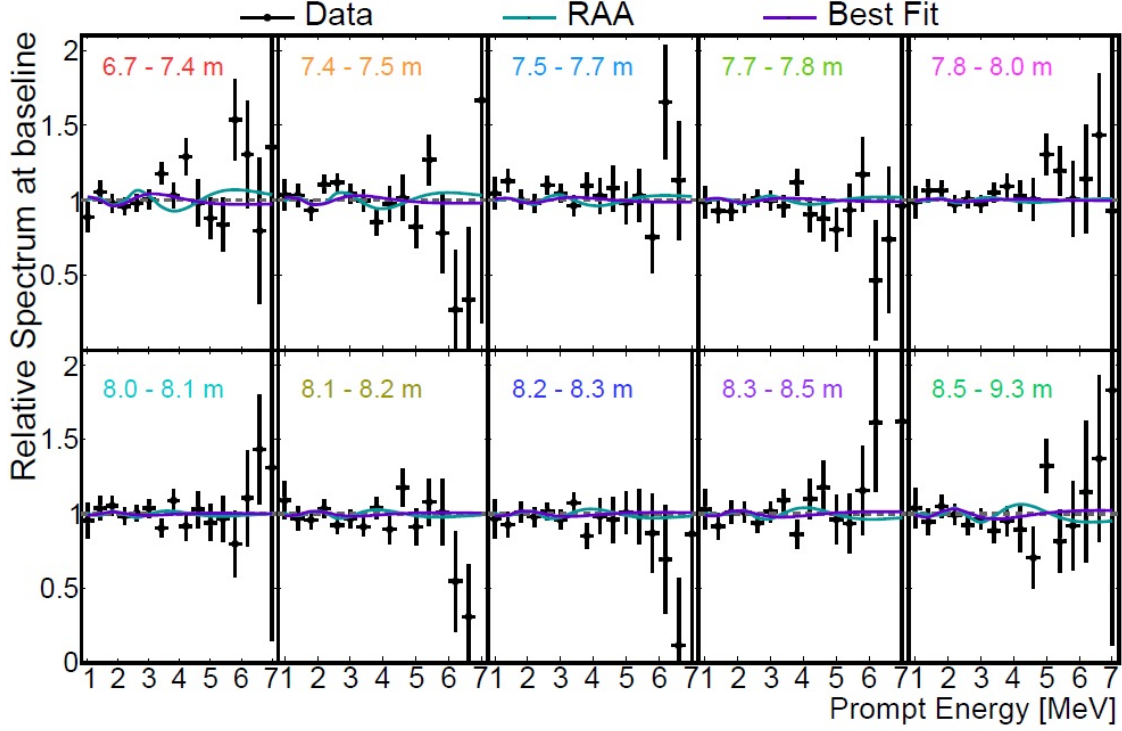


**Figure 6.12:** Comparison of the relative measured spectra of  $E_{rec} \frac{M_{l,e}}{M_e}$  with predicted  $\frac{P_{l,e}}{P_e}$  for different baseline bins. The predicted spectrum is oscillated for the best-fit point of  $(\sin^2 2\theta_{14}, \Delta m_{41}^2) = (0.11, 1.78 \text{ eV}^2)$  (purple solid lines) and for RAA best-fit point (blue solid lines) from<sup>19</sup>. Without oscillations, the ratio is a flat unity. Statistical uncertainties are shown with error bars<sup>18</sup>.

difference between measured and predicted spectra in each energy-baseline bin:

$$\Delta_{l,e} = M_{l,e} - M_e \frac{P_{l,e}}{P_e}. \quad (6.15)$$

$V_{tot}$  is a covariance matrix that represents the statistical and systematic uncertainties and their correlation with each other between energy bins.  $V_{tot}$  is a sum of the systematic and statistical matrices  $V_{sys}$  and  $V_{stat}$ .

The oscillation parameter space map for  $\chi^2$  values is presented in Fig. 6.13. In this map,  $\chi^2$  values are calculated and plotted along z-axis for each set of parameters of  $\sin^2 2\theta_{14}$  and  $\Delta m_{41}^2$ . The exclusion contours of 95% confidence level are obtained using critical parameters of  $\chi_{crit}^2$  from Feldman-Cousin approach (shown in black) and CLs approach (shown in red). The colored green

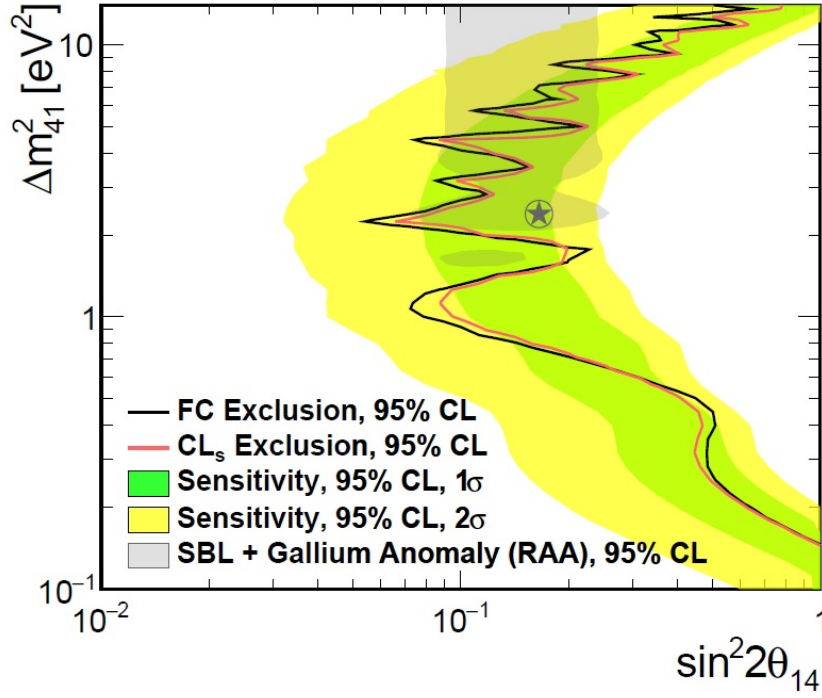


**Figure 6.13:** Exclusion contours for oscillations of sterile neutrino for Feldman-Cousins (black) and Gaussian CLs (red) methods. Green and yellow belts are the PROSPECT exclusion ranges from the toy MC datasets, grey belt is the RAA and best-fit point from<sup>20</sup> and preferred parameter space<sup>18</sup>.

and yellow bands show the PROSPECT 95% CL sensitivity regions. Those sensitivity regions mean that for each  $\Delta m_{41}^2$  value, this specific range of  $\sin^2 2\theta_{14}$  values has 95% CL exclusion boundary for unoscillated toy MC datasets. Specifically, green and yellow ranges include  $1\sigma$  and  $2\sigma$  (correspondingly) part of all MC toys of 95% CL exclusion boundaries.

As shown from the plot, the PROSPECT data excludes a significant part of the RAA allowed region, shown in grey, and the exclusion curves from both Feldman-Cousins and CLs methods show a good agreement. This exclusion region is located mostly within the green  $1\sigma$  belt, which indicates that the obtained spectral results are in a good correspondence with those expected from statistical and systematic variations.

## Chapter 7: Seasonality Study of Muons

### 7.1 Introduction

Muon cosmic rates are created in atmosphere due to interaction of primary cosmic rays (protons) with air molecules. As a result, neutrons, pions, kaons, muons, electrons, and photons are created. Muons are created through the decay of either pions or kaons.

$$\pi^- \rightarrow \mu^- + \bar{\nu}_\mu, \quad K^- \rightarrow \mu^- + \bar{\nu}_\mu \quad (7.1)$$

Secondary cosmic ray flux depends on the atmospheric pressure and temperature effects. While atmospheric pressure effect is discussed separately for different types of secondary events in Chapter, temperature effect is most prominent in muon rates observed on Earth.

There are two ways in which temperature of the atmosphere affects the count rate of muons on the surface. Positive effect shows increase of rate with increasing temperature. Negative effect, in contrast, shows decrease of rate with increase of temperature.

Positive effect happens because at higher temperatures the pions absorption with atmosphere decreases, and therefore at higher temperatures more muons are generated in the process of pion decay. Negative effect happens because with the expansion of the atmosphere in the summer, the majority of muons are generated at higher altitude and therefore they need to travel along the longer path to reach the ground. During this travel, they have a higher chance of decay into other particles, and the rate at the ground will be lower.

According to R. R. S. de Mendonca, et al.<sup>21</sup>, positive effect is prevalent for high energy muons, and negative effect dominates in low energy muons. The dependence of the rates of ground muon detectors on the season results in the harmonic periodic behavior with the maximum value in winter. De Mendoca et al. considered data of four ground muon detectors in Nagoya (Japan), Kuwait City (Kuwait), Kingston (Australia), and Sao-Martinho de Serra (Brazil). They analyzed balloon data

near the locations of these experiments. They found that temperature at mass muon production (MMP) altitude, where the maximum production of secondary cosmic rays happens, has the opposite behavior comparing to ground temperature with increase in winter, and decrease in summer (Fig. 7.1). The same behavior is shown by temperature at MMP line defined at isobar line along 100 hPa (atmospheric pressure level of MMP, Fig. 7.2). This means that because of this inverted temperature at MMP altitude, both negative and positive temperature effects incline for increase of muon events in the winter over the summer with harmonic behavior.

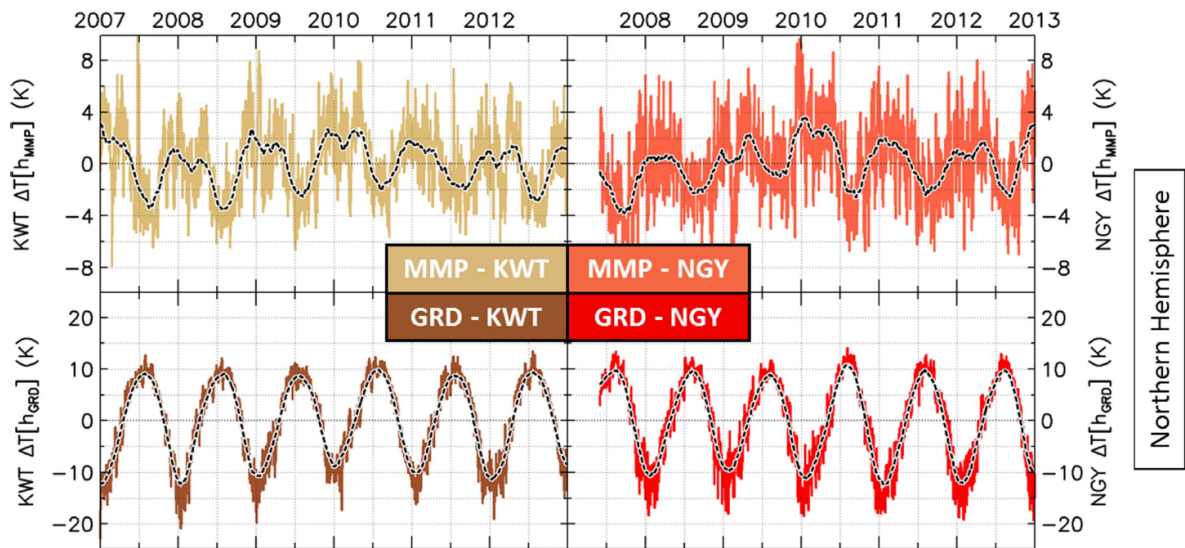


**Figure 7.1:** Dependence of temperature deviations from the mean value at the locations of Nagoya ground muon detector in Japan, and at the Kuwait City ground muon detector in Kuwait. Top plots show temperature deviations in the regions close to maximum muon production altitude ( $\Delta T[h_{MMP} = 16.5 \text{ km}]$ ) and bottom plots show temperature deviation near the ground ( $\Delta T[h_{GRD} = 0.5 \text{ km}]$ ). The black dashed curves are 3 months-average, and the colored curved are daily data.<sup>21</sup>

It is important to note, that the following inverted behavior, according to de Mendoca et al.<sup>21</sup> is only relevant for latitudes  $< 40^\circ$ . Respectively, the latitudes of the detectors in Nagoya, Kuwait, Kingston, and Sao Marthinho de Serra are at  $35.2^\circ\text{N}$ ,  $29.4^\circ\text{N}$ ,  $35.3^\circ\text{S}$ ,  $29.5^\circ\text{S}$ . Location of PROSPECT detector in Oak Ridge, Tennessee is at  $36.0^\circ\text{N}$ , which should also follow the following behavior. The behavior of temperature at  $h_{MMP}$  for experiments like Ice Cube ( $90.0^\circ\text{S}$ ) or Uragan muon detector ( $55.4^\circ\text{N}$ ) at high south/north latitudes would be in phase with temperature at  $h_{GRD}$ , and therefore

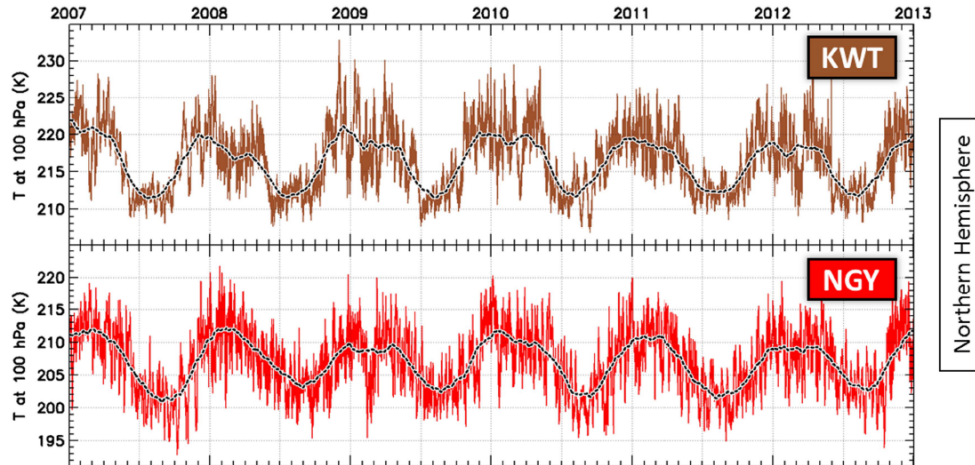


**Figure 7.2:** Dependence of temperature at isobar pressure of 100 hPa line (level of maximum muon production).<sup>21</sup>

the results would they both be ground detectors, would be different, too.

## 7.2 Muons Dependence on Atmospheric Pressure

Fig. 7.3 shows the dependence of muons rate on atmospheric pressure during the total timeline of PROSPECT data taking. We can see that it clearly depends on the atmospheric pressure but that there is also the trend of the data points being spread around which is caused by the temperature dependence.

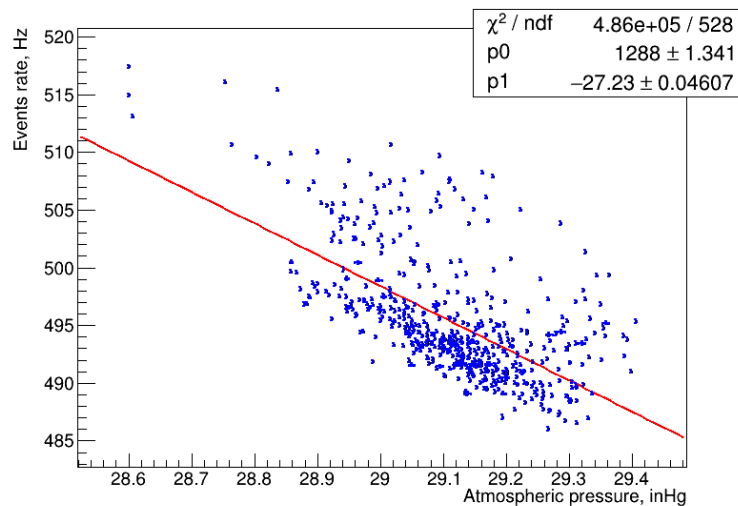


**Figure 7.3:** Rates of muon-like singles vs atmospheric pressure for combined RxOn and RxOff periods.

## 7.3 Temperature Datasets

### 7.3.1 Source of temperature data

Modified effective and mass-weighted temperatures, described above, were calculated based on Integrated Global Radiosonde Archive (IGRA) data from National Centers for Environmental Information (NCEI, National Oceanic and Atmospheric Administration, NOAA)<sup>90</sup>. IGRA archive has published data from over 2,700 stations around the world. The station closest to Oak Ridge was found to be a station in Nashville/Old Hickory (code of the station: USM00072327, 182 m above sea level) that has data from 1937 to 2020. The station in Knoxville, that would be closer, operated only from 1927 to 1973 and does not have data for PROSPECT dataset.

The Nashville station is one of 92 stations of National Weather Service (NWS) stations, and one of almost 900 global stations that perform a program of launching a weather balloon with radiosonde into the atmosphere. NWS station in Nashville launched balloon (Fig. 7.4) two times a day at 6 am and 6 pm (0:00 and 12:00 UTC). During the season of tropical cyclones, severe weather, and some other events, the balloon is launched four times a day, but extra launch points were removed for consistency of data.



**Figure 7.4:** National Weather Service station in Nashville (left) and a balloon inside before launching (right)<sup>22</sup>

The balloon is equipped with temperature and humidity sensor, Global Positioning System re-

ceiver to measure wind speed and direction, and radio transmitter to send the data to the station in real time. The balloon takes measurements of time after launch, pressure, height, temperature, humidity, dewpoint, wind direction, and wind speed at different altitudes from ground altitude up to approximately 36,000 - 37,000 m, but due to uniform altitude it reaches, we only considered data up to 10,000 mbar, after analysis.

### 7.3.2 Validity of Results in Nashville

To validate the assumption that the distance between Nashville, where the balloon is launched and the measurements at HFIR near Oak Ridge, does not affect temperature measurements too much, the comparison of ground temperatures is shown in Fig. 7.5. Oak Ridge measurements are taken from Oak Ridge Reservation Meteorology station which takes ground temperature measurements right near HFIR.

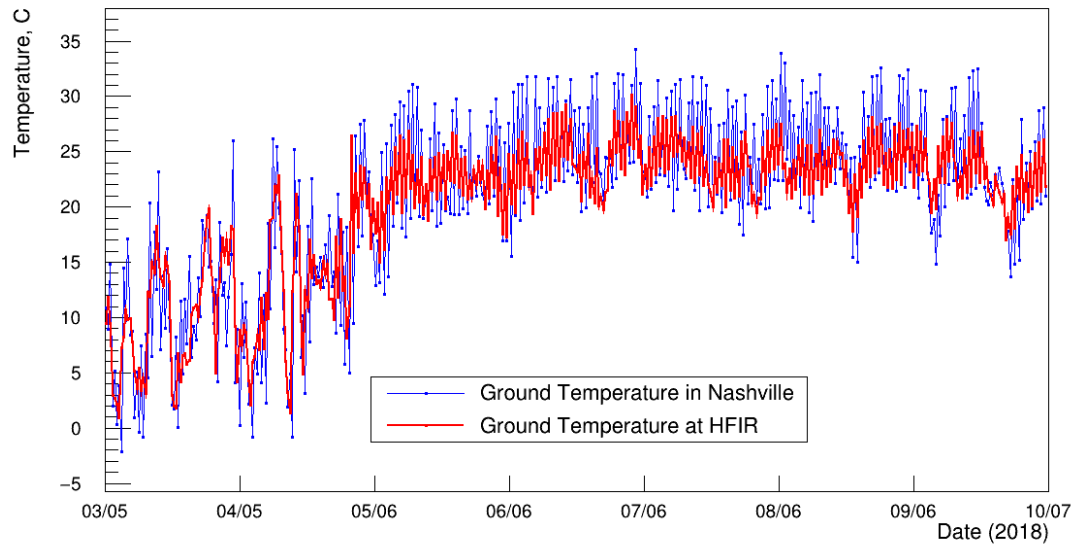


**Figure 7.5:** Comparison between ground temperatures at the balloon station in Nashville and near HFIR at Oak Ridge

To estimate uncertainty on temperature measurements, the conservative systematic uncertainty was chosen based on comparison of balloon data measurements between Nashville and other two closest to Oak Ridge sites with balloon launches: Peachtree City and Blacksburg. The details are

discussed in Appendix.

### 7.3.3 Comparison of Ground and MMP Temperatures

As was mentioned in Section 7.1, De Mendoca et al.<sup>21</sup> saw an anti-phase in temperatures on the ground and at maximum muon production (MMP) level. To check this fact, the ground ( $h = 180 \text{ m}$ ) and MMP ( $pressure = 100 \text{ hPa}$ , approximately 16.5 km) temperatures are compared in Fig. 7.6. We can see, that while the ground temperature (shown in blue) is increasing during the spring and summer, the temperature at MMP level (shown in red) had decreasing trend over time.

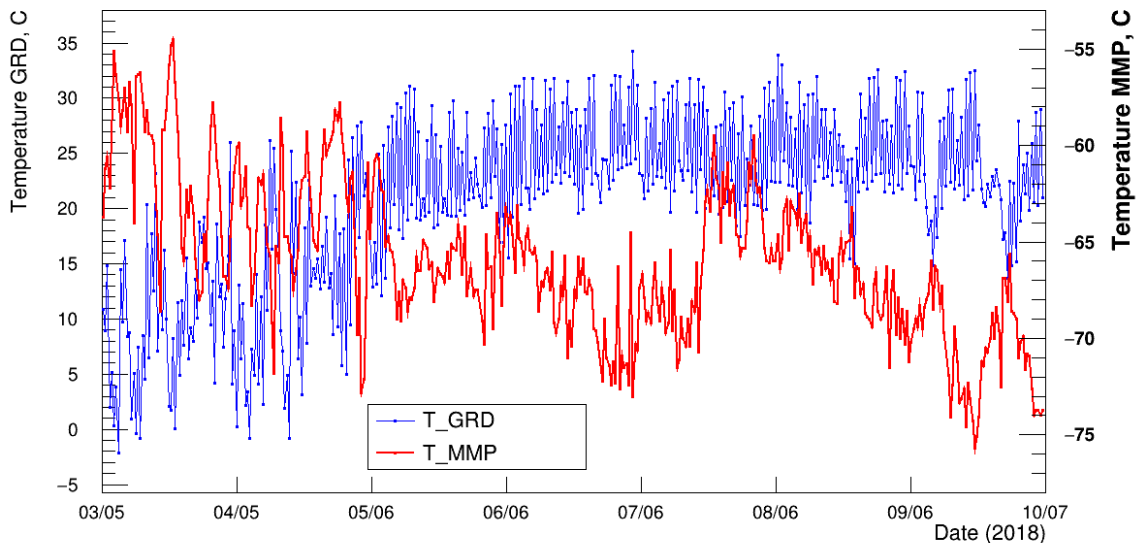


**Figure 7.6:** Comparison of ground and MMP temperatures at station in Nashville at Pressure = 100 hPa.

### 7.3.4 Modified Effective Temperature Calculation

For finding seasonal variations of muons, underground experiments look for the dependence of muon rates on the effective temperature ( $T_{EFF}$ ).  $T_{EFF}$  takes into account the whole atmospheric temperature profile, and is calculated with the following formula

$$T_{EFF} = \frac{\int_0^{x_{GRD}} \omega[x] \cdot T[x] \cdot dx}{\int_0^{x_{GRD}} \omega[x] \cdot dx}, \quad \omega[x] = \frac{1}{x} \cdot (e^{-x/\lambda_\pi} - e^{-x/\lambda_n}) \quad (7.2)$$

Here,  $\omega$  - weight function that describes pion and nucleon absorption in the atmosphere, and  $\lambda_\pi = 160 \text{ g/cm}^2$ ,  $\lambda_n = 120 \text{ g/cm}^2$  - attenuation lengths for pions and for nucleons.

Therefore, the difference in the intensity of muon rates ( $\Delta I_T$ ), depends on the difference in temperature of the atmosphere ( $\Delta T_{EFF}$ ) with linear with coefficient  $\alpha_{EFF}$ :

$$\Delta I_T = \alpha_{EFF} \cdot \Delta T_{EFF} \quad (7.3)$$

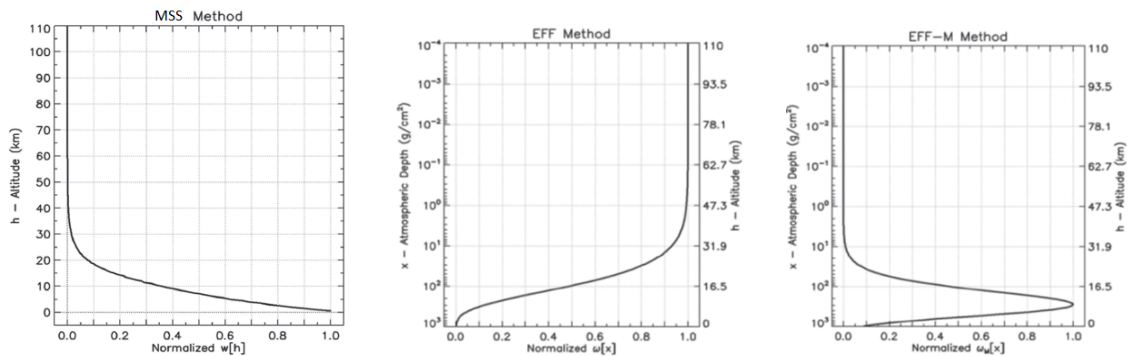


**Figure 7.7:** Left: Air mass weight function ( $w[ht]$ ) for mass-weighted method. Middle: weight function ( $\omega[x]$ ) of the effective temperature method vs atmospheric depth. Right: weight function ( $\omega[x]$ ) of the modified effective temperature method vs atmospheric depth.<sup>21</sup>

Fig. 7.7 (left) shows that the effective weight function  $\omega[x]$  has the most significant values for altitudes above 30 km.

However, de Mendoca, et. al<sup>21</sup> showed that the modified temperature model works worse for ground detectors than its modified version  $T_{EFF-M}$ . In modified effective temperature model, the temperature is calculated via the formula:

$$T_{EFF-M} = \frac{\int_0^{x_{GRD}} \omega_M[x] \cdot T[x] \cdot dx}{\int_0^{x_{GRD}} \omega_M[x] \cdot dx}, \quad \omega_M[x] = x \cdot (e^{-x/\lambda_\pi} - e^{-x/\lambda_n}) \quad (7.4)$$

As can be seen in Fig. 7.7 (right)  $\omega_M$  has more weight for temperatures measured at altitudes between 5 and 16.5 km, which also would work better for our source of temperature data, because the balloon usually goes up to altitudes of 34 km at most.

Considering, that we have data at discrete pressure levels, we can rewrite modified effective

temperature as:

$$T_{EFF-M} = \frac{\sum_0^{x_{GRD}} \omega_M[x] \cdot T[x] \cdot dx}{\sum_0^{x_{GRD}} \omega_M[x] \cdot dx}, \quad \omega_M[x] = x \cdot (e^{-x/\lambda_\pi} - e^{-x/\lambda_n}) \quad (7.5)$$

The balloon naturally does not reach the same data point in its flight. The altitude of its flight for PROSPECT dataset range from 5,622 m to 36,502 m, with the majority of datapoints exceed altitude of at least 24,000 m. To get consistent results, a cutoff value was chosen at pressure 2,000 Pa, and the details and discussion of this procedure is discussed in Appendix B.

The resulting values of  $T_{EFF-M}$  are presented in Fig. 7.8. It is well seen that diurnal variation, specific for ground temperature dataset  $T_{GRD}$  is not seen here, which shows that it is better atmospheric temperature characterization, than ground temperature.

### 7.3.5 Mass Weighted Temperatures Calculation

Mass weighted temperature is another method to include the whole atmosphere temperature profile. De Mendoca et al.<sup>21</sup> found that the muon detector rates have the best correlation with mass weighted temperature profile. The mass weighted temperature  $T_{MSS}$  is calculated with the following formula:

$$T_{MSS} = \sum_{i=0}^n w[h_i] \cdot T[h_i], \quad w[h_i] = \frac{x[h_i] - x[h_{i+1}]}{x[h_0]} \quad (7.6)$$

where  $h_0$  is the closest to the ground altitude,  $h_n$  - the altitude, closest to the top of atmosphere,  $x$  - atmospheric depth,  $x[h_{n+1}] = 0$ ,  $w[ht]$  - the air mass weighted function that behaves similar to atmospheric depth - the maximum value is near the ground, that is exponentially decreases with altitude. The dependence of  $w[ht]$  on altitude is shown in Fig. 7.7 (left). Therefore, the dependence of muon intensity rate ( $\Delta I_T$ ) on temperature  $T_{MSS}$  is defined through linear coefficient  $\alpha_{MSS}$ :

$$\Delta I_T = \alpha_{MSS} \cdot \Delta T_{MSS} \quad (7.7)$$

The altitude cutoff value for the balloon flights was the same as for  $T_{EFF-M}$  dataset, and is discussed in Appendix. The  $T_{MSS}$  temperature dataset for PROSPECT data taking period is shown

in Fig. 7.8. Similar to modified effective temperature dataset, mass weighted temperature also does not show diurnal variation.

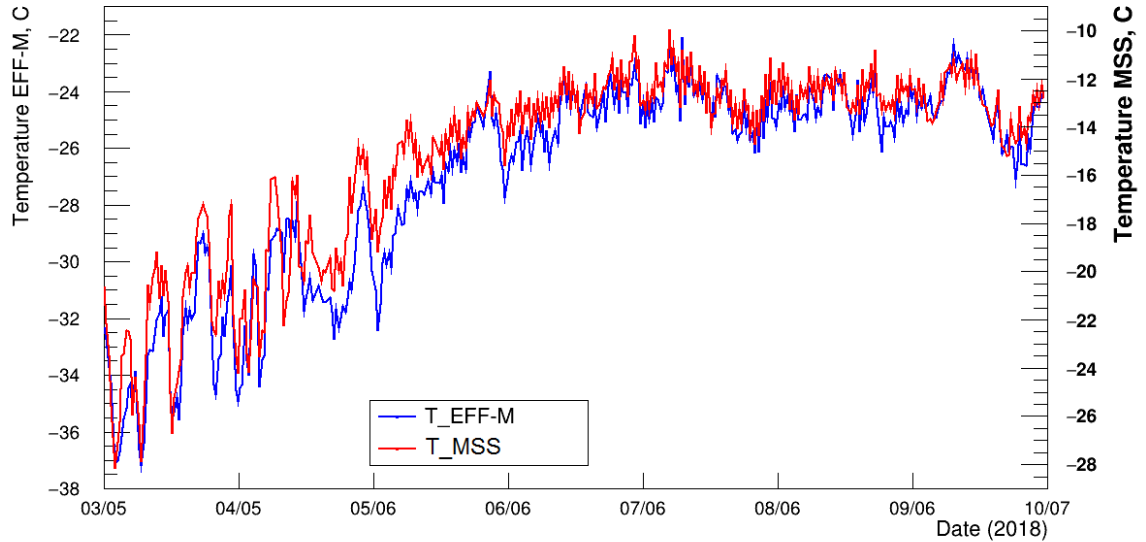


**Figure 7.8:** Modified effective ( $T_{EFF-M}$ ) and mass weighted ( $T_{MSS}$ ) temperatures at Nashville for PROSPECT data taking period.

## 7.4 Rate of Muons-like Events vs Temperature

### 7.4.1 Correlation Coefficients

The selection of muon-like events was used the same, as for muon shower veto: any cluster with  $E > 15\text{MeV}$ . As the cut depends only on energies and is very wide, this is not a clear sample of muons. Comparison of total rate of those events with time with  $T_{MSS}$  is shown in Fig. 7.9. The events were also separated in energy bins to study if the behavior with the temperature is consistent across all energy bins. It was found, that the energies with deposited energy beneath 200 MeV show anticorrelation with the mass-weighted temperature, while events with deposited energy of 250 MeV and above have steady increase with time. The energy bin of deposited energies between 200 and 250 MeV shows mixed behavior of upward and downward trend, resulting in approximately flat behavior over time.

The Table 7.1 shows the dependence of finer energy bins on mass weighted, modified effective,

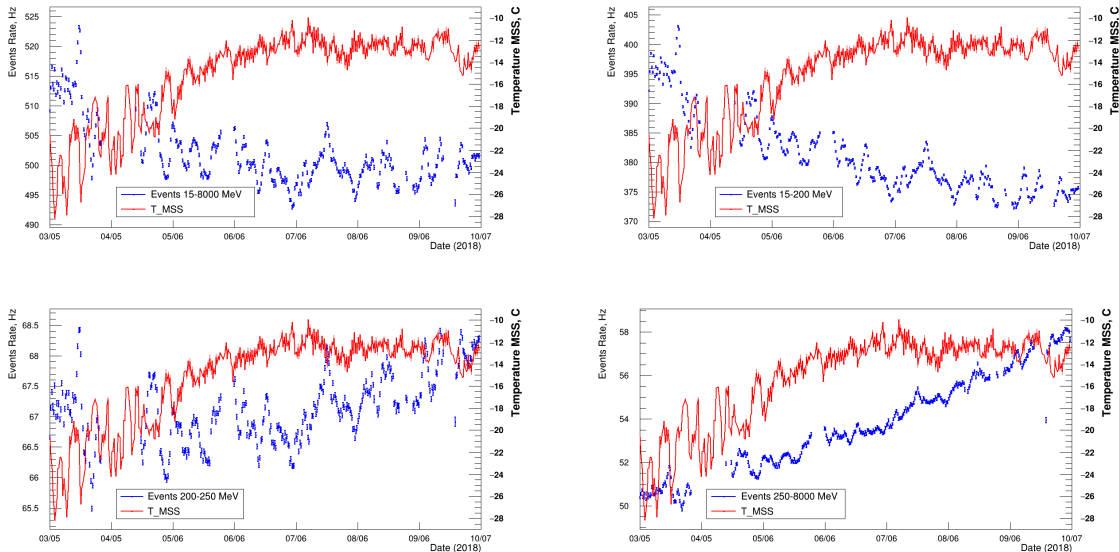


**Figure 7.9:** Rates for muon-like events for all events in the muon-like cut, and for energy ranges 15-200 MeV, 200-250 MeV, and 250-800 MeV, all compared to  $T_{MSS}$ .

ground at Nashville and HFIR, and at MMP level temperatures. It is clear seen that the dependence is negative for all temperatures except  $T_{MMP}$  below energy of 200 MeV, and it flips to positive dependence at energies 200-250 MeV. At the same time, for  $T_{MMP}$  the situation is reverse: the low energies have positive dependence, and it flips to negative in the same energy range 200-250 MeV.

**Table 7.1:** Correlation coefficients for different temperature datates and different energy bins of deposited energy of muon-like events in PROSPECT detector.

Energy, MeV	15	70	150	200	250	300	350	400	450
	-	-	-	-	-	-	-	-	-
	70	150	200	250	300	350	400	450	8000
$T_{MSS}$	-0.865	-0.882	-0.871	0.069	0.636	0.696	0.729	0.754	0.754
$T_{EFF-M}$	-0.862	-0.881	-0.866	0.156	0.697	0.749	0.777	0.795	0.802
$T_{GRD}$ Nashville	-0.664	-0.683	-0.679	-0.019	0.441	0.491	0.518	0.535	0.544
$T_{GRD}$ HFIR	-0.764	-0.784	-0.777	-0.005	0.519	0.578	0.609	0.627	0.632
$T_{MMP}$	+0.701	+0.701	+0.701	-0.009	-0.492	-0.549	-0.578	-0.589	-0.589

## 7.4.2 Linear Scaling with Pressure and Temperature

Obtained rates of muon-like events were scaled with atmospheric pressure and  $T_{MSS}$ . Fig. 7.10 shows scaling of muon-like events with deposited energy of 15-200 MeV with atmospheric pressure, and with temperature.

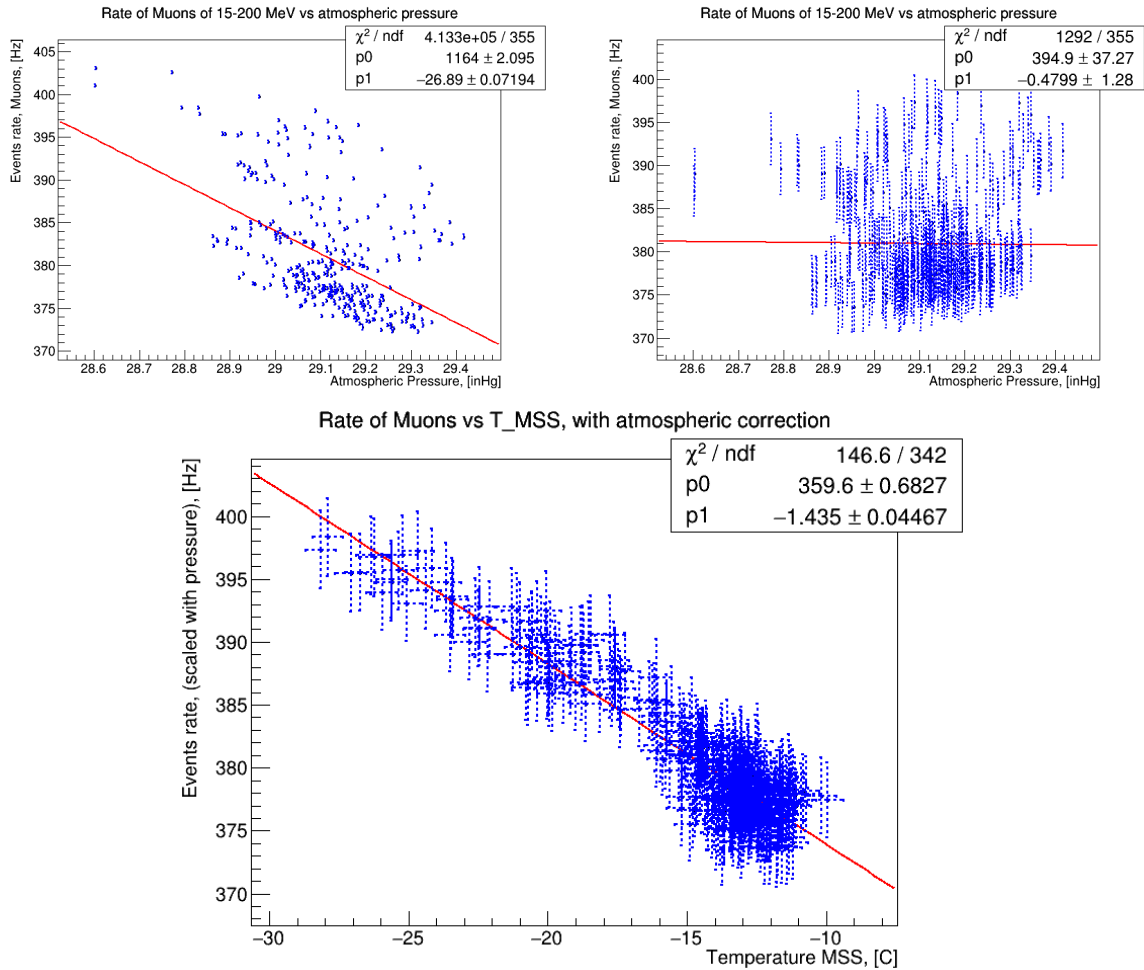


**Figure 7.10:** Top: Rates for muon-like events vs atmospheric pressure, before scaling with pressure, and after scaling. Bottom: Rates of muon-like events, already scaled with atmospheric pressure, vs  $T_{MSS}$ .

Muon-like events with deposited energy of 250-8000 MeV were only scaled with temperature, since the trend over time dominated the atmospheric pressure variations. The result is shown in Fig. 7.11.

The linear coefficients of total rates of muon-like events (15-8000 MeV), before and after pressure correction, vs  $T_{MSS}$  are compared to coefficients, obtained in<sup>21</sup>, and shown in Table 7.2.

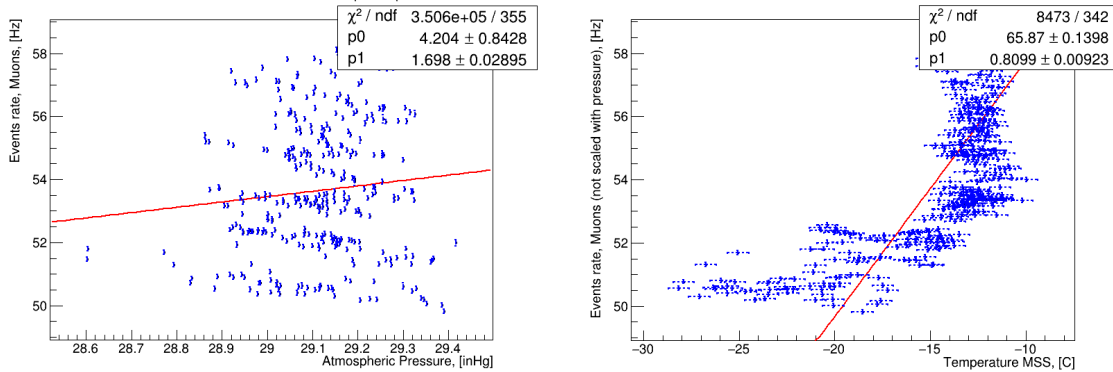


**Figure 7.11:** Behavior of muon-like events with high deposited energy (250-8000 MeV) vs atmospheric pressure (left) and vs  $T_{MSS}$  (right).

**Table 7.2:** Correlation coefficients of different muons datasets with different temperature datasets.

	Before Pressure Correction	After Pressure Correction	Literature
$T_{EFF-M}$	-0.232 %/K	-0.215 %/K	-0.27 %/K
$T_{MSS}$	-0.226 %/K	-0.203 %/K	-0.26 %/K
$T_{GRDNashville}$	-0.093 %/K	-0.090 %/K	-0.16 %/K

### 7.4.3 Michel Electrons

Taking into account that the sample of muon-like events is not a clear sample of events and has in it a contamination with others particles, especially at lower energies, a sample of Michel's electrons was chosen to study as an extra tool to confirm the validity of the muon studies. Michel's electrons are born in the detector when a low-energy muon decays inside the detector thus creating an electron as a result of this decay. For the selection of the event, we can choose a coincidence tag, which would theoretically let us to get significantly more clearer sample of low-energy muons.

DAQ triggering configuration limits time resolution at a scale of a muon decay which is  $2.2 \mu\text{s}$ . In addition, the energy/position signature for incoming muon and Michel electrons is also limited, which does not allow us to product the very accurate result. However, the analysis method can still be used for verification of our muon analysis.

The muon identification tag consists of a primary event - stopped muon of low energy - and a resulting event - Michel electron after decay of muon inside the detector. The primary muons were selected as clusters with total energy of  $\geq 20$  MeV, that are located at top cells. The following

events were selected in  $20 \mu\text{s}$  subsequent time windows. The energy of consequent Michel electron is  $\geq 4 \text{ MeV}$ . The distance cut was chosen such that the distance between those two events is not higher than 100 mm along z-axis.

The time rate of Michel electrons compared to  $T_{MSS}$  is shown in Fig. 7.12. Fig. 7.13 shows the same rate after scaling with atmospheric pressure. The rate is compared with pressure on Fig. 7.14: left is before scaling with pressure, and right is after scaling. After scaling with pressure, I compared the rate with  $T_{MSS}$  and obtained relatively good linear temperature dependence, shown in Fig. 7.15. These results show that regardless relatively loose cut for muon-like candidates in the main study of muons in this chapter, the purer sample of low-energy muons exhibits similar behavior with temperature thus validating study above.

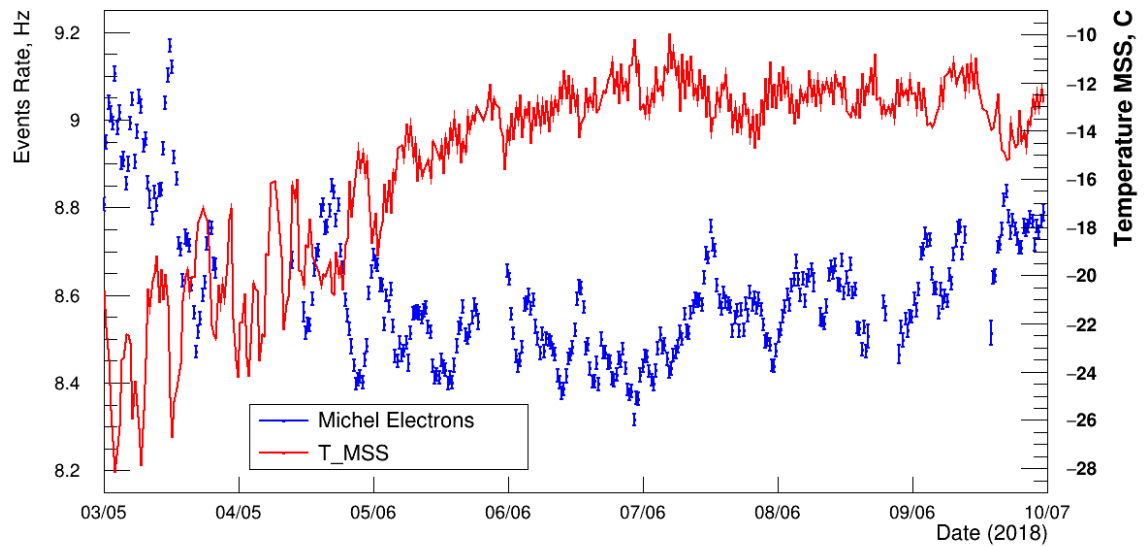


**Figure 7.12:** Rate of Michel electrons vs time, compared to  $T_{MSS}$ .

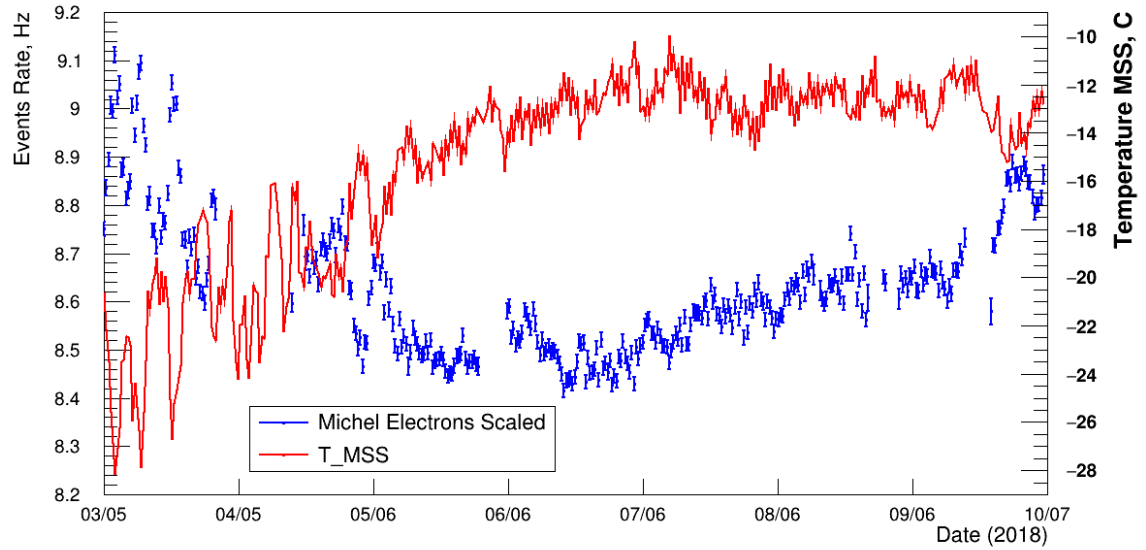


**Figure 7.13:** Rate of Michel electrons, already scaled with pressure vs time, compared to  $T_{MSS}$ .

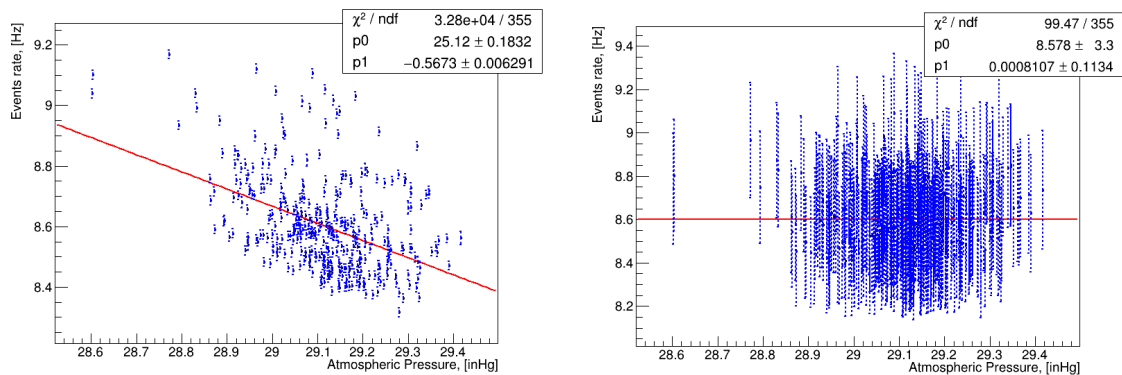


**Figure 7.14:** Dependence of rate of Michel electrons on atmospheric pressure before and after pressure scaling.

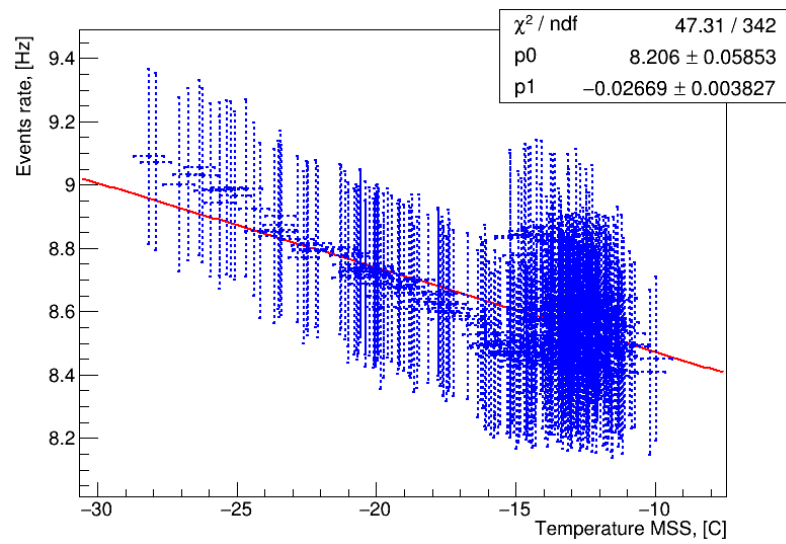


**Figure 7.15:** Dependence of scaled with pressure rate of Michel electrons on  $T_{MSS}$ .

## Chapter 8: Conclusion

PROSPECT is a reactor antineutrino experiment that was designed to study eV-scale sterile neutrino oscillations and to obtain a precise measurement of reactor antineutrino spectrum from  $^{235}\text{U}$  isotope at 85 MW High Flux Isotope Reactor at an average baseline distance of 7.9 m from the reactor core. The segmented design of array of  $11 \times 14$  segments with independent double-ended PMT readout allowed a reactor model independent search of sterile neutrino oscillations within the detector volume at baselines between 6.7 and 9.2 meters. The advantages of such a design also allowed to obtain a detection of propagation of antineutrino flux. PROSPECT performed measurements between March 2018 and October 2018 in Oak Ridge National Laboratory, in Tennessee, USA. During 96 days of its operation, PROSPECT detected  $50560 \pm 406$  IBD events which is the highest statistics of electron antineutrino spectrum of  $^{235}\text{U}$  spectrum up-to-date.

PROSPECT is a detector with almost no overburden, located on the surface in a very high proximity (7 m) to a nuclear reactor which inevitably lead to a high background. Regardless, the signal-to-background ratio, achieved by PROSPECT by the end of measurements, reached 1.4 which is the highest result of  $^{235}\text{U}$  electron antineutrino measurement up to date. Such a ratio was achieved due to multiple strategies, developed by the collaboration. First, the layered shielding structure made of different materials protects experiments from gamma-rays and thermalized neutrinos emitting by the reactor. The properties of inverse beta decay mechanism utilized for detection of neutrinos create a clear and distinct double tag for prompt and delayed signals in the detector allowing successfully reject the background. The cosmogenic shower veto procedure rejects the events that mimic IBD correlated pairs and come in correspondence with other cosmogenic events. The pulse shape discrimination properties of novel  $^6\text{Li}$ -loaded liquid scintillator allow creating framework to identify nuclear and electronic recoils to incorporate into more sophisticated series of cuts. Excellent energy resolution improves these cuts even further. Finally, the procedure of measuring the background during reactor-off periods, scaling it with atmospheric pressure and with time and subtracting from

reactor-on spectrum finalizes the obtaining a spectrum or reactor antineutrino signal.

This work investigated the dependence of cosmogenic background detected by on-surface experiment on atmospheric conditions including atmospheric pressure and temperature as well as dependence of background on the evolution of the detector. The results will allow the developing background rejection procedure in the future both for PROSPECT and other surface neutrino experiments.

## Bibliography

- [1] Masaharu Tanabashi, K Hagiwara, K Hikasa, Katsumasa Nakamura, Y Sumino, F Takahashi, J Tanaka, K Agashe, G Aielli, Claude Amsler, et al. Review of Particle Physics: particle data groups. 2018.
- [2] Francesco Capozzi, Eleonora Di Valentino, Eligio Lisi, Antonio Marrone, Alessandro Melchiorri, and Antonio Palazzo. Global constraints on absolute neutrino masses and their ordering. *Physical Review D*, 95(9):096014, 2017.
- [3] Courtesy to PROSPECT Collaboration, D. Norcini, 2018.
- [4] Frederick Reines, Clyde L Cowan Jr, FB Harrison, AD McGuire, and HW Kruse. Detection of the free antineutrino. *Physical Review*, 117(1):159, 1960.
- [5] Glenn R Jocher, Daniel A Bondy, Brian M Dobbs, Stephen T Dye, James A Georges III, John G Learned, Christopher L Mulliss, and Shawn Usman. Theoretical antineutrino detection, direction and ranging at long distances. *Physics Reports*, 527(3):131–204, 2013.
- [6] Feng Peng An, AB Balantekin, HR Band, M Bishai, S Blyth, D Cao, GF Cao, J Cao, WR Cen, YL Chan, et al. Improved measurement of the reactor antineutrino flux and spectrum at Daya Bay. *Chinese Physics C*, 41(1):013002, 2017.
- [7] J Ashenfelter, B Balantekin, CX Baldenegro, HR Band, G Barclay, CD Bass, D Berish, NS Bowden, CD Bryan, JJ Cherwinka, et al. Background radiation measurements at high power research reactors. *Nuclear Instruments and Methods in Physics Research Section A: Accelerators, Spectrometers, Detectors and Associated Equipment*, 806:401–419, 2016.
- [8] J Ashenfelter, AB Balantekin, C Baldenegro, HR Band, CD Bass, DE Bergeron, D Berish, LJ Bignell, NS Bowden, J Boyle, et al. The PROSPECT reactor antineutrino experiment. *Nuclear Instruments and Methods in Physics Research Section A: Accelerators, Spectrometers, Detectors and Associated Equipment*, 922:287–309, 2019.
- [9] J Ashenfelter, AB Balantekin, HR Band, CD Bass, DE Bergeron, D Berish, NS Bowden, JP Brodsky, CD Bryan, A Bykadorova Telles, et al. Performance of a segmented  ${}^6\text{Li}$ -loaded liquid scintillator detector for the PROSPECT experiment. *Journal of Instrumentation*, 13(06):P06023, 2018.
- [10] M Andriamirado, AB Balantekin, HR Band, CD Bass, DE Bergeron, D Berish, NS Bowden, JP Brodsky, CD Bryan, T Classen, et al. Improved short-baseline neutrino oscillation search and energy spectrum measurement with the PROSPECT experiment at HFIR. *Physical Review D*, 103(3):032001, 2021.
- [11] J Ashenfelter, AB Balantekin, C Baldenegro, HR Band, CD Bass, DE Bergeron, D Berish, LJ Bignell, NS Bowden, J Boyle, et al. The PROSPECT reactor antineutrino experiment. *Nuclear Instruments and Methods in Physics Research Section A: Accelerators, Spectrometers, Detectors and Associated Equipment*, 922:287–309, 2019.
- [12] Monthly and smoothed sunspot number, . URL <http://www.sidc.be/silso/monthlyssnplot>.
- [13] David Hathaway. Sunspots, grand solar minima, and climate change. URL <https://beta.capeia.com/planetary-science/2019/06/03/sunspots-grand-solar-minima-and-climate-change>.
- [14] Neutron Monitor Database NEST website. URL <http://www01.nmdb.eu/nest/>.

- [15] 2019 Let's Talk Science. What are cosmic rays? URL <https://letstalkscience.ca/educational-resources/backgrounders/what-are-cosmic-rays>.
- [16] Particle Data Group and others. Review of particle physics. *Chinese Physics C*, 40(10):100001, 2016.
- [17] Courtesy to PROSPECT Collaboration, G. Deichert and H. R. Band, 2020.
- [18] M Andriamirado, AB Balantekin, HR Band, CD Bass, DE Bergeron, D Berish, NS Bowden, JP Brodsky, CD Bryan, T Classen, et al. Improved Short-Baseline Neutrino Oscillation Search and Energy Spectrum Measurement with the PROSPECT Experiment at HFIR. *arXiv preprint arXiv:2006.11210*, 2020.
- [19] G Mention, M Fechner, Th Lasserre, Th A Mueller, D Lhuillier, M Cribier, and A Letourneau. Reactor antineutrino anomaly. *Physical Review D*, 83(7):073006, 2011.
- [20] Th A Mueller, D Lhuillier, Muriel Fallot, A Letourneau, S Cormon, M Fechner, Lydie Giot, Th Lasserre, J Martino, G Mention, et al. Improved predictions of reactor antineutrino spectra. *Physical Review C*, 83(5):054615, 2011.
- [21] RRS De Mendonça, CR Braga, E Echer, A Dal Lago, Kazuoki Munakata, T Kuwabara, Masayoshi Kozai, Chihiro Kato, M Rockenbach, NJ Schuch, et al. The temperature effect in secondary cosmic rays (muons) observed at the ground: analysis of the global muon detector network data. *The Astrophysical Journal*, 830(2):88, 2016.
- [22] <https://www.weather.gov/ohx/upperair>.
- [23] Wolfgang Pauli. Pauli letter collection: letter to Lise Meitner. Technical report, 1930.
- [24] Frederick Reines and Clyde L Cowan. The neutrino. *Nature*, 178(4531):446–449, 1956.
- [25] B Pontecorvo. Electron and muon neutrinos. *Zhur. Eksptl'. i Teoret. Fiz.*, 37, 1959.
- [26] Gaillard Danby, Jean Maurice Gaillard, Konstantin Goulianos, Leon M Lederman, N Mistry, M Schwartz, and J Steinberger. Observation of high-energy neutrino reactions and the existence of two kinds of neutrinos. *Physical Review Letters*, 9(1):36, 1962.
- [27] K Kodama, N Ushida, C Andreopoulos, N Saoulidou, G Tzanakos, P Yager, B Baller, D Boehnlein, Walter Freeman, B Lundberg, et al. Observation of tau neutrino interactions. *Physics Letters B*, 504(3):218–224, 2001.
- [28] B Pontecorvo. Inverse-process. *Chalk River Laboratory Report PD-205*, 1946.
- [29] Raymond Davis Jr, Don S Harmer, and Kenneth C Hoffman. Search for neutrinos from the Sun. *Physical Review Letters*, 20(21):1205, 1968.
- [30] John N Bahcall, Neta A Bahcall, and Giora Shaviv. Present Status of the Theoretical Predictions for the  $^{37}\text{Cl}$  Solar-Neutrino Experiment. *Physical Review Letters*, 20(21):1209, 1968.
- [31] Kohji S Hirata, Takaaki Kajita, T Kifune, K Kihara, Masayuki Nakahata, K Nakamura, S Ohara, Y Oyama, N Sato, M Takita, et al. Observation of  $^8\text{B}$  solar neutrinos in the Kamiokande-II detector. *Physical Review Letters*, 63(1):16, 1989.
- [32] Alain Bellerive, JR Klein, AB McDonald, AJ Noble, AWP Poon, SNO Collaboration, et al. The Sudbury Neutrino Observatory. *Nuclear Physics B*, 908:30–51, 2016.
- [33] KS Hirata, T Kajita, M Koshiba, M Nakahata, S Ohara, Y Oyama, N Sato, A Suzuki, M Takita, Y Totsuka, et al. Experimental study of the atmospheric neutrino flux. *Physics Letters B*, 205(2-3):416–420, 1988.

- [34] D Casper, R Becker-Szendy, CB Bratton, DR Cady, R Claus, ST Dye, W Gajewski, M Goldhaber, TJ Haines, PG Halverson, et al. Measurement of atmospheric neutrino composition with the IMB-3 detector. *Physical Review Letters*, 66(20):2561, 1991.
- [35] WWM Allison, GJ Alner, DS Ayres, WL Barrett, C Bode, PM Border, CB Brooks, JH Cobb, DJA Cockerill, RJ Cotton, et al. Measurement of the atmospheric neutrino flavour composition in Soudan 2. *Physics Letters B*, 391(3-4):491–500, 1997.
- [36] Bruno Pontecorvo. Mesonium and antimesonium. *Zhur. Eksptl'. i Teoret. Fiz.*, 33, 1957.
- [37] Ziro Maki, Masami Nakagawa, and Shoichi Sakata. Remarks on the unified model of elementary particles. *Progress of Theoretical Physics*, 28(5):870–880, 1962.
- [38] Bruno Pontecorvo. Neutrino experiments and the problem of conservation of leptonic charge. *Sov. Phys. JETP*, 26(984-988):165, 1968.
- [39] Carlo Giunti and Chung W Kim. *Fundamentals of neutrino physics and astrophysics*. Oxford university press, 2007.
- [40] Rabindra N Mohapatra and Goran Senjanović. Neutrino mass and spontaneous parity nonconservation. *Physical Review Letters*, 44(14):912, 1980.
- [41] A LSND. Aguilar et al., Evidence for neutrino oscillations from the observation of  $\nu_e$  appearance in a  $\nu_\mu$  beam. *Phys. Rev. D*, 64:112007, 2001.
- [42] B Karmen. Armbruster et al. *Phys. Rev. D*, 65:112001, 2002.
- [43] AA Aguilar-Arevalo, AO Bazarko, SJ Brice, BC Brown, L Bugel, J Cao, L Coney, JM Conrad, DC Cox, A Curioni, et al. Search for electron neutrino appearance at the  $\Delta m^2 \sim 1eV^2$  scale. *Physical review letters*, 98(23):231801, 2007.
- [44] AAea Aguilar-Arevalo, BC Brown, L Bugel, G Cheng, ED Church, JM Conrad, R Dharmapalan, Z Djurcic, DA Finley, R Ford, et al. Improved search for  $\nu_\mu \rightarrow \nu_e$  oscillations in the MiniBooNE experiment. *Physical review letters*, 110(16):161801, 2013.
- [45] W Hampel, G Heusser, J Kiko, T Kirsten, M Laubenstein, E Pernicka, W Rau, U Rönn, C Schlosser, M Wójcik, et al. Final results of the  $^{51}\text{Cr}$  neutrino source experiments in GALLEX. *Physics Letters B*, 420(1-2):114–126, 1998.
- [46] JN Abdurashitov. Measurement of the response of the Russian-American Gallium Experiment to neutrinos from a  $^{51}\text{Cr}$  source. *Phys. Rev. C*, 59(hep-ph/9803418):2246, 1999.
- [47] P. Vogel. Analysis of the antineutrino capture on protons. *Phys. Rev. D*, 29:1918–1922, May 1984. doi: 10.1103/PhysRevD.29.1918. URL <https://link.aps.org/doi/10.1103/PhysRevD.29.1918>.
- [48] P Vogel and John F Beacom. Angular distribution of neutron inverse beta decay,  $\bar{\nu}_e + p \rightarrow e^+ + n$ . *Physical Review D*, 60(5):053003, 1999.
- [49] BR Davis, P Vogel, FM Mann, and RE Schenter. Reactor antineutrino spectra and their application to antineutrino-induced reactions. *Physical Review C*, 19(6):2259, 1979.
- [50] Po Vogel, Go Ko Schenter, Fo Mo Mann, and RE Schenter. Reactor antineutrino spectra and their application to antineutrino-induced reactions. ii. *Physical Review C*, 24(4):1543, 1981.
- [51] F Von Feilitzsch, AA Hahn, and K Schreckenbach. Experimental beta-spectra from  $^{239}\text{Pu}$  and  $^{235}\text{U}$  thermal neutron fission products and their correlated antineutrino spectra. *Physics Letters B*, 118(1-3):162–166, 1982.

- [52] Nils Haag, Achim Guetlein, Martin Hofmann, L Oberauer, W Potzel, K Schreckenbach, and FM Wagner. Experimental determination of the antineutrino spectrum of the fission Products of  $^{238}\text{U}$ . *Physical review letters*, 112(12):122501, 2014.
- [53] Anna C Hayes and Petr Vogel. Reactor neutrino spectra. *Annual Review of Nuclear and Particle Science*, 66:219–244, 2016.
- [54] Xin Qian and Jen-Chieh Peng. Physics with reactor neutrinos. *Reports on Progress in Physics*, 82(3):036201, 2019.
- [55] Patrick Huber. Determination of antineutrino spectra from nuclear reactors. *Physical Review C*, 84(2):024617, 2011.
- [56] Y Abe, Christoph Aberle, T Akiri, JC Dos Anjos, F Ardellier, AF Barbosa, A Baxter, M Bergevin, A Bernstein, TJC Bezerra, et al. Indication of reactor  $\bar{\nu}_e$  disappearance in the Double Chooz experiment. *Physical Review Letters*, 108(13):131801, 2012.
- [57] FP An, JZ Bai, AB Balantekin, HR Band, D Beavis, W Beriguete, M Bishai, S Blyth, K Boddy, RL Brown, et al. Observation of electron-antineutrino disappearance at Daya Bay. *Physical Review Letters*, 108(17):171803, 2012.
- [58] Jung Keun Ahn, S Chebotaryov, JH Choi, S Choi, W Choi, Y Choi, HI Jang, JS Jang, EJ Jeon, IS Jeong, et al. Observation of reactor electron antineutrinos disappearance in the RENO experiment. *Physical Review Letters*, 108(19):191802, 2012.
- [59] Y. Abe et al. Reactor  $\bar{\nu}_e$  disappearance in the Double Chooz experiment. *Phys. Rev. D*, 86:052008, Sep 2012. doi: 10.1103/PhysRevD.86.052008. URL <https://link.aps.org/doi/10.1103/PhysRevD.86.052008>.
- [60] FP An, Q An, JZ Bai, AB Balantekin, HR Band, W Beriguete, M Bishai, S Blyth, RL Brown, GF Cao, et al. Improved measurement of electron antineutrino disappearance at Daya Bay. *Chinese Physics C*, 37(1):011001, 2013.
- [61] FP An, AB Balantekin, HR Band, W Beriguete, M Bishai, S Blyth, RL Brown, I Butorov, GF Cao, J Cao, et al. Spectral measurement of electron antineutrino oscillation amplitude and frequency at Daya Bay. *Physical review letters*, 112(6):061801, 2014.
- [62] Feng Peng An, AB Balantekin, HR Band, M Bishai, S Blyth, I Butorov, D Cao, GF Cao, J Cao, WR Cen, et al. Measurement of the reactor antineutrino flux and spectrum at Daya Bay. *Physical review letters*, 116(6):061801, 2016.
- [63] F. P. An et al. Evolution of the Reactor Antineutrino Flux and Spectrum at Daya Bay. *Phys. Rev. Lett.*, 118:251801, Jun 2017. doi: 10.1103/PhysRevLett.118.251801. URL <https://link.aps.org/doi/10.1103/PhysRevLett.118.251801>.
- [64] AC Hayes, JL Friar, GT Garvey, Gerard Jungman, and Guy Jonkmans. Systematic uncertainties in the analysis of the reactor neutrino anomaly. *Physical Review Letters*, 112(20):202501, 2014.
- [65] A Onillon. Updated Flux and Spectral Predictions relevant to the RAA. In *Applied Antineutrino Physics Workshop (AAP)*, 2018.
- [66] Kevork N Abazajian, MA Acero, SK Agarwalla, AA Aguilar-Arevalo, CH Albright, S Antusch, CA Argüelles, AB Balantekin, G Barenboim, V Barger, et al. Light sterile neutrinos: a white paper. *arXiv preprint arXiv:1204.5379*, 2012.
- [67] Seon-Hee Seo. New Results from RENO using 1500 Days of Data, 2017.

- [68] Y. Abe, J. C. dos Anjos, J. C. Barriere, E. Baussan, I. Bekman, M. Bergevin, T. J. C. Bezerra, L. Bezrukov, E. Blucher, and et al. Improved measurements of the neutrino mixing angle  $\theta_{13}$  with the Double Chooz detector. *Journal of High Energy Physics*, 2014(10), Oct 2014. ISSN 1029-8479. doi: 10.1007/jhep10(2014)086. URL [http://dx.doi.org/10.1007/JHEP10\(2014\)086](http://dx.doi.org/10.1007/JHEP10(2014)086).
- [69] J Ashenfelter, B Balantekin, HR Band, G Barclay, CD Bass, D Berish, NS Bowden, A Bowes, JP Brodsky, CD Bryan, et al. Light collection and pulse-shape discrimination in elongated scintillator cells for the PROSPECT reactor antineutrino experiment. *Journal of Instrumentation*, 10(11):P11004, 2015.
- [70] J Ashenfelter, AB Balantekin, HR Band, G Barclay, C Bass, NS Bowden, CD Bryan, JJ Cherwinka, R Chu, T Classen, et al. PROSPECT-A precision reactor oscillation and spectrum experiment at short baselines. *arXiv preprint arXiv:1309.7647*, 2013.
- [71] Danielle Norcini. First Search for eV-Scale Sterile Neutrinos and Precision Measurement of the  $^{235}\text{U}$  Antineutrino Spectrum with the PROSPECT Experiment, December 2019. URL [https://prospect.yale.edu/sites/default/files/norcini\\_final.pdf](https://prospect.yale.edu/sites/default/files/norcini_final.pdf).
- [72] J Ashenfelter, B Balantekin, CX Baldenegro, HR Band, G Barclay, CD Bass, D Berish, NS Bowden, CD Bryan, JJ Cherwinka, et al. Background radiation measurements at high power research reactors. *Nuclear Instruments and Methods in Physics Research Section A: Accelerators, Spectrometers, Detectors and Associated Equipment*, 806:401–419, 2016.
- [73] Thomas K Gaisser, Ralph Engel, and Elisa Resconi. *Cosmic rays and particle physics*. Cambridge University Press, 2016.
- [74] Cosmos - the sao encyclopedia of astronomy, . URL <https://astronomy.swin.edu.au/cosmos/S/Solar+Flare>.
- [75] Space weather news from april 17, 2018. URL <https://www.spaceweatherlive.com/en/news/view/338/20180417-coronal-hole-faces-earth>.
- [76] Goddard space flight center: Space physics data facility, website. URL <https://pwg.gsfc.nasa.gov/istp/nicky/cme-chase.html>.
- [77] List of GLE events in Neutron Monitor Database website. URL [http://www01.nmdb.eu/nest/gle\\_list.php](http://www01.nmdb.eu/nest/gle_list.php).
- [78] The Compact Cosmic Ray Telescope aboard the Kuiper Airborne Observatory website. URL <https://www2.lbl.gov/abc/cosmic/SKliewer/Index.htm>.
- [79] John M Clem and Lev I Dorman. Neutron monitor response functions. In *Cosmic Rays and Earth*, pages 335–359. Springer, 2000.
- [80] Cosmic Ray Station of the University of Oulu / Sodankyla Geophysical Observatory. URL <http://cosmicrays.oulu.fi/readme.html>.
- [81] JA Lockwood and HE Yingst. Correlation of meteorological parameters with cosmic-ray neutron intensities. *Physical Review*, 104(6):1718, 1956.
- [82] JA Simpson, W Fonger, and SB Treiman. Cosmic radiation intensity-time variations and their origin. i. neutron intensity variation method and meteorological factors. *Physical Review*, 90(5):934, 1953.
- [83] John R Davis, Erik Brubaker, and Kai Vetter. Fast neutron background characterization with the radiological multi-sensor analysis platform (radmap). *Nuclear Instruments and Methods in Physics Research Section A: Accelerators, Spectrometers, Detectors and Associated Equipment*, 858:106–112, 2017.

- [84] Douglas VanDerwerken, Marshall Millett, Thomas Wilson, Svetlana Avramov-Zamurovic, Martin Nelson, Kayla Barron, and Charles Leidig. Meteorologically driven neutron background prediction for homeland security. *IEEE Transactions on Nuclear Science*, 65(5):1187–1195, 2018.
- [85] Paul H Barrett, Lowell M Bollinger, Giuseppe Cocconi, Yehuda Eisenberg, and Kenneth Greisen. Interpretation of cosmic-ray measurements far underground. *Reviews of Modern Physics*, 24(3):133, 1952.
- [86] FP An, AB Balantekin, HR Band, M Bishai, S Blyth, D Cao, GF Cao, J Cao, YL Chan, JF Chang, et al. Seasonal variation of the underground cosmic muon flux observed at Daya Bay. *Journal of Cosmology and Astroparticle Physics*, 2018(01):001, 2018.
- [87] Courtesy to PROSPECT Collaboration, M. Mendenhall, 2018.
- [88] Courtesy to PROSPECT Collaboration, A. Woolverton, 2020.
- [89] <http://cosray.phys.uoa.gr/index.php/data/nm-barometric-coefficient>.
- [90] <https://www.ncdc.noaa.gov/data-access/weather-balloon/integrated-global-radiosonde-archive>.
- [91] B Wilczyńska, D Góra, P Homola, J Pe, M Risse, H Wilczyński, et al. Variation of atmospheric depth profile on different time scales. *Astroparticle Physics*, 25(2):106–117, 2006.
- [92] Juan Cruz Moreno and Sergio Sciutto. Characterization of the atmospheric depth profile using the ground-level temperature: The case of malargüe, argentina. *The European Physical Journal Plus*, 128(9):104, 2013.

## Appendix A: Spatial Distribution Study of Recoil-like Events

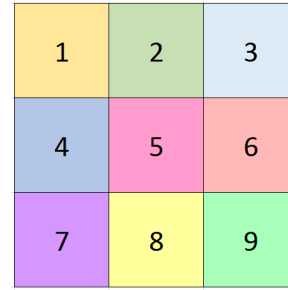
To better understand the problematic behavior of recoil-like singles, described in Section 4.2.2, I performed the following two studies. The studies were performed on prior PROSPECT dataset, so there are less excluded segments than discussed in the final plots in this thesis. However, the conclusion holds the same.

In the first study, the detector was separated into 9 parts with 14 segments in each part (Fig. A.1). Here, the region called "9" is located at the bottom of the detector, just below the "hot spot". The region called "7" is also at the bottom of the detector, but is directed toward the reactor. Energy/PSD distributions for one reactor-on run (1 hour) on May 15th were compared between those 9 regions, as shown in Fig. A.2. Those energy/PSD distributions do not have recoil cut on them to better see the situation. As we can see, there are extra amount of events appear on the bottom around  $PSD = 0.3$  and  $PSD = 0.4$ . There are also more of those extra events on the right side, than on the left side. This can be well explained with ingress theory, in which more false events happen at the bottom of the detector because more liquid leaks into the PMT housings due to higher pressure they experience at the bottom of the detector. At the same time, the PMT housings on the top of the detector experience less pressure, which leads to less leakage and less ingress. On the other hand, the right side has slightly more events comparing to the left side. This is happening because even though the reactor is closer to the left side of the detector, the right side has the less shielding at the bottom, producing increase in the background events just at the location where part "9" is located. The higher background create more false "recoil-like signals".

Very similar comparison was done for a run in March for reactor-off period, and similar behavior was observed. The less events happened to be leaked due to lower background activity and just the beginning of the functioning of the detector, but the spatial distribution of these leaked events also pointed towards their ingress nature.

In another study, the detector was divided into "Right" and "Left" parts, and "Top" and "Bot-

140	141	142	143	144	145	146	147	148	149	150	151	152	153
126	127	128	129	130	131	132	133	134	135	136	137	138	139
112	113	114	115	116	117	118	119	120	121	122	123	124	125
98	99	100	101	102	103	104	105	106	107	108	109	110	111
84	85	86	87	88	89	90	91	92	93	94	95	96	97
70	71	72	73	74	75	76	77	78	79	80	81	82	83
56	57	58	59	60	61	62	63	64	65	66	67	68	69
42	43	44	45	46	47	48	49	50	51	52	53	54	55
28	29	30	31	32	33	34	35	36	37	38	39	40	41
14	15	16	17	18	19	20	21	22	23	24	25	26	27
0	1	2	3	4	5	6	7	8	9	10	11	12	13



To Reactor

Hot Spot

**Figure A.1:** The dividing of the detector into 9 parts. Each part has 14 segments. Excluded segments are not colored.

tom” parts. The rates of recoil-like signals in these groups of segments were calculated and compared to atmospheric pressure, and correlation coefficients and  $\chi^2$  were calculated. The particular choices of these groups are:

- ”Left”: 16 segments on the left side of the detector throughout the whole height of the detector (Fig. A.3 (left), shown in yellow)
- ”Right”: 16 segments on the right side of the detector, chosen in a way such that number of detectors at each row matches the number of detectors at the same row on the ”left” side (Fig. A.3 (left), shown in green)
- ”Top 1”: the segments from the 2 top non-fiducial rows (Fig. A.3 (right)), 16 segments in total
- ”Top 2”: the segments from the 3 top non-fiducial rows, 26 segments in total
- ”Bottom”: the segments from the 3 bottom non-fiducial rows, 19 segments in total

Fig. A.4 and Fig. A.5 show the examples of rates scaling with pressure, and compared between each other. Fig. A.4 shows comparison between left and right parts for z-fiducial cut =  $\pm 434$  mm, and PSD  $\sigma$ -cut of  $3.5 \sigma$ . We can see, that while the left side is very well scaled with pressure, the

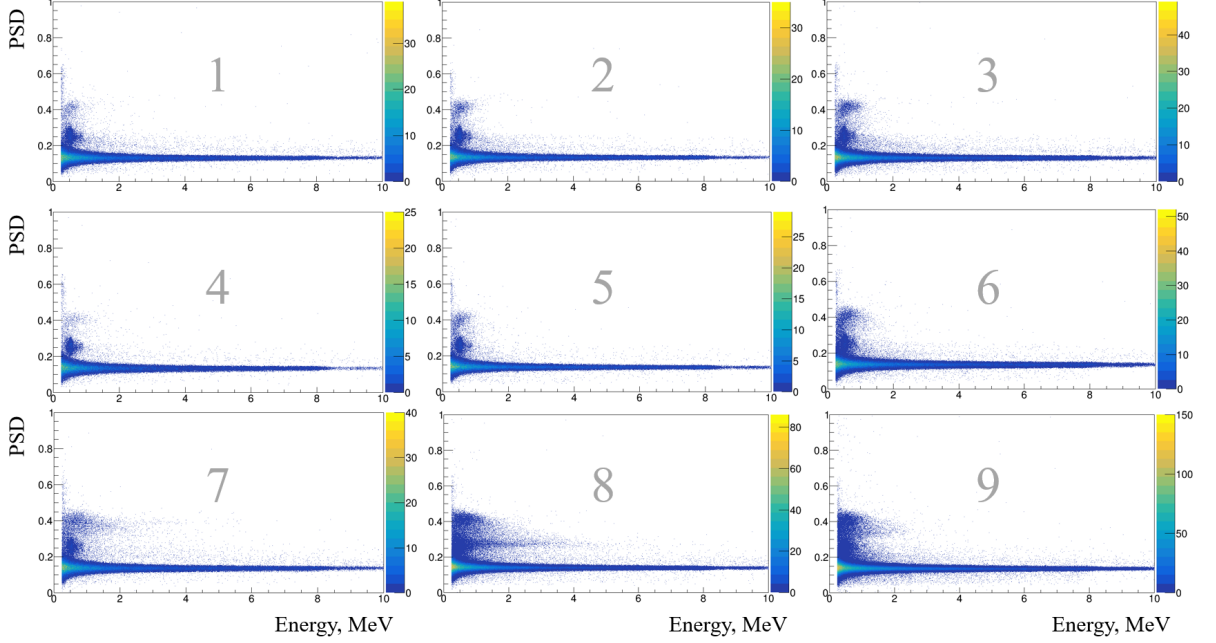
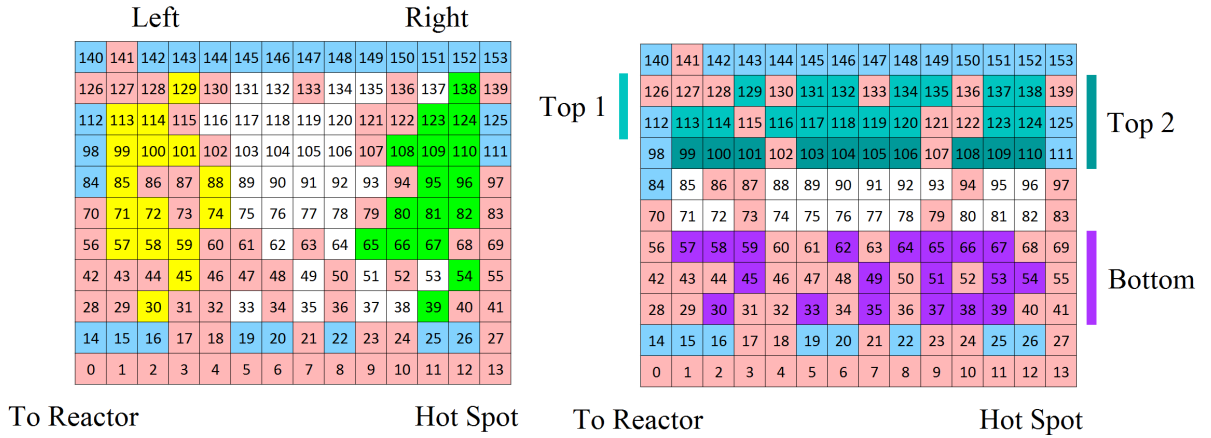


**Figure A.2:** PSD vs energy distributions for the events into each of 9 parts for one reactor-on run on May 15th, 2018. The plots show the behavior of ingress events that increase at the bottom of the detector, and to the right side above "hot spot".

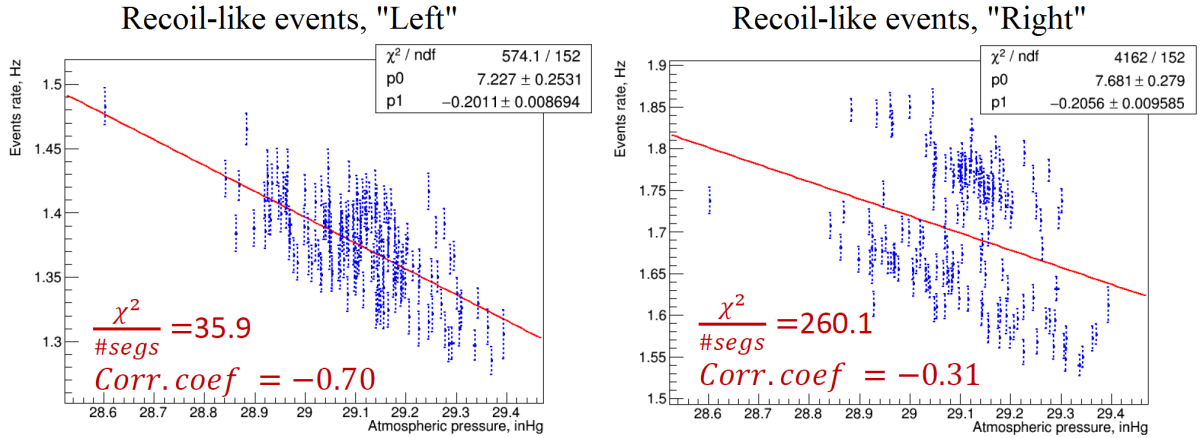
right side shows double behavior due to reactor-on/reactor-off shift. Comparing the numbers, we can see that correlation coefficient is higher for the left part, and the  $\chi^2/\text{DOF}$  is also smaller for it, which quantitatively shows better dependence on atmospheric pressure, and indicates that better portion of events is coming from true cosmogenic background.

Fig. A.5 shows similar comparison between Top 1 and Bottom parts for the same z-fiducial cut and PSD cut. Again, both visually and in quantitatively, top part indicates better cosmogenic nature, than bottom part.

This study was performed for 2 PSD cuts ( $\text{PSD} > 3.0 \sigma$  above the center of  $\gamma$ -band, and  $\text{PSD} > 3.5 \sigma$  above the center of  $\gamma$ -band) and for 2 z-fiducial cuts ( $z = \pm 444 \text{ mm}$  and  $z = \pm 434 \text{ mm}$ ), and the correlation coefficients and  $\chi^2$  are presented in Table A.1. The numbers show not only the spatial distribution corresponding to the ingress nature, but also that the shallower z-cut would give us better selection of events (ingress decreases closer to the center of the segment), and that the higher PSD cut would also provide better selection of cosmic events, comparing to ingress



**Figure A.3:** Separation of detector segments into left, right, top and bottom parts. Excluded segments are shown in red, and non-fiducial segments are shown in blue.



**Figure A.4:** Separation of detector segments into left, right, top and bottom parts. Excluded segments are shown in red, and non-fiducial segments are shown in blue.

contamination.

From this table, we can see that the best correlation coefficient rate = -0.74 for Top 2 selection for  $z = \pm 434$  mm, and  $\text{PSD} > 3.5 \sigma$ , and it also has one of the lowest  $\chi^2/\text{DOF}$ .

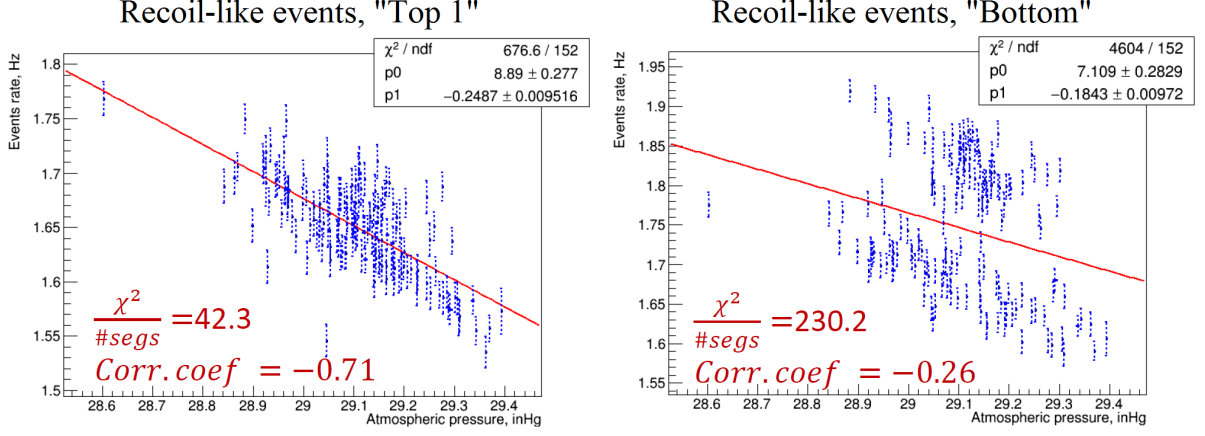


**Figure A.5:** Separation of detector segments into left, right, top and bottom parts. Excluded segments are shown in red, and non-fiducial segments are shown in blue.

**Table A.1:** Correlation coefficients with atmospheric pressure, and  $\chi^2/\text{DOF}$  for recoil-like events for different selection of spatial distribution, z-fiducial, and PSD cuts

Correlation coefficient / $\chi^2$	Whole	Top 1	Top 2	Bottom	Left	Right
$z = \pm 444 \text{ mm}$ PSD = $3.0 \sigma$	-0.39 / 114	-0.59 / 63	-0.55 / 68	-0.17 / 347	-0.57 / 58	-0.21 / 391
$z = \pm 434 \text{ mm}$ PSD = $3.0 \sigma$	-0.44 / 92	-0.62 / 54	-0.59 / 56	-0.20 / 287	-0.59 / 51	0.24 / 314
$z = \pm 444 \text{ mm}$ PSD = $3.5 \sigma$	-0.54 / 71	-0.71 / 42	-0.70 / 40	-0.26 / 230	-0.70 / 36	-0.31 / 260
$z = \pm 434 \text{ mm}$ PSD = $3.5 \sigma$	-0.58 / 57	-0.73 / 37	-0.74 / 33	-0.30 / 190	-0.72 / 32	-0.36 / 206

## Appendix B: Analysis of Temperature Dependence of Muon-like Events

### B.1 Temperature Measurements

The part of the data that was used from the archive was the data for pressure level types (major level type indicator (LVLTYYP1) and minor level type indicator (LVLTYYP2): standard pressure level/other pressure level, surface/tropopause/other), and all non-pressure levels were skipped (LVLTYYP1 LVLTYYP2: 30) since they did not provide pressure values.

The comparison of how temperature changes with altitude for dry season (March 4th, 2018) and humid season (August 28th, 2018) is shown in Fig B.1. The comparison of how humidity changes with altitude for the same dates is shown in Fig. B.2

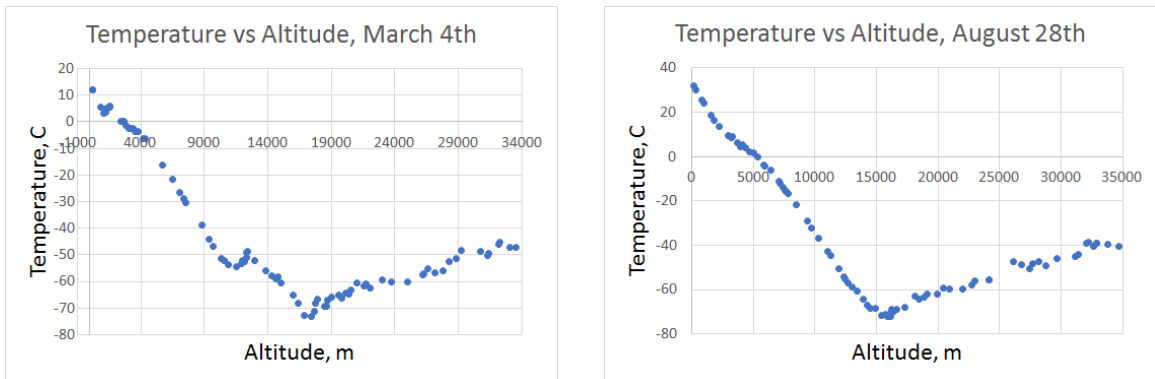


**Figure B.1:** Dependence of temperature on altitude for dry and humid seasons.

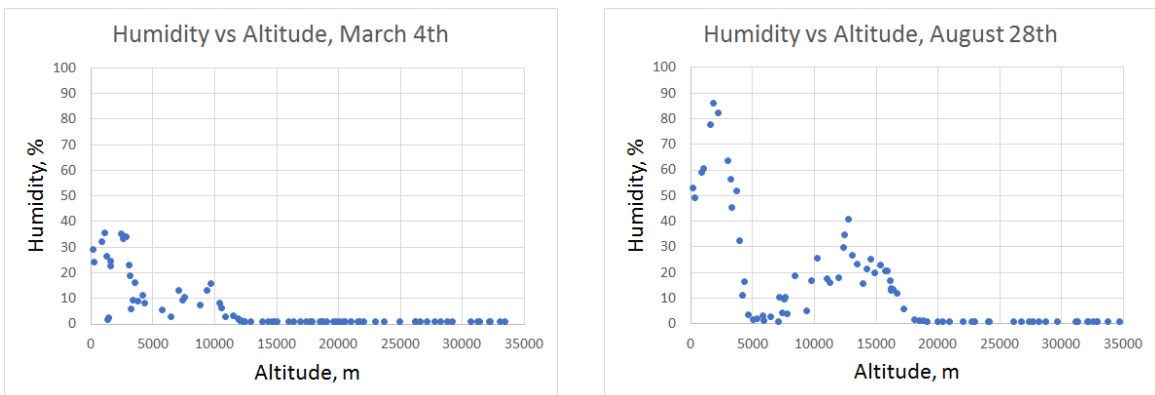


**Figure B.2:** Dependence of humidity on altitude for dry and humid seasons.

## B.2 Atmospheric Depth Calculation

Atmospheric depth at an altitude  $h$  characterizes the air mass the cosmic rays traverse to reach this altitude and measures their absorption along a vertical path to this altitude. It is defined as an integral of the air density of overlying layers of atmosphere:<sup>21;91;92</sup>

$$x[ht] = \int_h^\infty \rho[ht] dh, \quad \rho[ht] = \frac{P[ht]}{T[ht]} \cdot \frac{M_{Mol}}{R}$$

Here,  $\rho[ht]$  is the air density at the altitude  $h$ , and  $P[ht]$  and  $T[ht]$  are pressure and temperature at altitude  $h$ .  $M_{Mol} = 28.966$  g/mol is the molar mass of air, and  $R = 8.31446$  J/(K mol) is the universal gas constant. Atmospheric depth exponentially decreases with the altitude.

For the calculations of effective temperature, I used the approximation, also used in Daya Bay muon seasonal variation analysis<sup>86</sup>. Since by definition, pressure is a force per unit area:  $P = \frac{F}{A}$ . Considering gravity acceleration  $g = 9.81m/s^2$  as a constant, we can write weight of the air mass above:

$$F = \int g \cdot dm = \int_h^\infty g \rho A dh \approx g A \int_h^\infty \rho dh = P \cdot A$$

$$x[ht] = \int_h^\infty \rho \cdot dh \approx \frac{P[ht]}{g}$$

Which means that at the altitude  $h$ , the atmospheric depth can be approximated as a pressure level at that altitude, divided by gravitational acceleration. The comparison of the "correct" calculation with the "simplified" calculation of atmospheric depth vs altitude for one flight of balloon (March 4th) is shown in Fig. B.3

## B.3 Cutoff Altitude

The balloon flight maximum altitude is different for every data point. The distribution of data points is shown on Fig. B.4 with the minimal altitude of 5,622 m, and the maximum of 36,502 m. Fig. B.3 shows that even at 20,000 m, the atmospheric depth is not negligible to consider it 0. Therefore, we need to create cutoff of minimum flight altitude to get results consistent with as many

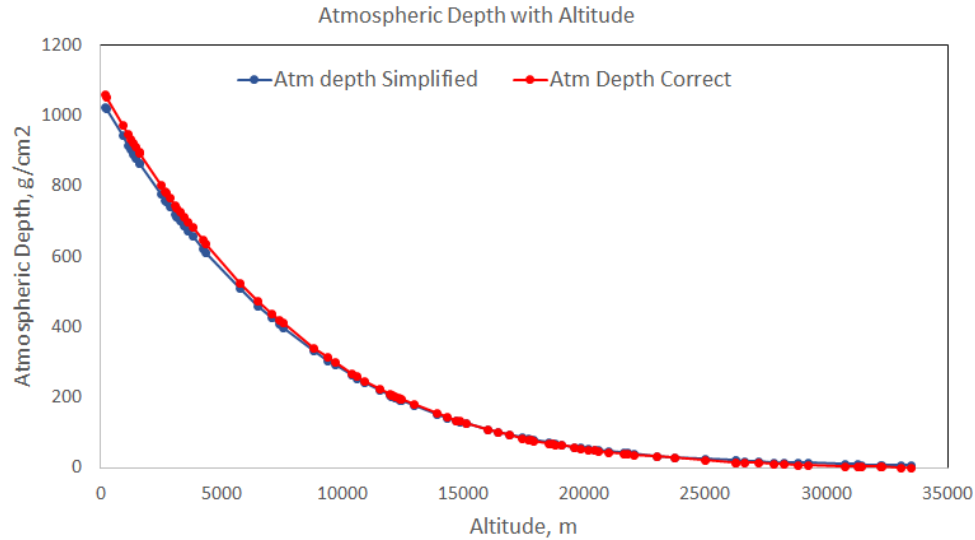


**Figure B.3:** Dependence of atmospheric dependence with altitude.

datapoints as possible.

To make the decision on cutoff value, a small study was done for March 4th datapoint. I put different cuts on the data for that flight, and calculated  $T_{EFF-M}$  for different cutoffs. From Fig. B.5 we can see, that below 25,000 m altitude, effective temperature dramatically depends on the altitude cutoff, and therefore cutoff must be done at least at 25,000 m where  $T_{EFF-M}$  gets approximately independent on higher altitude datapoints. Therefore, we cutoff all datapoints that don't reach at least 24,000 m, and consider value of atmospheric depth at 25,000 m altitude being fixed zero for all datapoints. With this cutoff, 1.8% of datapoints was lost (was 434 points, left 426 points).

## B.4 Uncertainty

To calculate uncertainty of modified effective and mass weighted temperature datasets, I chose to compare the values of  $T_{EFF-M}$  and  $T_{MSS}$  with the values of those parameters at the closest locations to Nashville, where other weather balloons are regularly launched. The reason behind this was that the main contribution to the uncertainty could be the distance between the PROSPECT detector (Oak Ridge) and Nashville - where the closest weather balloon is launched. By comparing the difference between two other locations, and calculating the root-mean-square value, a conclusion

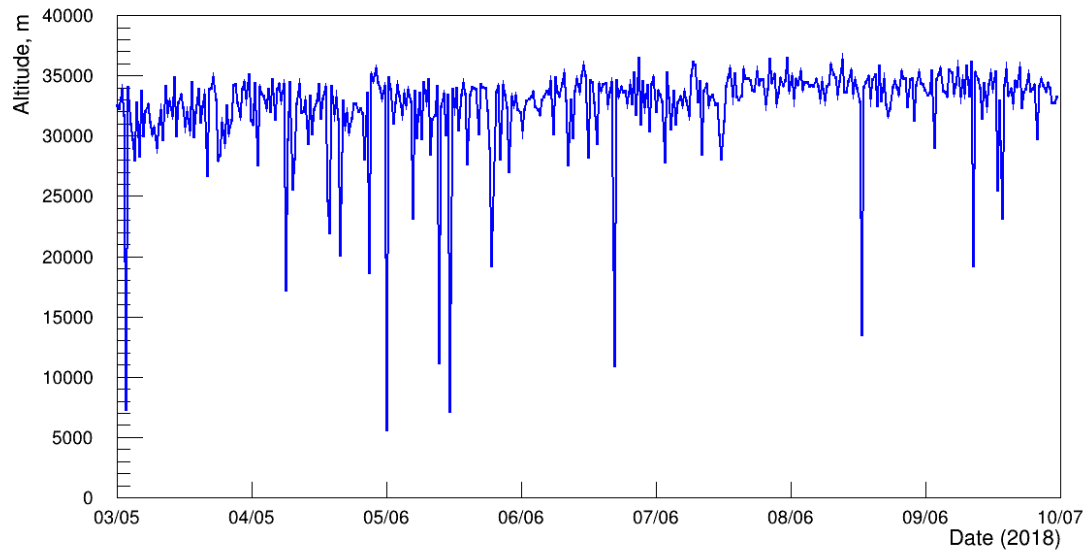


**Figure B.4:** Maximum altitude of balloon flight.

on systematic uncertainty can be derived. The closest locations to Oak Ridge after Nashville are in Peachtree City and in Blacksburg. Fig. B.6 shows the comparison between data values between all three locations for  $T_{EFF-M}$ , and Fig. B.8 - for  $T_{MSS}$ . We can see, that because Blacksburg is further from Nashville, the temperatures are consistently lower for  $T_{MSS}$ . Figures B.7 and Figure B.9 show the difference between those datasets between Peachtree City and Nashville.

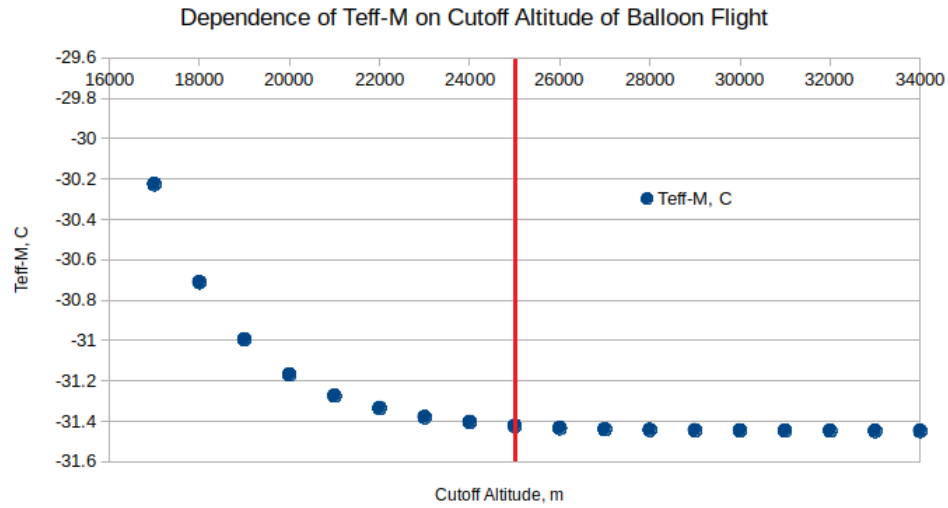


**Figure B.5:** Dependence of height cutoff on  $T_{EFF-M}$  value.

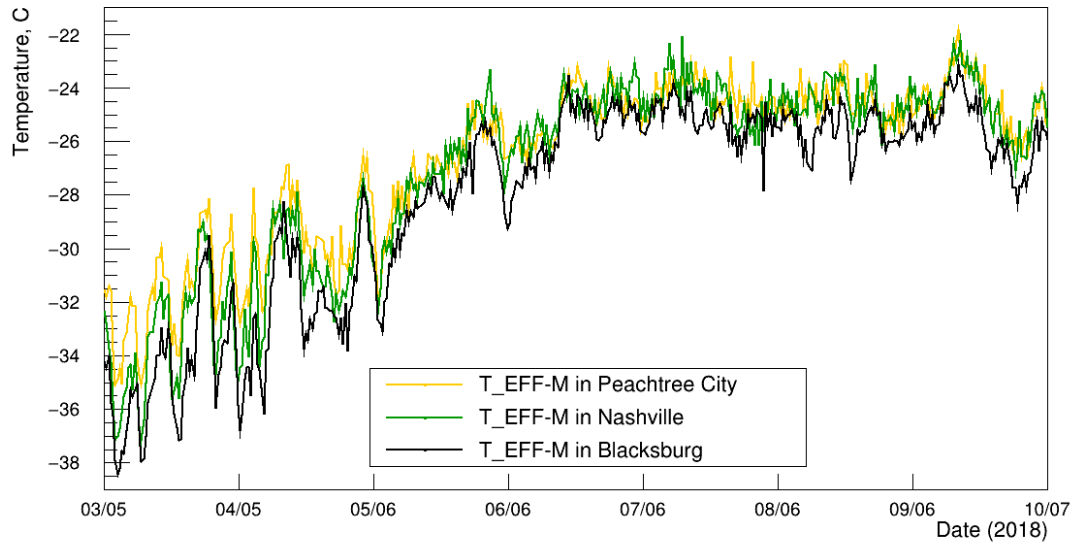


**Figure B.6:** Comparison of effective temperature calculations in Peachtree City, Nashville, and Blacksburg

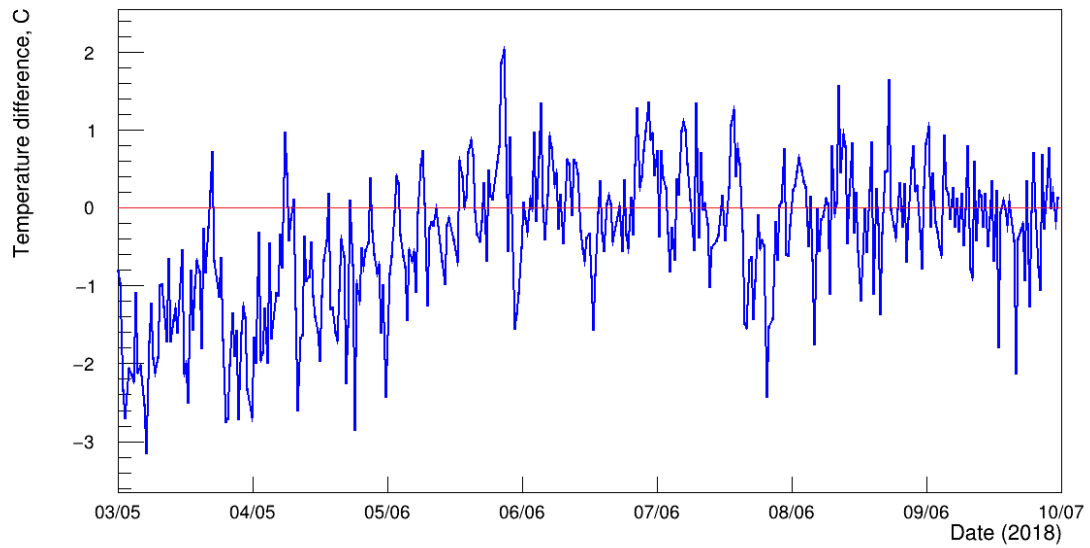


**Figure B.7:** Difference between EFF-M temperatures in Peachtree City and Nashville

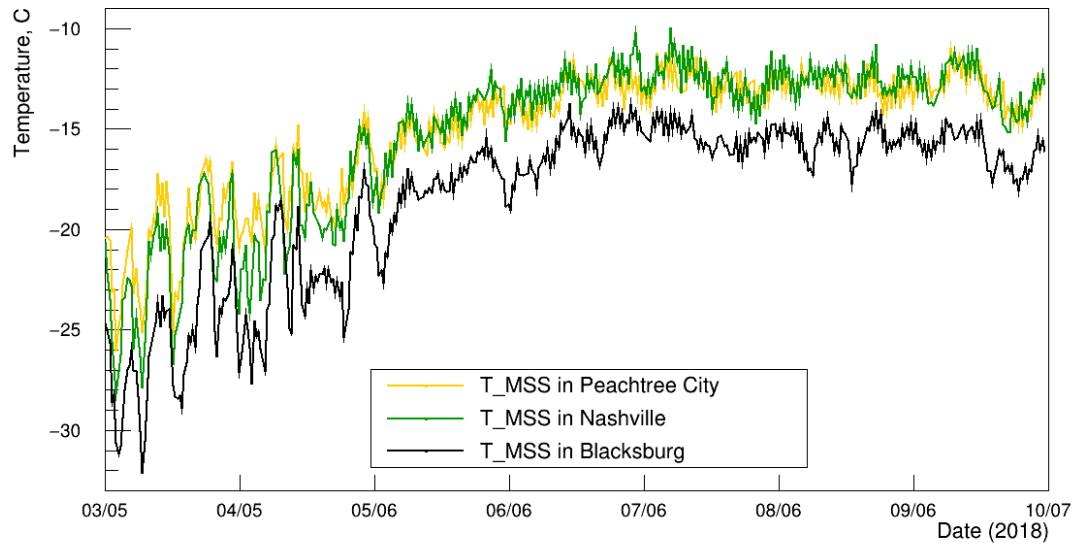


**Figure B.8:** Comparison of MSS temperature calculations in Peachtree City, Nashville, and Blacksburg

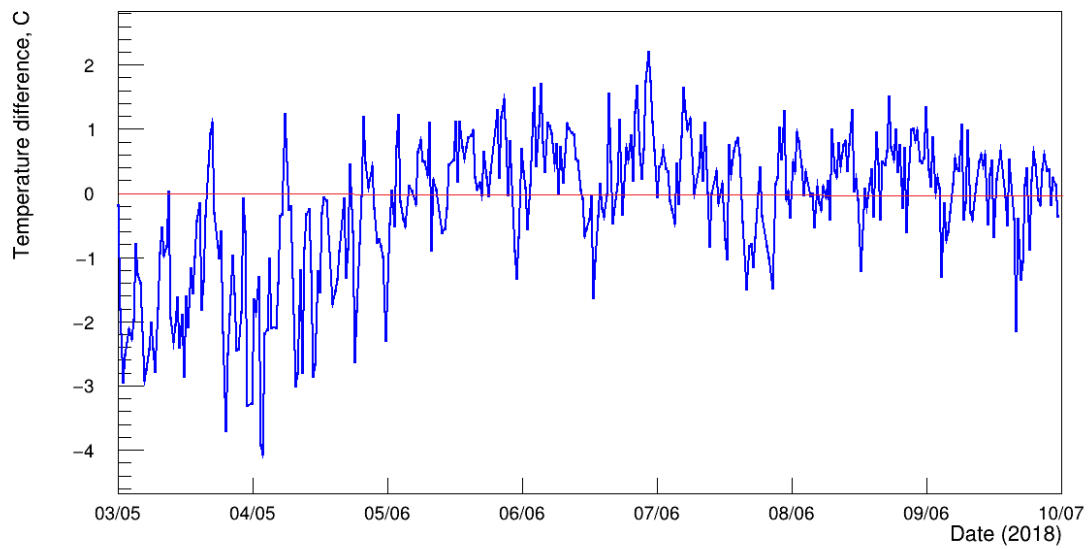


**Figure B.9:** Difference between MSS temperatures in Peachtree City and Nashville

